Instabilities in Soft Particulate Composites

By

Dean Chen

A dissertation submitted in partial fulfillment of

the requirements for the degree of

Doctor of Philosophy

(Mechanical Engineering)

at the

UNIVERSITY OF WISCONSIN – MADISON

2023

Date of final oral examination: 08/08/2023

The dissertation is approved by the following members of the Final Oral Committee:

Stephan Rudykh, Assistant Professor, Mechanical Engineering

Xiaoping Qian, Professor, Mechanical Engineering

Shiva Rudraraju, Assistant Professor, Mechanical Engineering

Izabela Szlufarska, Professor, Materials Science and Engineering

Melih Eriten, Associate Professor, Mechanical Engineering

Acknowledgments

In writing this PhD thesis, my heart overflows with immense gratitude toward those whose unwavering love and support have been the cornerstone of my journey.

To my beloved parents, Qingsong Chen and Jun Zhang, and my cherished brother, Dekang Chen. Their unwavering support during my pursuit of studying abroad has been nothing short of miraculous. Leaving behind the comforts of home and venturing into the unknown was a daunting decision, but it was their love, encouragement, and faith in my abilities that gave me the strength to take this bold step.

I am deeply indebted to my advisor, Stephan Rudykh, for his exceptional mentorship and guidance throughout my PhD study. His professional expertise, kindness, and encouragement were instrumental in shaping my research and personal growth. I am truly fortunate to have had such a dedicated and inspiring mentor, who always believed in my potential and helped transform my initial ideas into reality.

To my colleague friends, Yuhai, Qi, Nitesh, Neda, and Parag, I extend my sincere thanks for their camaraderie, motivation, and support during this academic endeavor. I am especially grateful to Dr. Jian Li, whose collaboration and guidance have been instrumental in my research journey. I want to extend this gratitude to the entire Faculty and staff of the Mechanical Engineering Department at UW-Madison.

Lastly, I am deeply appreciative of the financial support provided by the Chinese Scholarship Council, which made my PhD study possible. Their generosity and belief in my potential have allowed me to focus on my research and academic pursuits.

Abstract

This Ph.D. dissertation presents a multifaceted study of the instability-induced pattern transformations in soft particulate composites undergoing large deformations, via various numerical approaches and considering different forms and dimensions of the composite configurations. This study also emphasizes the whole process study of the instability phenomenon in composite materials, from prior- to post-buckling regimes.

Specifically, results are presented for different forms of particulate composites, including 1) 2D rectangular cells with a single-sized inclusion, 2) 2D rectangular cells with two different-sized inclusions, and 3) 3D cuboid cells with a single-sized sphere inclusion. Numerical results derived from various methods are shown and discussed, including those from i) Bloch-Floquet analysis, ii) Post-Buckling analysis, iii) Energy quasi-convexification analysis, and iv) a hybrid method that implements Bloch-Floquet analysis in the post-buckling regime.

In addition to presenting the dependence of instability critical characteristics on the composite's initial geometric configurations, the study also highlights key findings and novel insights, including i) the transition of buckling behavior as the composite's manifestation of two soft particulate systems; ii) the divergence of linearized instability predictions in their post-buckling regimes; iii) the unique "seemingly non-periodic" state of buckling modes; iv) the occurrence of secondary instability in the post-buckling regime of the particulate composite; v) the interplay of two different-sized inclusions in particulate composites; and vi) the differences in instability behaviors between 2D and 3D particulate composites.

Additionally, a post-processing method based on the discrete Fourier transformation (DFT)

is developed for characterizing post-buckling development. This method enables accurate identification of critical characteristics compared to traditional visual inspection of repeating blocks. It also facilitates the future application of experimental identification of instability-induced pattern transformations by circumventing test defects.

Table of Contents

Acknowledgments i
Abstract ii
Table of Contents iv
List of Figures v
1. Introduction 1
1.1 Soft composites 1
1.2 Elastic instabilities 2
1.3 Instabilities in soft particulate composites 4
1.4 Numerical analysis of instabilities in periodic composites. 5
1.5 Outline of this dissertation 7
2. Theoretical background 9
2.1 Nonlinear elasticity 9
2.2 Analysis of macroscopic instability 9
2.3 Analysis of microscopic instability 11
2.4 Constitutive models 13
3. Numerical modeling 14
3.1 Bloch-Floquet analysis 14
3.1.1 2D Analysis (single-sized inclusion) 14
3.1.2 2D Analysis (two different-sized inclusions) 17
3.1.3 Bloch-Floquet analysis in post-buckling regime 18
3.1.4 3D Analysis 20
3.2 Energy quasi-convexification analysis 21
3.3 Post-buckling analysis 24
3.3.1 Geometric modeling 24
3.3.2 Characterization of post-buckling development 29
4. Numerical results 30
4.1 Composite(2D) with single-sized inclusions 30
4.1.1 Bloch-Floquet prediction 30
4.1.2 Energy landscapes 44
4.1.3 Post-buckling analysis 47
4.1.4 Secondary buckling development in post-buckling regime 65
4.2 Composite(2D) with two different-sized inclusions 74
4.2.1 Bloch-Floquet prediction 74
4.3 Composite(3D) with single-sized inclusions 82
4.3.1 Bloch-Floquet prediction 82
5. Conclusion 86
Appendix A The influence of the number of unit cells in the RVE for post-buckling analysis 89
Bibliography 90

List of Figures

Fig. 1 Schematic composite microstructure with stiff circular inclusions periodically distributed in soft matrices. 12
Fig. 2 Schematic composite microstructure with stiff circular inclusions periodically distributed in soft matrices. 15
Fig. 3 Dispersion curves of the composite subjected to increasing levels of compressive strains. 16
Fig. 4 a) Schematic composite microstructure with two different-sized stiff circular inclusions periodically distributed in soft matrices; Schematic composite with inclusion diameter contrast ratio b) $k_d = 1$, c) $k_d = 0.2$, d) $k_d \approx 0$. 18
Fig. 5 Schematic representative volume element with two composite unit cells in a) the initial undeformed state and b) its post-buckling regime corresponding to its initial periodicity being exactly doubled. 19
Fig. 6 Schematic 3d composite microstructure with stiff sphere inclusions periodically distributed in cuboid soft matrices. 21
Fig. 7 a) Landscape of the normalized stored-energy W as a function of the compressive strain ε and shear strain γ (corresponding to $\xi = 0.7$ and $\eta = 1$) b) Schematic composite cell subjected to simultaneously applied compressive strain and pure shear deformations 24
Fig. 8 Schematic composite microstructure with stiff circular inclusions periodically distributed in soft matrices. 25
Fig. 9 (a) Schematic composite cell without geometric imperfection. 27
Fig. 10 The DFT results of the post-buckling development at compressive strain $\varepsilon = 0.241$ for numerical models with (a) various amplitudes of geometric imperfection ($Kimp = 10^{-2}, 10^{-3}, 10^{-4}, 10^{-5}$, 10^{-6}, and 10^{-7}); (b) different realizations of random imperfection with the same amplitude of geometric imperfection $K_{imp} = 10^{-5}$. 28
Fig. 11 The dependence of critical strain on periodicity aspect ratio with various spacing ratios. Dotted and continuous curves correspond to macroscopic and microscopic instabilities, respectively. 31
Fig. 12 Distribution of strain field, ε_{22}, in the composite with $\xi = 0.6$ under the applied average compressive strain $\varepsilon = 0.24$ with various periodicity aspect ratios. 34
Fig. 13 The dependence of critical wavenumber on the periodicity aspect ratio with various spacing ratios. Dotted and continuous curves correspond to macroscopic and microscopic instabilities, respectively. 35
Fig. 14 Schematics of instability patterns based on initial primitive cells and enlarged primitive cells. 36
Fig. 15 Eigenmodes of the composites at the critical strains with spacing ratio $\xi = 0.4$ and various periodicity aspect ratios from 1.546 to 1.325. 39
Fig. 16 Surface of critical wavenumber in the space of periodicity and spacing ratio. 41
Fig. 17 Critical dispersion curves corresponding to the jump-transition mode. 43
Fig. 18 Critical dispersion curves corresponding to the limited-transition mode 44
Fig. 19 Critical dispersion curves corresponding to the full-transition mode. 44
Fig. 20 (a) Comparison of critical strains derived from quasi-convexification and Bloch-Floquet analyses for the composites with $\xi = 0.3$, $\xi = 0.5$, $\xi = 0.7$ and $\xi < \eta \leq 5$; 47
Fig. 21 (a) The deformation sequence under compressive strain level $\varepsilon = 0$, 0.233, and 0.253; initial geometric parameters are $\xi = 0.6$ and $\eta = 2.1$; (b) The position of inclusion centers in the deformed RVE. 48
Fig. 22 The DFT analysis results of the post-buckling development for the composite with spacing ratio $\xi =$

0.6 and periodicity aspect ratio $\eta = 2.1$ at compressive strain $\varepsilon = 0.233$, $\varepsilon = 0.2339$, $\varepsilon = 0.234$, $\varepsilon = 0.235$, $\varepsilon = 0.237$, and $\varepsilon = 0.24$ with $N = 80$ number of unit cells built in the RVE. 51

Fig. 23 Post-buckling patterns and the corresponding DFT results with fixed spacing ratio $\xi = 0.8$ and various periodicity aspect ratios (compared with the critical wavenumber predicted from the Bloch-Floquet analysis). 53

Fig. 24 Post-buckling patterns and the corresponding DFT results with fixed spacing ratio $\xi = 0.3$ and various periodicity aspect ratios (in comparison with the critical wavenumber predicted from Bloch-Floquet analysis). 56

Fig. 25 Post-buckling patterns and the corresponding DFT results with fixed spacing ratio $\xi = 0.45$ and various periodicity aspect ratios (compared with the critical wavenumber predicted from Bloch-Floquet analysis). 58

Fig. 26 Post-buckling pattern mapping in the geometrical parameter space. 61

Fig. 27 Post-buckling patterns and the corresponding DFT results for the case with spacing ratio $\xi = 0.45$ and periodicity aspect ratio $\eta = 1.5$ under various compressive strain levels (1) $\varepsilon^{cr} = 0.338$, (2)$\varepsilon^{cr} = 0.3386$, (3)$\varepsilon^{cr} = 0.34$ and (4)$\varepsilon^{cr} = 0.348$. 63

Fig. 28 The deformation sequence under compressive strain level $\varepsilon = 0$, $\varepsilon = 0.343$, $\varepsilon = 0.368$, $\varepsilon = 0.555$, and $\varepsilon = 0.565$; initial geometric parameters are $\xi = 0.45$ and $\eta = 6$. Only 80 unit cells of the RVE are displayed for a more compact illustration. 66

Fig. 29 The DFT analysis results of the post-buckling development for the composite with spacing ratio $\xi = 0.45$ and periodicity aspect ratio $\eta = 6$ at compressive strain $\varepsilon = 0$, $\varepsilon = 0.34$, $\varepsilon = 0.368$, and $\varepsilon = 0.557$ with $N = 320$ number of unit cells built in the RVE (the RVE view is zoomed so not all inclusion are displayed). 67

Fig. 30 The dependence of *secondary* buckling critical strain on periodicity aspect ratio with various spacing ratios. The dotted and continuous curves correspond to longwave and microscopic buckling results (from the post-buckling analysis), respectively; the triangular scatters correspond to results from the Bloch-Floquet analysis. 69

Fig. 31 The dependence of critical wavenumber on the periodicity aspect ratio with various spacing ratios. Triangular scatters and continuous curves correspond to results from post-buckling analysis and Bloch Floquet analysis, respectively. 72

Fig. 32 The first and secondary buckling pattern mapping in the geometrical parameter space. The highlighted areas (bright and dark blue) represent the secondary buckling. 73

Fig. 33 The dependence of critical strains on inclusion diameter contrast ratio with various spacing ratios in composite with two different-sized inclusions. 74

Fig. 34 The dependence of critical wavenumber on inclusion diameter contrast ratio with spacing ratio $\xi = 0.4$ in composite with two different-sized inclusions. 79

Fig. 35 The dependence of critical wavenumber on inclusion diameter contrast ratio with spacing ratio $\xi = 0.6$ in composite with two different-sized inclusions. 80

Fig. 36 The dependence of critical wavenumber on inclusion diameter contrast ratio with spacing ratio $\xi = 0.8$ in composite with two different-sized inclusions. 82

Fig. 37 The dependence of critical strain on periodicity aspect ratio with various spacing ratios for 3D particulate composites. Dotted and continuous curves correspond to macroscopic and microscopic instabilities, respectively. 83

Fig. 38 Schematic microstructure of the 3D particulate composite and the 3D extrusion of the 2D particulate composite. 84

Fig. 39 The dependence of critical wavenumber on periodicity aspect ratio with various spacing ratios for 3D particulate composites. Dotted and continuous curves correspond to macroscopic and microscopic instabilities, respectively. 85

Fig. 40 The DFT results of the post-buckling development for composite with spacing ratio $\xi = 0.6$ and periodicity aspect ratio $\eta = 2.1$ at compressive strain $\varepsilon = 0.237$, for various numbers of unit cells built in the RVE ($N = 20, N = 40, N = 80, N = 120, N = 160,$ and $N = 200$)..... 90

1. Introduction

1.1 Soft composites

Soft materials such as elastomers, gels, and biological tissues possess the capability to develop large deformations in response to diverse external stimuli, including mechanical loading (Shan et al., 2015), electrical (Acome et al., 2018; Kellaris et al., 2018; Su et al., 2020) and magnetic fields (Yu et al., 2018; Kim et al., 2018; Tipton et al., 2012), heat (Yuan et al., 2017, 2018) and light (Zhao et al., 2017; Wang et al., 2018), thus providing rich opportunities for designing active materials with various distinctive and unconventional properties (Babaee, et al., 2016; Liu et al., 2016; Tang et al., 2015). The soft composite materials, constructed by reinforced matter embedded in the soft matrix, can achieve a wider range of special electronic, optical, and acoustic properties due to their precisely designed shape, geometry, orientation, and arrangement of microstructures (Bertoldi et al., 2008; Gao et al., 2018; Li & Rudykh, 2019b; Li et al., 2018b). These properties can be further empowered via the instability-induced pattern transformation of their microstructures. Such transformations can enable the design of materials with tunable and switchable properties such as tunable bandgaps (Li et al., 2019c; Rudykh & Boyce, 2014; Shan et al., 2014; Wang et al., 2014; Gao et al., 2019; Pranno et al., 2022), negative group velocity states (Slesarenko et al., 2018; Arora et al. 2022a) and negative Poisson's ratio and auxetic behavior (Bertoldi et al., 2008, 2010; Mullin et al., 2007; Li et al., 2018b; Li & Rudykh, 2019b; Li et al., 2019c). Moreover, knowledge about the mechanical instability phenomenon can help elucidate the morphogenesis of organs during growth in various biological systems (Budday et al., 2014; Garcia et al., 2018; Du et al., 2020).

1.2 Elastic instabilities

The elastic instabilities are often accompanied by a dramatic change in materials' structure configurations and a sudden loss in their load capacities. Traditionally, the buckling phenomenon has been regarded as a failure mode in engineering. However, as discussed above, the recent new concept of using the rich instability-induced pattern transformations in soft materials has been put forward. In hyperelastic soft composites, instability can develop at microscopic and macroscopic(longwave) length scales (Geymonat et al., 1993). The macroscopic (or longwave) instability refers to the buckling wavelength being significantly larger than the characteristic size of the microstructure. In contrast, the buckling wavelength in microscopic instability is comparable with the characteristic size of the microstructure. To analyze the elastic instabilities, the framework of the linearized small motions superimposed on finitely deformed solids is frequently used (Ogden, 1997). The onset of macroscopic or longwave instabilities can be identified through the loss of ellipticity analysis. In composite materials, the loss of ellipticity analysis requires evaluations of the tensor of elastic moduli, which can be calculated through numerical (Bruno et al., 2010; Greco & Luciano, 2011; Greco et al., 2018, 2021; Pranno et al., 2022; De Maio et al., 2023; Aboudi & Gilat, 2023; Melnikov et al., 2021) or analytical (Rudykh & Debotton, 2012) homogenization approaches. Alternatively, the loss of the ellipticity condition can be determined directly through phenomenological models (Merodio & Ogden, 2002, 2003, 2005a, 2005b; Merodio & Pence, 2001a, 2001b; Aboudi & Volokh, 2020; Ehret & Itskov, 2007; Volokh, 2017; Qiu & Pence, 1997). However, the onset of the microscopic instabilities, which develops at finite wavelengths, may precede the occurrence of longwave instabilities (Geymonat et al., 1993).

To predict the onset of microscopic instabilities and to determine the critical level of deformation and wavelength, the Bloch-Floquet analysis is typically employed (Geymonat et al., 1993; Triantafyllidis et al. 2006; Bertoldi et al., 2008; Slesarenko & Rudykh, 2017). Note that the longwave limit in the Bloch-Floquet analysis is equivalent to the loss of ellipticity condition (Geymonat et al., 1993).

These methods have been effectively applied in the theoretical prediction of instabilities in various soft systems and have also been realized via experimental investigations. For fiber composites (FCs), Galich et al. (2018) examined the influence of the periodic fiber distribution on instabilities and shear wave propagation in 3D fiber composites. Rudykh & Debotton (2012) employed micromechanics-based homogenization to predict the macroscopic instabilities in transversely isotropic fiber composites. Li et al. (2018a) experimentally observed the transition of elastic instabilities in 3D-printed fiber composites from small wavelength wavy patterns to longwave modes. Through both simulations and experiments, Arora et al. (2022b) examined the influence of constituent material properties on buckling orientation in fiber composites. For instabilities in soft laminates, Li et al. (2013) observed in experiments the microscopic and macroscopic instabilities in 3D-printed layered materials. Arora et al. (2019) considered the inhomogeneous interphases in 3D-printed soft laminates and examined their influence on composite stability. Slesarenko and Rudykh (2016) utilized the visco-hyperelastic behavior (Xiang et al., 2020a, 2020b) to achieve tunable wavy patterns through variable strain rates. Li et al. (2019d) analyzed the elastic instability in compressible laminates, where the stabilizing effect of phase compressibility was reported. Li et al. (2022) experimentally observed the formation of twinning microstructures in soft laminates driven by instabilities.

Wrinkling instabilities are also found to develop in the system of a thin stiff film on a compliant flat soft substrate under compression beyond a critical level (Cao et al., 2012; Chen et al., 2004; Huang et al., 2005; Jiang et al., 2007; Song et al., 2008; Cheng et al., 2014; Chen et al., 2014). This wrinkling may transit to more complex secondary patterns with further deformation (Sun et al., 2012; Pocivavsek et al., 2008; Brau al., 2011, 2013; Jin et al., 2015; Li et al., 2011; Auguste et al., 2018; Efimenko et al., 2005; Chung et al., 2011; Vella et al., 2009; Ebata et al., 2012; Mei et al., 2011). The "stiff film"-"soft substrate" system may produce rather different patterns when subjected to biaxial compressive deformations (Chen et al., 2004; Cai et al. 2011; Huang et al., 2005; Yin et al., 2012, 2018; Yin & Boyce, 2015; Choi et al., 2007; Bae et al., 2015; Kim et al., 2011; Lin et al., 2007). Moreover, structural instabilities have also been found in soft electro- (Rudykh et al., 2012), magneto- (Saxena et al., 2019; Reddy et al., 2017, 2018), or electro-magneto-elastic membranes (Saxena et al., 2021; Liu et al., 2021).

In addition to the instabilities in the soft layers under compressive deformation, various instability modes have also been observed under tensile deformation. For example, cavitation and fringe instabilities are observed in soft layers with perfect adhesion to a stiff substrate under a tensile deformation (Shull et al., 2000; Lin et al., 2016).

1.3 Instabilities in soft particulate composites

In contrast to continuous-phase composites like soft FCs and laminates, discrete-phase composites, such as particulate composites, present greater challenges in the analysis of their instabilities. This is primarily due to the highly inhomogeneous distribution of the deformation field and the complex interactions between particles. Constraining the equivalent 3D FC into

the in-plane setting, the stability of the 2D particulate system of fiber cross-section has been examined (Triantafyllidis et al., 2006). The re-examination of this problem under similar combined in-plane loadings was conducted by Michel et al. (2010), which compared the macroscopic stability of the composite with a random distribution of circular or elliptical inclusions. Li et al. (2019a) experimentally observed the formation of wavy chain patterns in soft particulate composites. Goshkoderia et al. (2020) reported that the pattern formation in soft particulate composites could be controlled via magnetic fields. Xiang et al., 2023 investigated the interplay between viscoelasticity and instabilities in soft particulate composites undergoing finite deformation. However, there remains a significant shortage of comprehensive studies investigating the instabilities developing in soft particulate composites. Moreover, there is a lack of research focused on validating and enhancing conventional instability analysis methods, such as Bloch-Floquet and Post-buckling analysis for discrete-phase particulate systems.

We note that the Bloch-Floquet analysis and the alternatives, such as the refined eigenvalue analysis (Bertoldi et al., 2008), are linearized methods. The post-buckling analysis considers the nonlinearity in the post-buckling development, thus, providing additional information (potentially more accurate) about the development of instability patterns under large deformations.

1.4 Numerical analysis of instabilities in periodic composites.

The analytical prediction of elastic instabilities in heterogeneous materials, such as particulate composites, poses significant challenges due to the high inhomogeneous

distribution of the deformation field and intricate interactions between the embedded particles. Therefore, numerical methods, such as the finite element method (FEM), have been widely used as powerful tools for investigating and simulating instability behaviors. Furthermore, via advanced computational platforms, a reliable numerical model of instabilities is capable of providing robust databases of materials behaviors for advanced machine learning research in metamaterial design.

Given the understanding of instability-induced pattern transformation as a break of the composite's initial periodicity and followed by it attaining a new periodicity, different numerical approaches have been developed to investigate the bifurcations occurring in infinite periodic solids. By imposing traditional eigenvalue instability analyses on representative volume element (RVE) of increasing size and with general periodic boundary conditions, the so-called "Refined Eigen Analysis" has been employed to determine the critical loading and wavelength by a discrete convergence search (Laroussi et al., 2002; Bertoldi et al., 2008). However, the so-called Refined Eigen Analysis only works as a compromised approach to extend the traditional eigen analysis to an infinite space, and is limited by low precision, no consideration of prior instability stress field, and will face a nearly infeasible number of integrations when identifying longwave instability. As mentioned in Sec. 1.2, the advanced numerical Bloch-Floquet analysis (also known as the Bloch wave analysis) (Triantafyllidis and Schnaidt, 1993; Triantafyllidis and Schraad, 1998; Triantafyllidis et al., 2006) can not only achieve the detection of both microscopic and longwave instabilities for infinitely periodic composites in multiple directions, but also provide opportunities for investigating the wave propagation in soft composites. However, we also note that both the Bloch-Floquet analysis

and its alternatives, as well as the Refined Eigenvalue Analysis, are linearized methods, which only predict the linearized development of instability right at the critical loading. The further evolution of the buckled structure with deformation beyond the critical loading cannot be captured, especially in the situation when the initial buckling mode changes with the applied deformation(Chen et al., 2022, 2023). The post-buckling analysis, which considers the nonlinearity in deformation development and monitors the finite deformation of buckling evolution from prior- to post-buckling regimes, provides additional information (potentially more accurate) about the instability patterns under large deformations(Chen et al., 2023). Specifically for incompressible neo-Hookean hyperelastic materials, the numerical quasi-convexification analysis can also be implemented to determine the critical loading of instability at prescribed wavelengths (Conti et al., 2008; Furer & Ponte Castañeda, 2018). Moreover, via the derived energy landscape, further information can be obtained for understanding the influence of geometrical and material parameters on critical instability characteristics.

1.5 Outline of this dissertation

In this Ph.D. dissertation research, we examine the instabilities in soft particulate composites and the associated pattern transformations via various numerical approaches and in different forms and dimensions. Specifically, the numerical approach includes the i) Bloch-Floquet analysis; ii) Post-Buckling analysis; iii) Energy quasi-convexification analysis, and iv) Hybrid method combining the Post-Buckling and Bloch-Floquet analysis. We consider different forms of particulate composites, including a) 2D rectangular unit cells with single-sized inclusion; and b) 2D rectangular unit cells with two different-sized inclusions.

Remarkedly, we emphasize the whole process study of the instability development in soft particulate composites, from prior- to post-buckling regimes, which helps to uncover a distinctive buckling phenomenon where a secondary instability occurs in the post-buckling regime of particulate composites. Finally, we also investigated the instabilities in 3D version of the single-sized inclusion composite (cuboid unit cell with sphere inclusions). The overall structure of this dissertation is described as follows:

In section 2, we provide the theoretical background of instability analysis and the used constitutive models. In section 3, we present the numerical modeling methods for Bloch-Floquet, Energy quasi-convexification, and post-buckling analysis conducted in this research. The corresponding geometric and material models, finite element models, and boundary conditions, as well as the post-processing methods, are also included. In section 4, we discussed the numerical results of 2D composites with single-sized inclusions and two different-sized inclusions and the results of 3D composites.

We would like to highlight the discussion of i) transition of buckling behavior as the composite's manifestation of two soft particulate systems [Sec. 4.1.1.1]; ii) the difference between post-buckling and Bloch-Floquet predictions [Sec. 4.1.3]; iii) the unique "seemingly non-periodic" state of buckling modes [Sec. 4.1.1.2]; iv) the secondary instability occurring in the post-buckling regime of particulate composites [Sec. 4.1.4]; v) the interplay of two different-sized inclusions in particulate composites on their instability behaviors [Sec. 4.2.1]; and vi) the difference between inabilities in corresponding 2D and 3D particulate composites [Sec. 4.3.1].

2. Theoretical background

2.1 Nonlinear elasticity

Consider a continuum body where the position vector of each point is denoted by $\boldsymbol{X}$ in the reference (or undeformed) and $\boldsymbol{x}$ in the current (or deformed) configurations. The mapping function between the position vectors is expressed by $\boldsymbol{x} = \boldsymbol{\chi}(\boldsymbol{X})$. The deformation gradient is defined as $\boldsymbol{F} = \partial \boldsymbol{x}/\partial \boldsymbol{X}$, and its determinant is defined as $J \equiv det\, \boldsymbol{F} > 0$. Consider a hyperelastic material and its constitutive behavior is defined by a strain energy density function, $W(\boldsymbol{F})$, thus, the first Piola-Kirchhoff stress tensor is expressed as

$$\boldsymbol{P} = \frac{\partial W(\boldsymbol{F})}{\partial \boldsymbol{F}}. \tag{1}$$

For an incompressible material, $J = 1$, and Eq. (1) modifies as

$$\boldsymbol{P} = \frac{\partial W(\boldsymbol{F})}{\partial \boldsymbol{F}} - p\boldsymbol{F}^{-T}, \tag{2}$$

where p is an unknown Lagrange multiplier.

The relationship between the Cauchy stress ($\boldsymbol{\sigma}$) and the first Piola-Kirchhoff stress tensors is defined as $\boldsymbol{\sigma} = J^{-1}\boldsymbol{P}\boldsymbol{F}^{T}$. In the undeformed configuration, the equation of motion for quasi-static deformation and without body forces is written as

$$Div\, \boldsymbol{P} = \boldsymbol{0}. \tag{3}$$

2.2 Analysis of macroscopic instability

To analyze the material stability, we consider incremental deformations superimposed on a finitely deformed state (Ogden, 1997). The corresponding linearized constitutive law is

$$\dot{\boldsymbol{P}} = \mathbb{A}\colon \dot{\boldsymbol{F}}. \tag{4}$$

where $\dot{\boldsymbol{F}}$ is an incremental change in the deformation gradient, $\dot{\boldsymbol{P}}$ is the corresponding change

in the first Piola-Kirchhoff stress tensor, and $\mathbb{A}$ is the tensor of elastic moduli, defined as

$$\mathbb{A} = \frac{\partial^2 W}{\partial \boldsymbol{F} \partial \boldsymbol{F}}. \tag{5}$$

Under the assumption that $\mathbb{A}_{ijkl}$ is independent of $\boldsymbol{X}$, the incremental equilibrium equation can be written in the form,

$$\mathbb{A}_{i\alpha j\beta} \frac{\partial^2 u_j}{\partial X_\alpha \partial X_\beta} = 0. \tag{6}$$

For incompressible materials, Eq. (6) takes the form,

$$\mathbb{A}_{ijkl} \frac{\partial^2 u_l}{\partial X_i \partial X_k} + \frac{\partial \dot{p}}{\partial x_j} = 0, \tag{7}$$

where $\boldsymbol{u}$ is incremental displacement associated with $\dot{\boldsymbol{F}}$, $\dot{p}$ is an incremental variation in p.

Recall that the incompressibility condition implies

$$\nabla \cdot \boldsymbol{u} = 0. \tag{8}$$

By application of the chain rule, the incremental equilibrium Eq. (7) can be written in the deformed configuration as

$$\mathbb{A}^0_{ipjq} \frac{\partial^2 u_j}{\partial x_p \partial x_q} + \frac{\partial \dot{p}}{\partial x_i} = 0, \tag{9}$$

where

$$\mathbb{A}^0_{ipjq} = J^{-1} F_{p\alpha} F_{q\beta} \mathbb{A}_{i\alpha j\beta}, \tag{10}$$

We seek a solution for Eq. (10) in the form

$$\boldsymbol{u} = \hat{\boldsymbol{m}} e^{ik\boldsymbol{x}\cdot\hat{\boldsymbol{n}}}, \ \dot{p} = \hat{p} e^{ik\boldsymbol{x}\cdot\hat{\boldsymbol{n}}}, \tag{11}$$

where k is a wavenumber, $\hat{\boldsymbol{m}}$ and $\hat{\boldsymbol{n}}$ are unit vectors.

The incompressibility condition Eq. (8) leads to the requirement

$$\hat{\boldsymbol{m}} \cdot \hat{\boldsymbol{n}} = 0. \tag{12}$$

Substitution of Eq. (11) into Eq. (9) yields

$$\boldsymbol{Q}\hat{\boldsymbol{m}} + i\hat{p}\hat{\boldsymbol{n}} = \boldsymbol{0}, \tag{13}$$

where $\boldsymbol{Q}$ is the acoustic tensor with its components defined as

$$Q_{ij} = \mathbb{A}^0_{ipjq}\hat{n}_p\hat{n}_q. \tag{14}$$

The associated strong ellipticity condition implies

$$Q_{ij}\hat{m}_i\hat{m}_j \equiv \mathbb{A}^0_{ipjq}\hat{n}_p\hat{n}_q\hat{m}_i\hat{m}_j > 0. \tag{15}$$

Thus, the loss of stability is associated with the condition $Q_{ij}\hat{m}_i\hat{m}_j = 0$. In the context of the heterogeneous composites, the loss of ellipticity analysis requires the determination of the effective tensor of elastic moduli, and, thus, identifies the onset of longwave or macroscopic instabilities.

2.3 Analysis of microscopic instability

To predict the instabilities developing at the length scales comparable with the composite microstructures, the Bloch-Floquet analysis of small amplitude deformations (superimposed on finite deformation) can be employed. Consider a composite with 2D rectangular cells with single-sized stiff inclusion in the center of each cell, see Fig. 1. Taking $\boldsymbol{Y}$ as the smallest repeating unit of the periodic structure of the infinite structure, namely, the initial primitive cell. The initial primitive cell $\boldsymbol{Y}$ can be identified by a rectangular spanned by the vectors $\overrightarrow{AB} = a\boldsymbol{e}_1$ and $\overrightarrow{AC} = b\boldsymbol{e}_2$, where $\boldsymbol{e}_1$ and $\boldsymbol{e}_2$ are Cartesian basis vectors; a and b denote the width and length of the primitive cell, respectively. The geometry can be parameterized through periodicity aspect ratio $\eta = a/b$ and inclusion spacing ratio $\xi = d/b$, where d is the diameter of the inclusion. However, once the bifurcation occurs, the initial primitive cell $\boldsymbol{Y}$ is no longer the smallest repeating unit of the periodic structure, namely, the initial $\boldsymbol{Y}$- periodicity

breaks, and the composite attains a new periodicity with an enlarged primitive cell as the smallest repeating unit, namely, $\boldsymbol{pY}$- periodicity, where vector $\boldsymbol{p} = (p_1,\ p_2)$ defines the size of the enlarged primitive cell. For example, see Fig. 1, the initial primitive cell can be characterized by $\boldsymbol{p} = (1,\ 1)$. After the bifurcation, the enlarged primitive cell can be characterized by $\boldsymbol{p} = (2,\ 2)$.

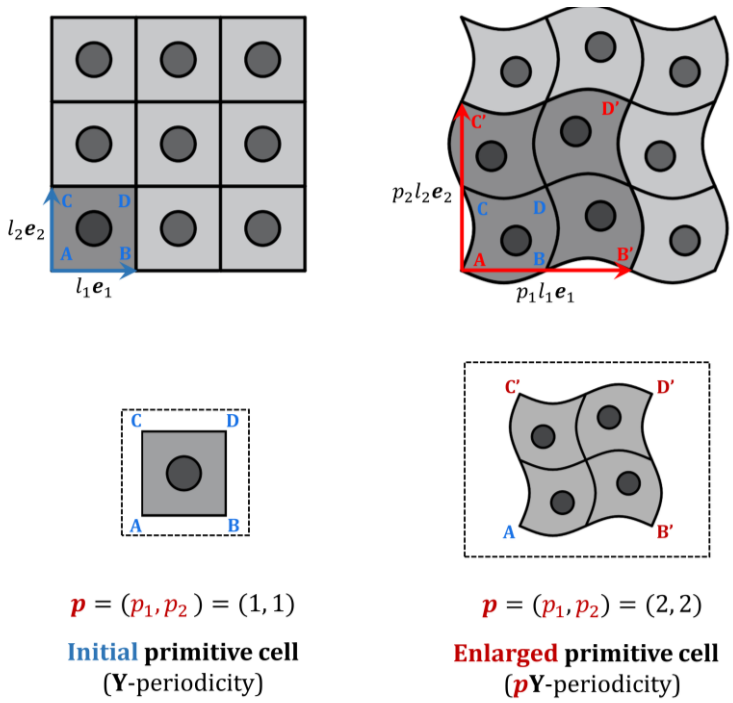

Fig. 1 Schematic composite microstructure with stiff circular inclusions periodically distributed in soft matrices.

Thus, at bifurcation, the material space satisfies the periodic conditions

$$\left(\boldsymbol{X} + p_j l_j \boldsymbol{a}_j\right) = \psi(\boldsymbol{X}), \qquad j = 1, 2. \tag{16}$$

for any point $\boldsymbol{X}$ in space. The space should also satisfy the classical Bloch condition

$$\left(\boldsymbol{X} + p_j l_j \boldsymbol{a}_j\right) = \psi(\boldsymbol{X}) \exp\left[i\boldsymbol{k}_0 \cdot \left(p_j l_j \boldsymbol{a}_j\right)\right], \qquad j = 1, 2. \tag{17}$$

Therefore, we must have

$$\exp\left[i\boldsymbol{k}_0 \cdot \left(p_j l_j \boldsymbol{a}_j\right)\right] = 1, \qquad j = 1, 2. \tag{18}$$

which can only be accomplished through k_0 in the form

$$\boldsymbol{k}_0 = k_1\boldsymbol{e}_1 + k_2\boldsymbol{e}_2, \tag{19}$$

where the wavenumbers

$$k_1 = \frac{1}{p_1}, \qquad k_2 = \frac{1}{p_2}. \tag{20}$$

Therefore, the bifurcation mode of the instability can also be characterized by the wavenumber of the Bloch condition $\boldsymbol{k}_0$, namely, the critical wavenumber. Moreover, we can further identify two different types of bifurcation modes based on the magnitude of $\boldsymbol{k}_0$, while $\boldsymbol{k}_0 > 0$ corresponds to a microscopic instability and $\boldsymbol{k}_0 \to 0$ corresponds to a macroscopic or longwave instability. The latter case corresponds to the loss of ellipticity at the macroscopic scale, which is discussed in section 2.2.

2.4 Constitutive models

The behavior of the stiff inclusion and soft matrix materials in this study is described by the nearly incompressible neo-Hookean strain energy density function, namely,

$$\mathrm{W}^{(\mathrm{r})} = \frac{\mu^{(\mathrm{r})}}{2}(I_1 - 3) + \frac{\kappa^{(\mathrm{r})}}{2}(J-1)^2, \tag{21}$$

where $\mu^{(\mathrm{r})}$ is the initial shear modulus, $\kappa^{(\mathrm{r})}$ is the bulk modulus, and $I_1 = \mathrm{tr}\boldsymbol{C}$ is the first invariant of the right Cauchy-Green tensor $\boldsymbol{C} = \boldsymbol{F}^{\mathrm{T}}\boldsymbol{F}$. The superscript (r) indicates the properties of different material phases; for example, $(\mathrm{r}) = (\mathrm{m})$ denotes the stiff inclusion phases, and $(\mathrm{r}) = (\mathrm{i})$ denotes the soft matrix phases. We introduce the ratio $\Lambda = \kappa^{(\mathrm{r})}/\mu^{(\mathrm{r})}$ representing the material compressibility, and assign a high ratio, $\Lambda = 10^3$, to maintain a nearly incompressible behavior of the material. We select the inclusion-to-matrix ratio of shear moduli $\mu^{(\mathrm{i})}/\mu^{(\mathrm{m})} = 10^3$. Therefore, stiff inclusions almost do not deform, and the

deformation is mostly accommodated by the soft matrix.

3. Numerical modeling

3.1 Bloch-Floquet analysis

We implement a 2-step Bloch-Floquet analysis to identify the onset of instability and corresponding critical wavenumber in the particulate composite.

3.1.1 2D Analysis (single-sized inclusion)

First, in-plane unidirectional compression is applied by imposing the periodic boundary conditions on boundary pair $AB-CD$ and $AC-BD$ as

$$\boldsymbol{u}_{src}-\boldsymbol{u}_{dst}=(\bar{\boldsymbol{F}}-\boldsymbol{I})(\boldsymbol{X}|_{src}-\boldsymbol{X}|_{dst})=\bar{\boldsymbol{H}}(\boldsymbol{X}|_{src}-\boldsymbol{X}|_{dst}), \tag{22}$$

where $\boldsymbol{u}_{src}$ and $\boldsymbol{u}_{dst}$ represents the displacement of an arbitrary pair of source and destination points periodically located on boundary pair AB and CD, respectively; $\bar{\boldsymbol{F}}$ denotes the average deformation gradient, and $\bar{\boldsymbol{H}}=\bar{\boldsymbol{F}}-\boldsymbol{I}$ denotes the average displacement gradient. Thus, the applied uniaxial compression loading is defined as

$$\bar{\boldsymbol{H}}=(\lambda_1-1)\boldsymbol{e}_1\otimes\boldsymbol{e}_1+(\lambda_2-1)\boldsymbol{e}_2\otimes\boldsymbol{e}_2, \tag{23}$$

where λ_1 and λ_2 are the principal stretch ratios in the direction of $\boldsymbol{e}_1$ and $\boldsymbol{e}_2$, respectively. The compressive loading level is prescribed via the average compressive strain $\varepsilon=1-\lambda_2$. λ_1 is defined via $\lambda_1\lambda_2=1$ according to the incompressibility of materials.

Second, we employ the Bloch–Floquet analysis superimposed on the deformed state(Bertoldi et al., 2008). The Floquet periodic conditions relate the incremental displacement fields $\boldsymbol{u}$ via

$$\boldsymbol{u}(\boldsymbol{X}+\boldsymbol{R})=\boldsymbol{u}(\boldsymbol{X})e^{i\boldsymbol{K}\cdot\boldsymbol{R}}, \tag{24}$$

where $\boldsymbol{K} = K_1\boldsymbol{e}_1 + K_2\boldsymbol{e}_2$ is the Bloch wave vector, and $\boldsymbol{R} = R_1 a\boldsymbol{e}_1 + R_2 b\boldsymbol{e}_2$ is a vector that denotes the initial periodicity of the composite with arbitrary integers R_1, R_2. In FEA, the Bloch–Floquet analysis is performed by solving the eigenvalue problem with Floquet boundary conditions imposed on the boundary pairs of the primitive unit cell read as $\boldsymbol{u}_{AB} = \boldsymbol{u}_{CD}e^{-i\boldsymbol{K}\cdot(\boldsymbol{R}_{AB}-\boldsymbol{R}_{CD})}$ and $\boldsymbol{u}_{BD} = \boldsymbol{u}_{AC}e^{-i\boldsymbol{K}\cdot(\boldsymbol{R}_{BD}-\boldsymbol{R}_{AC})}$. Here, the normalized components of the wavenumber are $k_1 = K_1 a/2\pi$ and $k_2 = K_2 b/2\pi$ in the undeformed configuration. Through the numerical analysis, we determine the lowest critical loading level (critical strain ε^{cr}) for which a zero eigenvalue occurs at the corresponding critical wavenumber k^{cr} (k_1^{cr} or k_2^{cr}). We refer to the cases with $k^{cr} \to 0$ as the longwave or macroscopic instability, and microscopic instabilities otherwise. We note that – throughout our calculations – the instabilities are found to develop only in the direction of compression (direction of $\boldsymbol{e}_2$) for all considered cases. Therefore, we report the corresponding critical wavenumber as $k^{cr} = k_2^{cr}$.

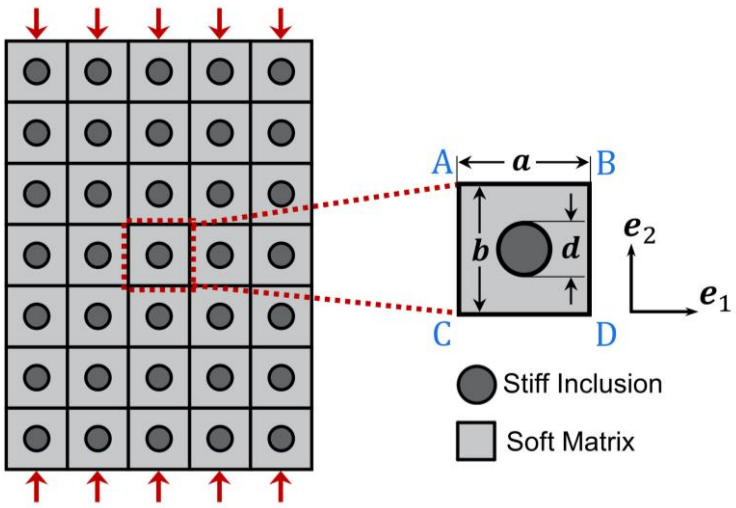

Fig. 2 Schematic composite microstructure with stiff circular inclusions periodically distributed in soft matrices.

The numerical procedure illustrated in Fig. 3 shows a typical case of identifying ε^{cr} and k_2^{cr}. For each geometric configuration (in this case, it is $\xi = 0.45$ and $\eta = 1.75$), in the first

step, we apply a compressive strain ε. Next, we import the compressed solution to the second step, where the associated eigenvalue problem with Floquet conditions Eq. (24) is solved. By repeating step 1 and 2, we scan the normalized wavenumbers k_2 in the range from 0 to 0.5, solve the lowest normalized eigenfrequency $f_n = \frac{\omega d}{2\pi}\sqrt{\rho/\mu^{(m)}}$ (ω is the angular frequency and $\rho = \rho^{(m)} = \rho^{(i)}$ is the mass density of the material), and finally get the dispersion relation $f_n(k_2) - k_2$ under given ε, see continues curves in in Fig. 3. Through this procedure, we can observe that the curves corresponding to $\varepsilon \leq 0.34232$ do not intersect with x-axis, except with the trivial point $f_n(0) = 0$ corresponding to the rigid body motion. However, an increase in the compressive strain level leads to the appearance of a zero-point at $k_2^{cr} \neq 0$. The corresponding values are identified as critical strain, ε^{cr}, and critical wavenumber k_2^{cr}. Here, we distinguish the following cases: $k_2^{cr} > 0$ is identified as the microscopic instability, and $k_2^{cr} \to 0$ ($k_2^{cr} \neq 0$) is identified as the longwave or macroscopic instability.

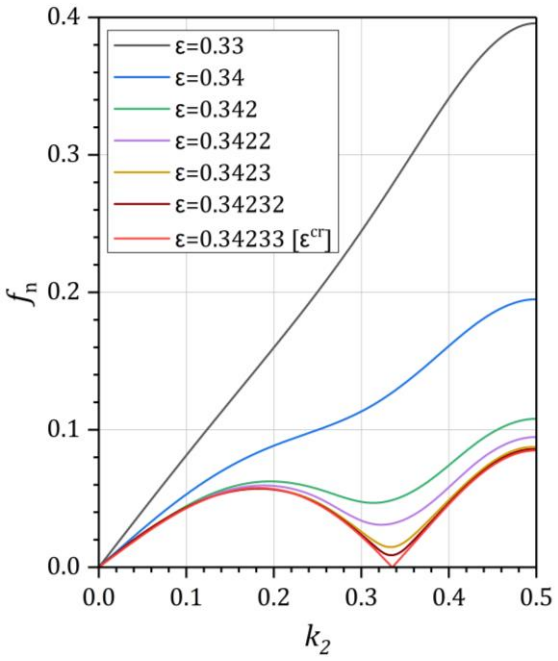

Fig. 3 Dispersion curves of the composite subjected to increasing levels of compressive strains.

3.1.2 2D Analysis (two different-sized inclusions)

In this part, we consider a particulate composite with two different-sized inclusions vertically and periodically distributed in 2D rectangular primitive unit cell, as shown in Fig. 4a. The primitive unit cell consists of an upper-part cell with the smaller inclusion (with diameter d_2), and a lower-part cell with the larger inclusion (with diameter d_1). The width of the primitive unit cell is denoted by a, and the length of the upper- and lower-part cells are denoted by b_2 and b_1, respectively. For this model, we specifically focus on the interaction between the vertically distributed inclusions with different sizes and try to minimize the interaction between neighboring inclusion columns. Therefore, we model the primitive cell with a large enough aspect ratio defined by a constant ratio $a/b_1 = 8$, and modify the height of the upper-part cell and the diameter of the two different-sized inclusions to alter the diameter contrast ratio $k_d = d_2/d_1$, while keeping the same spacing ratio for both the upper- and lower-part cell as $\xi = d_1/b_1 = d_2/b_2$. For example, with the same spacing ratio $\xi = 0.6$, the composites with two different-sized inclusions corresponding to the diameter contrast ratio $k_d = 1$, $k_d = 0.2$ and $k_d \to 0$ are shown in Fig. 4b, c and d, respectively. We observe that, with $k_d = 1$, the two inclusions have the same size, and the behavior of the composite should be identical to the single-sized inclusion model. With the diameter contrast ratio reduced to $k_d = 0.2$, the lower part keeps the same, while the diameter of the smaller inclusion, together with the height of the upper-part cell, is reduced to accommodate the reduced diameter contrast ratio. When the diameter contrast ratio k_d decreases to nearly zero, the upper part-cell is consequently reduced to an ignorable part, and apparently, and this composite is identical to the single-sized inclusion model.

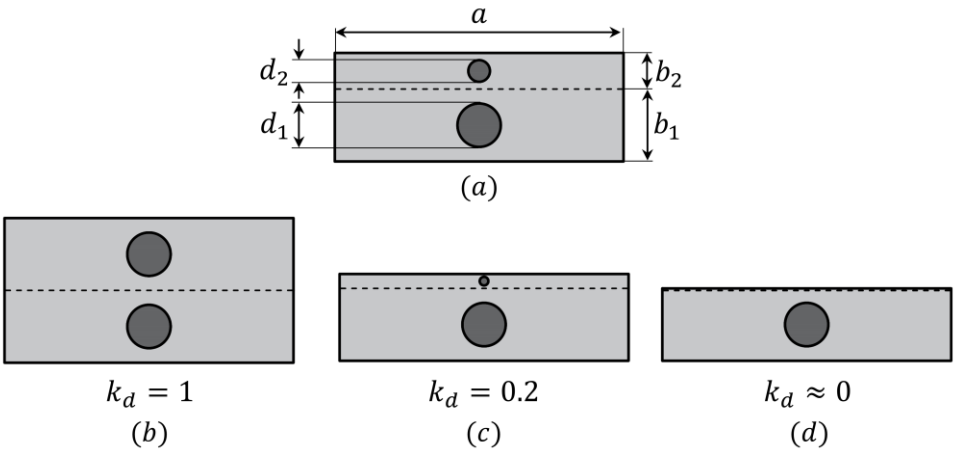

Fig. 4 a) Schematic composite microstructure with two different-sized stiff circular inclusions periodically distributed in soft matrices; Schematic composite with inclusion diameter contrast ratio b) $k_d = 1$, c) $k_d = 0.2$, d) $k_d \approx 0$.

Next, we implement the Bloch-Floquet analysis based on the two different-sized inclusion model with the same two-step method described in Sec. 3.1.1. The Floquet periodic conditions applied on the two boundary pairs are the same as described in Eq. (24). Specifically for the model with two different-sized inclusions, we have $\boldsymbol{R} = R_1 a\boldsymbol{e}_1 + R_2(b_1 + b_2)\boldsymbol{e}_2$. Correspondingly, the normalization of the wavenumber is altered to $k_1 = K_1 a/2\pi$ and $k_2 = K_2(b_1 + b_2)/4\pi$ to ensure that, for the model with two different-sized inclusions corresponding to $k_d = 1$, the derived wavenumber is the same as that derived in the single-sized inclusion model. Notice that, with this normalization, for the model with $k_d \approx 0$, the derived wavenumber should be exactly a half of the wavenumber derived in the single-sized inclusion model.

3.1.3 Bloch-Floquet analysis in post-buckling regime

In this part, we present an integrated analysis where the Bloch–Floquet analysis is superimposed on the post-buckling state of RVE (see Fig. 5b) corresponding to its initial

periodicity exactly being doubled. The procedure of this analysis is typically the same as the two-step Bloch-Floquet analysis described in Sec. 3.1.1. For the first step, the RVE is compressed to deform beyond its first buckling being triggered, namely, to deform in its post-buckling regime. The in-plane unidirectional compression is imposed on the two boundary pairs $AB-CD$ and $AC-BD$ via the same definitions described in Eq. (22) and Eq.(23) in Sec. 3.1.1. In the second, step, the Floquet periodic conditions are applied on the two boundary pairs the same as described in Eq. (24). Specifically for the RVE with two different-sized inclusions, we have $\boldsymbol{R}=R_1 a\boldsymbol{e}_1+R_2(2b)\boldsymbol{e}_2$. Through the numerical analysis, we can identify the occurrence of the secondary buckling at the lowest strain level (namely, the critical strain ε_{II}^{cr}) while a zero eigenvalue emerges at a critical wavenumber k_{II}^{cr}. We refer to the cases with $k_{II}^{cr}\to 0$ as the longwave or macroscopic instability, and cases with $k_{II}^{cr}>0$ as microscopic instabilities. Throughout our calculation, we observe that the secondary buckling is found to develop only in the direction of compression (the direction of $\boldsymbol{e}_2$) for all considered cases. Here and thereafter, the subscript "II" denotes the critical characteristics of the secondary buckling, and "I" denotes those of the first stage buckling.

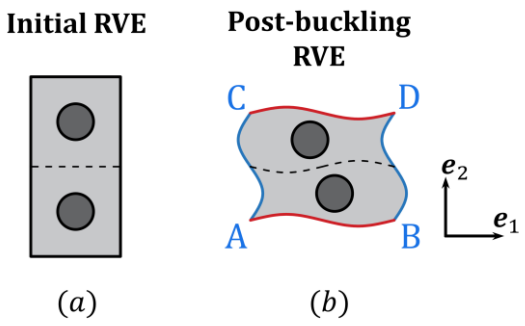

Fig. 5 Schematic representative volume element with two composite unit cells in a) the initial undeformed state and b) its post-buckling regime corresponding to its initial periodicity being exactly doubled.

3.1.4 3D Analysis

To perform the 3D analysis, we construct a composite with a single sphere inclusion embedded in a cuboid primitive unit cell, as shown in Fig. 6. The width and length of the cell are defined as the same a; the height is defined by b and d is the diameter of the inclusion. The geometry can be parameterized through periodicity aspect ratio $\eta = a/b$ and inclusion spacing ratio $\xi = d/b$. The procedure of this analysis is typically the same as the two-step Bloch-Floquet analysis described in Sec. 3.1.1. For the first step, the uniaxial compression is applied via periodic boundary conditions imposed on the top-bottom surface pair as described in Eq. (22). For the 3D case, the displacement gradient is defined as

$$\bar{\boldsymbol{H}} = (\lambda_1 - 1)\boldsymbol{e}_1 \otimes \boldsymbol{e}_1 + (\lambda_2 - 1)\boldsymbol{e}_2 \otimes \boldsymbol{e}_2 + (\lambda_3 - 1)\boldsymbol{e}_3 \otimes \boldsymbol{e}_3, \tag{25}$$

where λ_1, λ_2 and λ_3 are the principal stretch ratios in the direction of $\boldsymbol{e}_1$, $\boldsymbol{e}_2$ and $\boldsymbol{e}_3$ respectively. The loading level is prescribed via the average compressive strain in the direction of compression (the direction of $\boldsymbol{e}_1$), defined as $\varepsilon = 1 - \lambda_1$, where λ_2 and λ_3 are defined via $\lambda_2 = \lambda_3$ and $\lambda_1\lambda_2\lambda_3 = 1$ according to the incompressibility of materials. For the second step, the Bloch–Floquet analysis is performed by solving the eigenvalue problem with Floquet boundary conditions imposed on the three surface pairs of the primitive unit cell read as

$\boldsymbol{u}_{top} = \boldsymbol{u}_{bottom} e^{-i\boldsymbol{K}\cdot(\boldsymbol{R}_{top} - \boldsymbol{R}_{bottom})}$,

$\boldsymbol{u}_{right} = \boldsymbol{u}_{left} e^{-i\boldsymbol{K}\cdot(\boldsymbol{R}_{right} - \boldsymbol{R}_{left})}$,

$\boldsymbol{u}_{front} = \boldsymbol{u}_{back} e^{-i\boldsymbol{K}\cdot(\boldsymbol{R}_{front} - \boldsymbol{R}_{back})}$.

Here, the normalized components of the wavenumber are $k_1 = K_1 b/2\pi$, $k_2 = K_2 a/2\pi$ and $k_3 = K_3 a/2\pi$ in the undeformed configuration. Throughout our calculation, we observe that the buckling in the 3D particulate composite is found to develop only in the direction of

compression (the direction of $\boldsymbol{e}_2$) for all considered cases. Therefore, here and thereafter in this paper, we report the corresponding critical wavenumber of the 3D particulate composite as $k^{cr} = k_1^{cr}$.

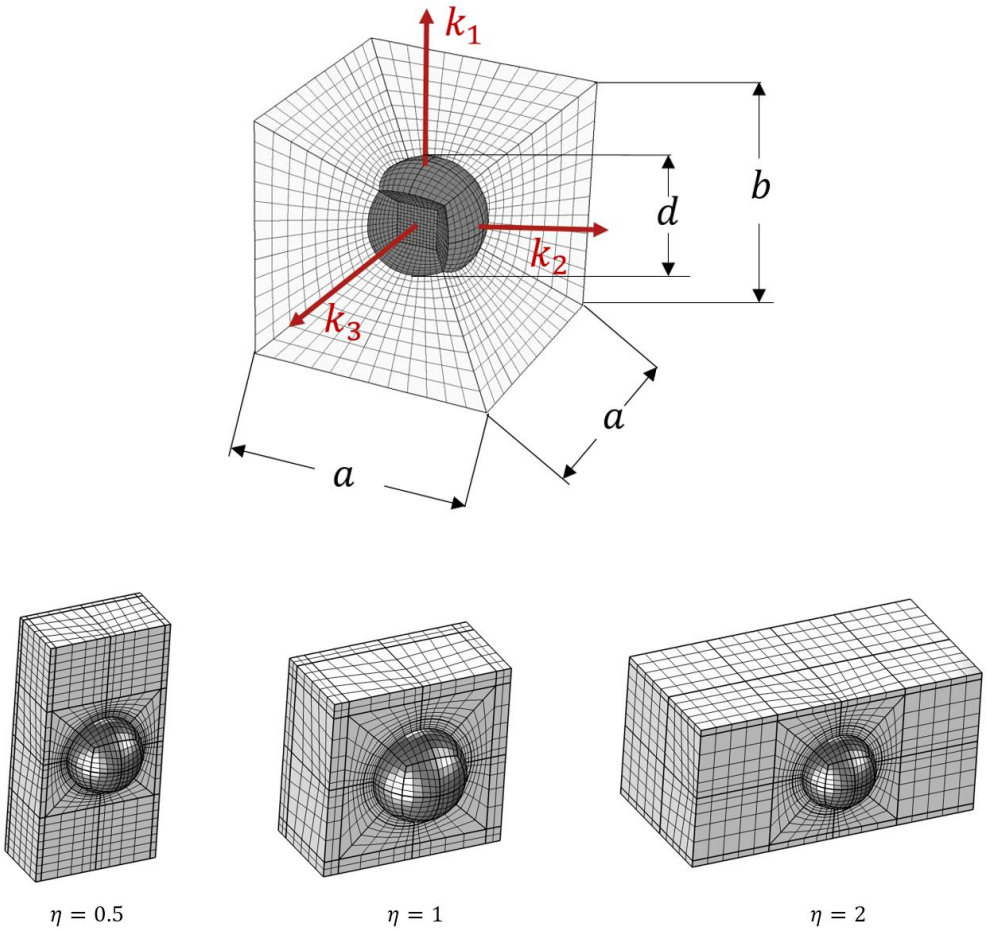

Fig. 6 Schematic 3d composite microstructure with stiff sphere inclusions periodically distributed in cuboid soft matrices.

3.2 Energy quasi-convexification analysis

In this part, we illustrate the so-called energy landscapes of the finitely deformed particulate composite. In the analysis, we calculate the macroscopic response of a single unit cell deformed beyond the possible instability point (similar to the standard post-buckling regime simulations (Li et al., 2019b; Bertoldi et al., 2008)). Then, the quasi-convexification of

the calculated elastic strain energy function $W(\boldsymbol{F})$ in the applied deformation gradient $\boldsymbol{F}$ is examined.

A strain energy function $W(\boldsymbol{F})$ is said to be quasi-convex (Morrey, 1952) if

$$W(\boldsymbol{F}) \leq \frac{1}{|D|}\int_{D} W(\boldsymbol{F} + Grad\, \boldsymbol{u}\,(\boldsymbol{X}))d\boldsymbol{X} \tag{26}$$

for every bounded region D and for every smooth function with compact support $\boldsymbol{u}\,(\boldsymbol{X})$. Note that the quasi-convexification of the energy with the volumetric constraints (such as incompressibility constraint) is rank-one convexification (Conti et al., 2008). In the following study, we identify the critical conditions for the loss of quasi-convexity or 'relaxation' in the strain energy function.

We consider the composites subjected to simultaneously applied compressive strain and pure shear deformations (see Fig. 7b). The corresponding macroscopic deformation gradient $\overline{\boldsymbol{F}}$ is

$$\overline{\boldsymbol{F}} = H_{11}\boldsymbol{e}_1 \otimes \boldsymbol{e}_1 + \varepsilon \boldsymbol{e}_2 \otimes \boldsymbol{e}_2 \pm \gamma \boldsymbol{e}_1 \otimes \boldsymbol{e}_2 + \boldsymbol{I}, \tag{27}$$

where ε and γ are the compressive strain measure and amount of shear, respectively. Note that H_{11} is determined by the corresponding traction-free boundary condition. The effective (or homogenized) strain energy W stored in the unit cell under prescribed deformations is computed and normalized via

$$\widetilde{W}(\overline{\boldsymbol{F}}) = \frac{1}{\mu^{(m)}}\frac{1}{\Omega_0}\int_{\Omega_0} W(\boldsymbol{X}, \boldsymbol{F})dV_{\boldsymbol{X}}. \tag{28}$$

Next, we compute the energy landscape of the composite cell based on $\widetilde{W}(\varepsilon, \gamma)$ as a function of the compressive strain ε and amount of shear γ. According to the condition of quasi-convexity in Eq. (26), the 'relaxation' or loss of quasi-convexity of the effective energy

function is associated with the condition

$$\widetilde{W}(\varepsilon,\gamma) = \widetilde{W}(\varepsilon,\gamma = 0) \tag{29}$$

for any non-zero amount of shear γ. Finally, the lowest compressive strain ε, corresponding to the 'relaxation' of the effective energy function $\widetilde{W}$, is identified as the critical strain level.

Fig. 7a shows an example of the energy landscape corresponding to geometrical parameters $\xi = 0.7$ and $\eta = 1$, where the normalized energy $\widetilde{W}$ is plotted as a function of γ and ε. Fig. 7c shows the curves of $\widetilde{W}$ as a function of γ, which are derived from the energy landscape in Fig. 7a through making cross-sections at given ε (see, for example, the curve corresponding to $\varepsilon = 0.18$ in Fig. 7c is derived from the cut curve $\widetilde{W}(\varepsilon = 0.18,\gamma)$ in Fig. 7a). We observe that, for curves corresponding to a small ε (see, for example, the curve corresponding to $\varepsilon = 0.05$ in Fig. 7c), the stored-energy increases with an increase in γ. This implies that the shearing mode is not energetically favorable under this level of compression. Thus, the composite is considered in a stable state. For curves corresponding to a large ε (see, for example, the curve corresponding to $\varepsilon = 0.19$ in Fig. 7c), we observe that the stored energy decreases with an increase in γ. This, however, implies that the shearing mode now becomes an energetically favorable mode. Thus, the composite is considered in an unstable state. In this state, the composite will run into a bifurcation with a slight disturbance, that is, the loss of stability. Finally, as shown in Fig. 7d, the onset of instability is identified at the critical strain ε^{cr} where a numerically determined relaxation, $\widetilde{W}_\gamma^0(\varepsilon) = \widetilde{W}(\varepsilon,\gamma = 0.001) - \widetilde{W}(\varepsilon,\gamma = 0) = 0$ is detected. (see, for example, in Fig. 7b, the critical strain is identified as $\varepsilon^{cr} = 0.1407$).

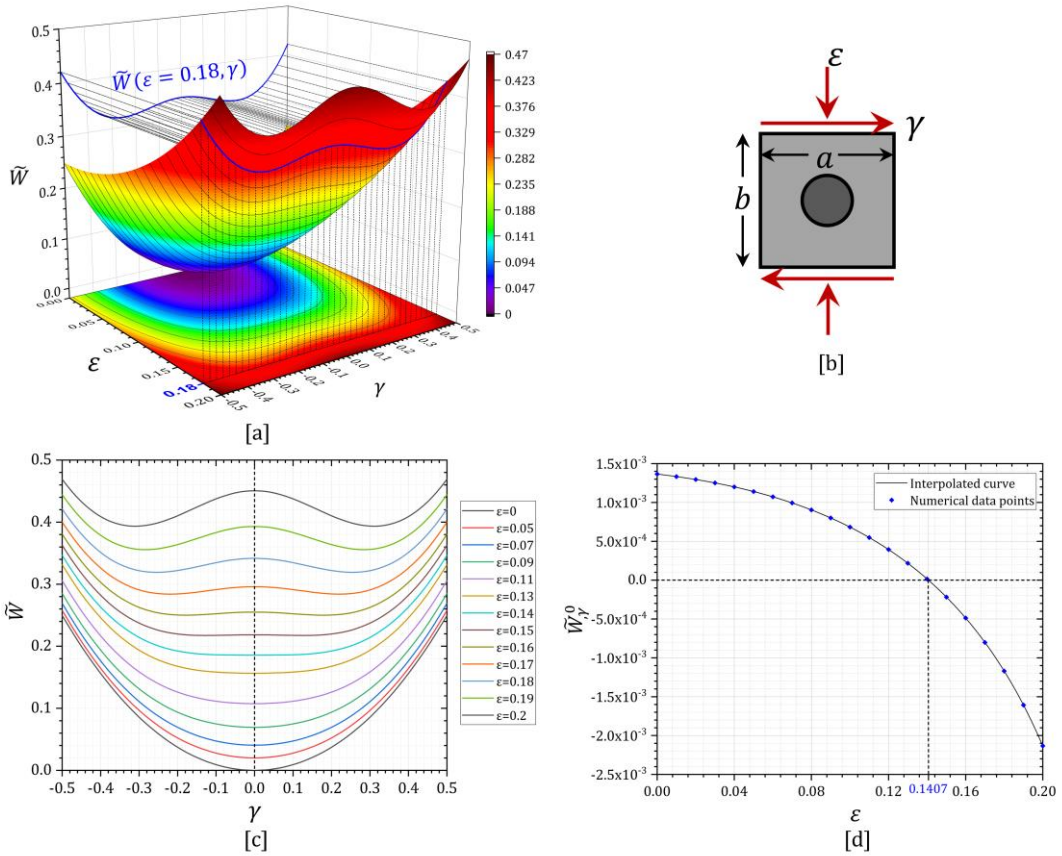

Fig. 7 a) Landscape of the normalized stored-energy $\widetilde{W}$ as a function of the compressive strain ε and shear strain γ (corresponding to $\xi = 0.7$ and $\eta = 1$) b) Schematic composite cell subjected to simultaneously applied compressive strain and pure shear deformations
c) The curves of normalized stored-energy with various γ and fixed ε
d) The curve for numerical determination of relaxation

3.3 Post-buckling analysis

3.3.1 Geometric modeling

To perform the post-buckling analysis, we construct a *representative volume element* (RVE) (Bertoldi et al., 2008) with a large number ($N = 80$) of unit cells. The RVE is enclosed by four boundaries (AB, CD, AC, and BD), defined by nodes $A, B, C,$ and D (see Fig. 8). We apply uniaxial compression *quasi-statically* via periodic boundary conditions imposed on the boundary pair $AB - CD$ and $AC - BD$ as

$$\boldsymbol{u}_{src} - \boldsymbol{u}_{dst} = (\bar{\boldsymbol{F}} - \boldsymbol{I})(\boldsymbol{X}|_{src} - \boldsymbol{X}|_{dst}) = \bar{\boldsymbol{H}}(\boldsymbol{X}|_{src} - \boldsymbol{X}|_{dst}), \tag{30}$$

where $\boldsymbol{u}_{src}$ and $\boldsymbol{u}_{dst}$ represent the displacement of an arbitrary pair of points periodically located on the *source* and *destination* boundary of the boundary pair, respectively; $\bar{\boldsymbol{F}}$ denotes the average deformation gradient, $\boldsymbol{I}$ denotes the identity tensor and $\bar{\boldsymbol{H}} = \bar{\boldsymbol{F}} - \boldsymbol{I}$ denotes the average displacement gradient. We apply the in-plane unidirectional compression to the RVE in the direction of $\boldsymbol{e}_2$ via the displacement gradient defined ass

$$\bar{\boldsymbol{H}} = (\lambda_1 - 1)\boldsymbol{e}_1 \otimes \boldsymbol{e}_1 + (\lambda_2 - 1)\boldsymbol{e}_2 \otimes \boldsymbol{e}_2, \tag{31}$$

where λ_1 and λ_2 are the principal stretch ratios in the direction of $\boldsymbol{e}_1$ and $\boldsymbol{e}_2$, respectively. The compressive loading level is prescribed via the average compressive strain $\varepsilon = 1 - \lambda_2$. λ_1 is defined via $\lambda_1\lambda_2 = 1$ according to the incompressibility of materials.

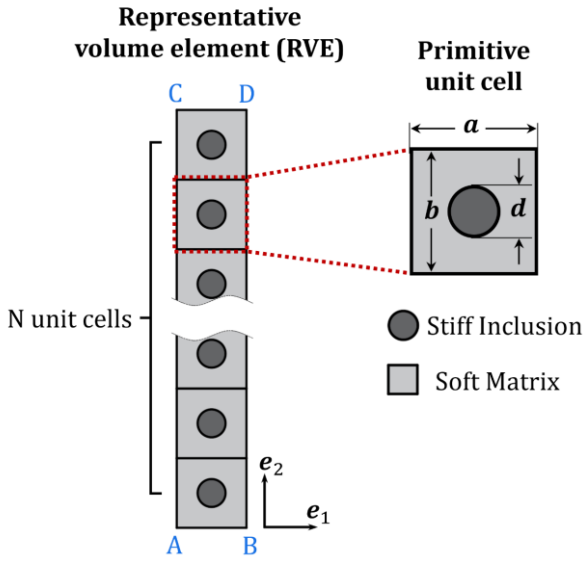

Fig. 8 Schematic composite microstructure with stiff circular inclusions periodically distributed in soft matrices.

As a perturbation to trigger instabilities, geometrical imperfection is introduced in terms of a slight alternation of the shape and position of the stiff inclusions. Specifically, as shown in Fig. 9, the inclusions are modeled as nearly-circular *ellipses*, where the geometrical differences

are introduced independently onto the major diameter L_n, minor diameter S_n and the position X_n of the center of the nth inclusion, namely,

$$L_n = d + \Delta L_n,$$

$$S_n = d + \Delta S_n,$$

$$X_n = X + \Delta X_n,$$

where d is the diameter of the perfect circular inclusion and X_n is the acuate horizontal position of the center of the nth inclusion; ΔL_n, ΔS_n, and ΔX_n are random deviations. Note that the imperfections shown in Fig. 9b are significantly scaled for better illustration, since the original imperfection is too small to be visually discernible. Next, we generated three sets of random deviations,

$$\{\Delta L_n\} := \Delta L_1, \Delta L_2, \Delta L_3 \ldots, \Delta L_N,$$

$$\{\Delta S_n\} := \Delta S_1, \Delta S_2, \Delta S_3 \ldots, \Delta S_N,$$

$$\{\Delta X_n\} := \Delta X_1, \Delta X_2, \Delta X_3 \ldots, \Delta X_N,$$

and use them to alter the inclusions in the numerical model (where N is the total number of inclusions modeled in an RVE). Moreover, the distribution of the random set is symmetric to zero and is arranged to stay within $K_{imp} \cdot d$, where K_{imp} is the amplitude of deviation.

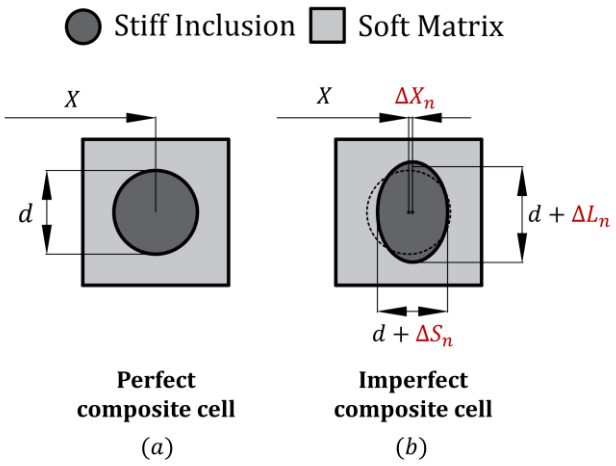

Fig. 9 (a) Schematic composite cell without geometric imperfection. (b) Schematic composite cell with geometric imperfections (the imperfections are significantly scaled in the figure for better illustration since the original imperfection is too small to be visually discernible)

To find the proper value of K_{imp} (with which the instabilities can be successfully triggered and the results are insensitive enough to the imperfections), we compare the results from numerical models with different K_{imp} (in particular, $K_{imp} = 10^{-2}$, 10^{-3}, 10^{-4}, 10^{-5}, 10^{-6} and 10^{-7}). The corresponding DFT results are shown in Fig. 10a at the compressive strain level $\varepsilon = 0.241$ (after the Bloch-Floquet critical strain $\varepsilon^{cr} = 0.2338$). We observe that, for a large enough amplitude of deviation (for example, $K_{imp} = 10^{-2}, 10^{-3}, 10^{-4}$), the instability was successfully trigged. However, the inclusion chains (the post-buckling pattern) are found to be frustrated because of overwhelming imperfections, resulting in jagged DFT curves. For small enough amplitudes of deviation (for example, $K_{imp} = 10^{-6}$ and 10^{-7}), the imperfection is too small that it fails to trigger the instability in numerical computation; thus, we find the DFT results maintain a zero line.

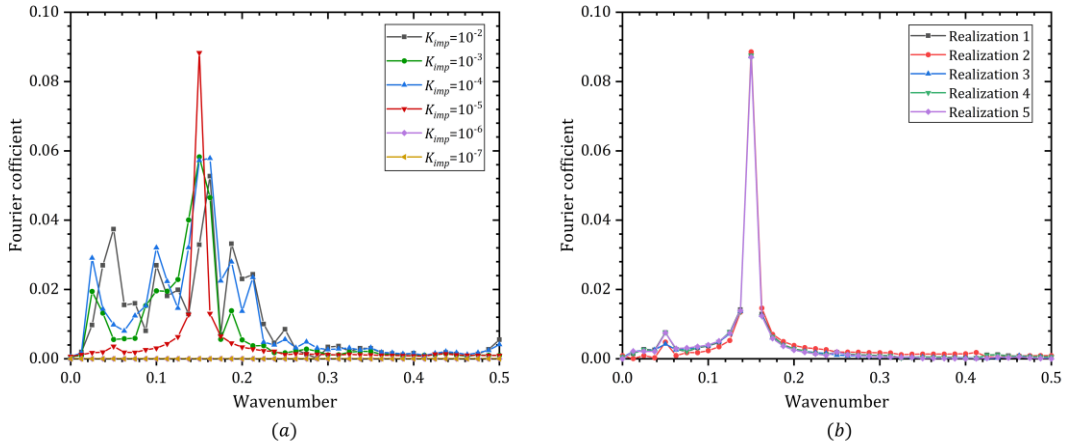

Fig. 10 The DFT results of the post-buckling development at compressive strain $\varepsilon = 0.241$ for numerical models with (a) various amplitudes of geometric imperfection ($K_{imp} = 10^{-2}, 10^{-3}, 10^{-4}, 10^{-5}, 10^{-5},$ and 10^{-7}); (b) different realizations of random imperfection with the same amplitude of geometric imperfection $K_{imp} = 10^{-5}$.

Our results indicate that, with an intermediate amplitude of deviation, $K_{imp} = 10^{-5}$, the instability pattern can be successfully triggered without being overwhelmed by the imperfections (see the red curve shown in Fig. 10a corresponding to $K_{imp} = 10^{-5}$). Moreover, to verify the insensitivity of the FEA results to specific realizations of the random imperfection, we compared five numerical models with independent realizations. The corresponding DFT results (where the peak corresponds to the critical wavenumber) are shown in Fig. 10b. Moreover, the derived critical strains corresponding to realizations 1 to 5 are found at $\varepsilon^{cr} =$ 0.23377, 0.23374, 0.23375, 0.23377, and 0.23378. These results demonstrate that, with an amplitude of deviation at $K_{imp} = 10^{-5}$, the critical strains and wavenumbers are insensitive enough to specific realizations of the random imperfection.

It should be noted that the imperfections introduced in our study are designed to trigger the instability without impacting the prediction of the composite's buckling behavior. However, they may not accurately reflect the imperfections in natural materials resulting from geometrical (Chen et al., 2019; Ding et al., 2019; Yu et al., 2022) or material (Hauseux et al.,

2017, 2018; Rappel et al., 2019) uncertainties. The prediction of the composite's buckling behavior may be affected by those uncertainties. Additionally, interphases between the composite constituents, which may occur during the material manufacturing processes, can potentially affect the instability characteristics (Arora et al., 2019). To quantify the influence of these uncertainties, multi-field coupled stochastic analyses can be employed (Elouneg et al., 2021; Mazier et al., 2022).

3.3.2 Characterization of post-buckling development

To correctly capture the onset of secondary buckling, and to analyze the critical wavenumber, we utilized a standard post-processing method that characterizes the post-buckling structure obtained from FEA via discrete Fourier transformation (DFT). Specifically, we track the position displacement of the inclusion centers throughout the first and the secondary buckling. This procedure starts with building a representation of the stiff inclusions by a discrete wavy curve that connects their centers. Note that we only consider the horizontal displacement of the inclusion centers (in $\boldsymbol{e}_1$ direction), and the deformations of the stiff inclusions themselves are neglected. Next, we apply a discrete Fourier transform (DFT) on the obtained inclusion center connecting curve to find its wavenumber components and corresponding Fourier coefficient. Given a discrete curve being defined by the positions of inclusions, namely, $\{x_n\} := x_1, x_2, x_3 \dots, x_N$ in $\boldsymbol{e}_1$ direction, the DFT utilizes a set of discrete harmonic curves based on a fundamental wavenumber $1/N$ to reassemble the discrete curve $\{x_n\}$, where N is the number of inclusions in the RVE, and the corresponding wavenumber of the Kth harmonic curve is K/N. Through the discrete Fourier transformation,

we obtain the dependence of the Fourier coefficient f_K on the corresponding component wavenumber $k = K/N$ by solving the linear equation system

$$x_n = \sum_{K=0}^{N-1} f_K \cdot e^{i2\pi \frac{K}{N} n}. \tag{32}$$

Next, the DFT result is represented as a wavenumber spectrum $f_K = F(k)$, where f_K is Fourier coefficient and k is the component wavenumber ($k = 1/N,\ 2/N, ...,\ (N-1)/N,\ 1$). Finally, we identify the peak point in the DFT spectrum $f_K = F(k)$ (corresponding to the harmonic curve that dominates the post-buckling pattern) as the critical wavenumber. This results from the buckling wavelength being significantly larger than the size of RVE. Note that, with a finite-sized RVE, the DFT analysis will identify the longwave instabilities at the fundamental wavenumber $1/320$, corresponding to a single period of buckling pattern with the wavelength equal to the height of the RVE. If we use a larger number of unit cells in the RVE (for example, 640 cells), the longwave buckling will be identified with a critical wavenumber shifting down to $k = 1/640$.

4. Numerical results

4.1 Composite(2D) with single-sized inclusions

4.1.1 Bloch-Floquet prediction

4.1.1.1 Dependence of critical strain on geometric parameters

We start by examining the influence of the instability characteristics, such as critical strain and wavenumber, on the initial geometrical parameters of the periodic microstructure. Fig. 11 shows the dependence of the critical strain on the periodicity aspect ratio η for various fixed values of the inclusion spacing ratios ξ from 0.1 to 0.9. Note that, the admissible geometries

are restricted by $d < b$ and $d < a$, thus, limited the parameter space as $\eta > \xi$. Here and thereafter, the dotted and continuous curves correspond to longwave (or macroscopic) and microscopic instabilities, respectively.

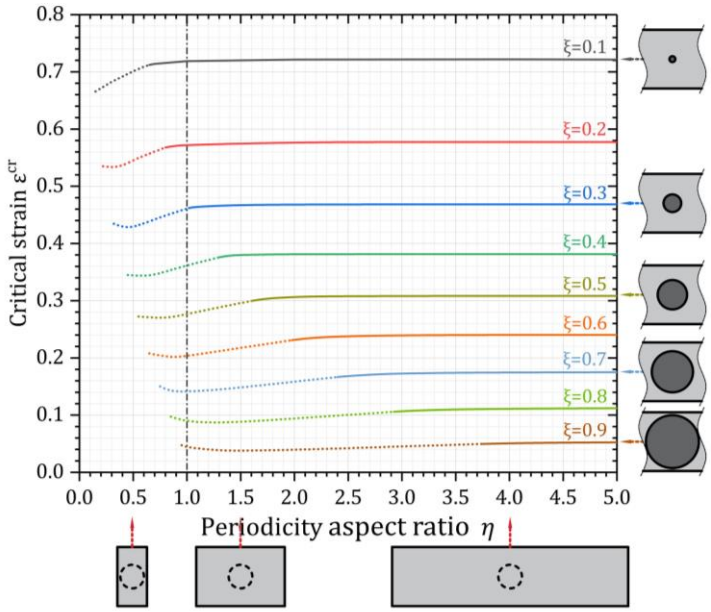

Fig. 11 The dependence of critical strain on periodicity aspect ratio with various spacing ratios. Dotted and continuous curves correspond to macroscopic and microscopic instabilities, respectively.

We observe that the composites with higher spacing ratios experience instabilities at lower compressive strains. In these composites, the inclusions are placed more closely in the compressive direction. Thus, the stiff inclusions are brought into their strong interactions at lower strain levels leading to earlier instability development. Interestingly, the dependence of the critical strain on the spacing periodicity ratio alters with a change in the inclusion spacing ratio. For composites with small spacing ratios, the critical strain ε^{cr} increases monotonically with an increase in η (see, for example, the black curve corresponding to $\xi = 0.1$ in Fig. 11). This behavior, however, changes to a non-monotonic one in the composite with low-to-moderate spacing ratios. Their curves decrease initially; however, after reaching their local minima, the critical strain increases with a further increase in the periodicity aspect ratio and

finally converges to a plateau. For example, for the composite with $\xi = 0.3$ (the blue curve in Fig. 11), ε^{cr} decrease initially, after reaching its local minimum $\varepsilon^{cr} = 0.426$ at $\eta = 0.45$, the curve starts to increase and eventually converges to a plateau after $\eta > 1.035$. The asymptotic values of the plateaus correspond to those initial configurations with an isolated or single column of inclusions embedded in the soft matrix.

This non-monotonic dependence is the manifestation of two different dominating buckling behaviors in the soft particulate systems. In particular, the composites with high periodicity aspect ratios exhibit laminate-like behavior (with the stiffer layers reinforced by the stiff inclusions); in these composites, the critical strain decreases as the periodicity aspect ratio decreases (corresponding to an increase in the effective volume fraction of the analogous reinforced layer). However, as the periodicity aspect ratio is decreased further, the buckling behavior changes as the inclusions are introduced into additional horizontal interactions. The introduced horizontal frustration forces the soft particulate system to seek a different buckling mechanism requiring higher strain levels. The transition in the buckling behavior can be illustrated by considering the soft composites with $\xi = 0.6$ (see the orange curve in Fig. 11). For the configurations with higher periodicity aspect ratios ($\eta \gtrsim 0.85$), the composites exhibit the laminate-like buckling behavior, and the critical strain decreases with a decrease in the inclusions spacing ratio. The behavior starts changing in the configurations with $\eta \approx 0.85$, and the critical strain increases with a decrease in η. For the composites with $\xi = 0.6$, the transition point corresponding to the local minimum of the curve is $\eta \approx 0.85$. The composites with large inclusion spacing ratios (larger inclusions) are characterized by a wider range of the periodicity aspect ratios, where they exhibit laminate-like buckling behavior (accompanied by

a decrease in the critical strain with a decrease in the periodicity aspect ratio). This is due to the fact that the additional horizontal particle interactions are more likely to be introduced in the composites with larger stiff inclusions. Correspondingly, the transition point shifts towards the large periodicity aspect ratio values with an increase in ξ. For example, the composites with $\xi = 0.3$ and 0.9 have their transition points at $\eta \approx 0.45$ and $\eta \approx 1.5$, respectively.

We further illustrate the transition between these two different system behaviors in Fig. 12 for the soft composites with $\xi = 0.6$ and $\eta = 0.62, 0.85, 1.5,$ and 2. Fig. 12 shows the deformation field distribution with the vertical strain component ε_{22}. When the compressive deformation is high enough, the inclusions are pushed close to each other in the compressive direction. The composite with higher periodicity aspect ratios (for example, the composite with $\eta = 2$ in Fig. 12) forms the columns of compactly lined up inclusions in the deformed configuration. The deformed system creates the analogous "effective stiffer layers" and "softer matrix layers" (see the deformed composite with $\eta = 2$ in Fig. 12). The particulate composite is observed to exhibit laminate-like buckling behavior. When the periodicity aspect ratio is decreased (compare the composite cells with $\eta = 2$ and 1.5 in Fig. 12), the effective stiffer layers are placed closer to each other, resulting in an increase in the analogous volume fraction of the effective stiffer phase. Similar to the laminate buckling behavior (J. Li, Slesarenko, et al., 2019c; Y. Li et al., 2013), the composites are characterized by a decrease in the critical strain as the periodicity ratio is decreased. In particular, the critical strain decreases from $\varepsilon^{cr} = 0.231$ to $\varepsilon^{cr} = 0.217$ in the composites with η decreased from 2 to 1.5.

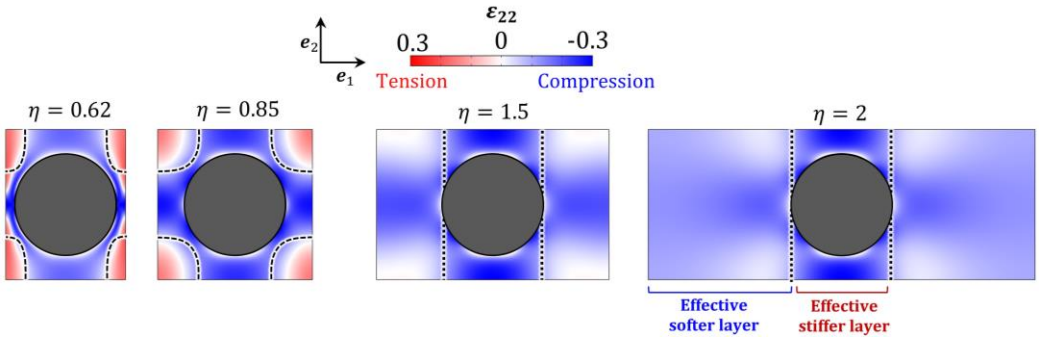

Fig. 12 Distribution of strain field, ε_{22}, in the composite with $\xi = 0.6$ under the applied average compressive strain $\varepsilon = 0.24$ with various periodicity aspect ratios.

As the periodicity aspect ratio further decreases, the composite configurations enter into the transition buckling behavior. Such configuration is illustrated in Fig. 12 for the composite with the periodicity aspect ratio $\eta = 0.85$. The columns of stiff inclusions are placed close to each other so that the inclusions are introduced into additional horizontal interactions. This is illustrated by the deformation distribution field showing the strong interaction of the stiff inclusions in both vertical and horizontal directions. The proximity of the stiff inclusions columns hinders the buckling development and makes the structure more stable. This mechanism manifests in the increase of the critical strain when the periodicity aspect ratio is decreased further (beyond the transition minimum point). Thus, for example, the critical strain increases from 0.201 to 0.211 in the soft composites with $\eta = 0.85$ and $\eta = 0.62$ (shown in Fig. 12).

4.1.1.2 Dependence of critical wavenumber on geometric parameters

Next, we recall the essential feature of the failure curves, namely, the existence of a transition from macroscopic (or longwave) to microscopic instability mode occurring at a critical threshold value η^{th}. For example, the composite with $\xi = 0.6$ transits from

macroscopic to microscopic instability at the threshold value is $\eta^{th} \approx 1.975$, and the threshold values gradually increase with an increase in the spacing ratio. This transition of instability modes is characterized by the corresponding change in the critical wavenumber.

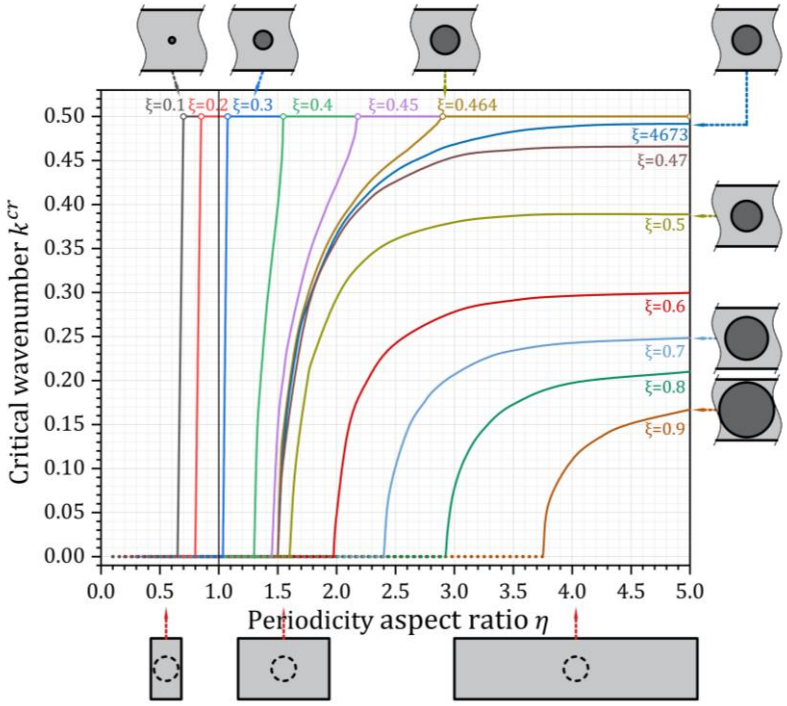

Fig. 13 The dependence of critical wavenumber on the periodicity aspect ratio with various spacing ratios. Dotted and continuous curves correspond to macroscopic and microscopic instabilities, respectively.

Fig. 13 shows the dependence of the critical wavenumber k^{cr} on the periodicity aspect ratio η, for various fixed values of the inclusion spacing ratios ξ from 0.1 to 0.9. We observe in Fig. 13 that the curves are characterized by the existence of macroscopic or longwave instability ($k^{cr} \to 0$) in the initial ranges of their periodicity aspect ratio lower than their threshold values η^{th}. The threshold value – after which a switch from macroscopic to microscopic buckling mode happens – is dictated by the initial spacing ratio value ξ. This transition from macro- to micro-instability modes happens rather rapidly in the composites with small initial spacing ratios. For example, in the composite with $\xi = 0.2$ (see the red

curve in Fig. 13), the wavenumber suddenly switches from $k^{cr} = 0$ to 0.5 at the threshold value $\eta^{th} \approx 0.8$. In the composites with higher periodicity aspect ratios, however, gradual transitions are observed; the corresponding critical wavenumbers continuously increase from zero until reaching the plateau value at the corresponding threshold value. For instance, in the composites with $\xi = 0.45$ (see the violet curve in Fig. 13), the wave number k^{cr} increases after the threshold value $\eta^{th} = 1.45$, and it reaches the maximum bound level of 0.5 at $\eta = 2.18$. After reaching the threshold value, the critical wavenumber does not change with a further increase in the periodicity aspect ratio η. For the composites with even higher spacing ratios, the critical wavenumber k^{cr} does not reach the upper bound value of 0.5; instead, the wavenumber approaches a lower-level plateau for a high enough η. For example, in the composites with $\xi = 0.6$, the critical wavenumber increases after the threshold value $\eta^{th} = 1.975$, followed by the curve flattening and asymptotically reaching the plateau value with $k^{cr} \to 0.31$.

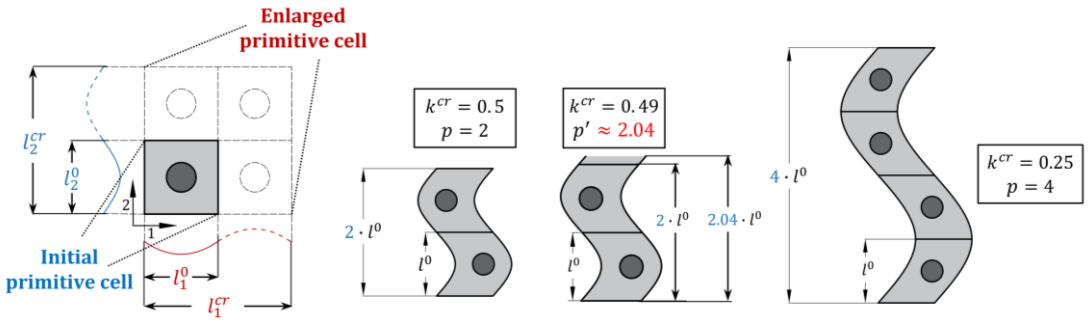

Fig. 14 Schematics of instability patterns based on initial primitive cells and enlarged primitive cells.

We schematically illustrate the corresponding instability patterns in Fig. 14. Prior to the onset of instabilities, the composite's periodicity is defined by the *initial* primitive cell (shown in the left part in Fig. 14) with the initial periodicity $l_1^0 = b$ and $l_2^0 = a$. Once the bifurcation occurs, the initial periodicity may break, and the composite attains a new periodicity with an

enlarged primitive cell characterized by critical wavelength l_1^{cr} and l_2^{cr} (defined in the undeformed configuration). Recall that our calculations indicate that the onset of instabilities develops along the compressive direction, and the horizontal periodicity does not change upon buckling, namely, $l_1^{cr} \equiv l_1^0$; the vertical periodicity, however, does change with the onset of instability; therefore, here and thereafter, we only consider l_2^{cr} component of the critical wavelength and report l_2^{cr} as l^{cr} and l_2^0 as l^0 for simplification. For instability patterns, the following cases can occur. First, the enlarged primitive cell consists of an *integer* number of initial primitive cells. In this case, the critical wavelength is $l^{cr} = pl^0$ where p is an integer defining the number of initial primitive cells included in the enlarged primitive cell; the unit cell number can be obtained as $p = 1/k^{cr}$. For example, for the composite with $\xi = 0.45$ and $\eta = 1.6$, $k^{cr} = 0.25$, so that the enlarged primitive cell consists of $p = 4$ with an expected wavy pattern, including four inclusions in the period (see the right part in Fig. 14). A similar case with $k^{cr} = 0.5$ (for example, the cases with $\xi = 0.45$ and $\eta > 2.18$) is also illustrated in Fig. 14. In this case, a wavy pattern with two inclusions in the period is expected to develop upon the onset of instability. Similar to the above examples, the composites with their critical wavenumbers corresponding to $p = N$ (where $N = 1, 2, 3 \dots$) may develop a wavy pattern with critical wavelength $l^{cr} = pl^0$, including N incisions in its period. We note, however, that the critical wavenumbers can be continuous functions of η (see, for example, the curves for the composites with $\xi = 0.45$ in Fig. 13). Therefore, an infinite number of instability configurations with *non-integer* values of $1/k^{cr}$ are admissible through tuning the initial periodicity parameters. Fig. 14 schematically illustrates such a case of the composite with $\xi = 0.4$, $\eta = 1.546$, the corresponding critical wavenumber is $k^{cr} \approx 0.49$. However,

$1/k^{cr} \approx 2.04$ is indeed not an integer number, which we denote as $p' = 1/k^{cr}$ (to distinguish it from the cases with an integer number of unit cells). The corresponding enlarged primitive cell (consisting of an integer number of initial primitive cells) may be constructed, if there exists a large enough integer number n such that $p = np'$ is an integer. We note, however, that consideration may be sensitive to the accuracy of the results of the Bloch-Floquet analysis, namely, the accuracy of the critical wavenumber k^{cr} (and, hence, of p'). Thus, the composites (that are characterized by their critical wavenumber in the range $0 < k^{cr} < 0.5$) exhibit seemingly non-periodic instability patterns.

Next, we examine the seemingly non-periodic instability patterns via corresponding eigenmodes of the composites at the critical strains. Fig. 15 shows the eigenmodes of the composites at the critical strains with fixed spacing ratio $\xi = 0.4$ and various periodicity aspect ratios η =1.546, 1.544, 1.54, 1.5, 1.4, and 1.325 corresponding to eigenmodes (1) – (6). For each eigenmode, the colored map shows the relative lateral displacement (u_2) distribution. Note that, while the numerical analysis is performed on the single unit cell, the eigenmodes are reconstructed via the corresponding Floquet conditions to include a large number of unit cells in each domain (in particular, 50-unit cells are used).

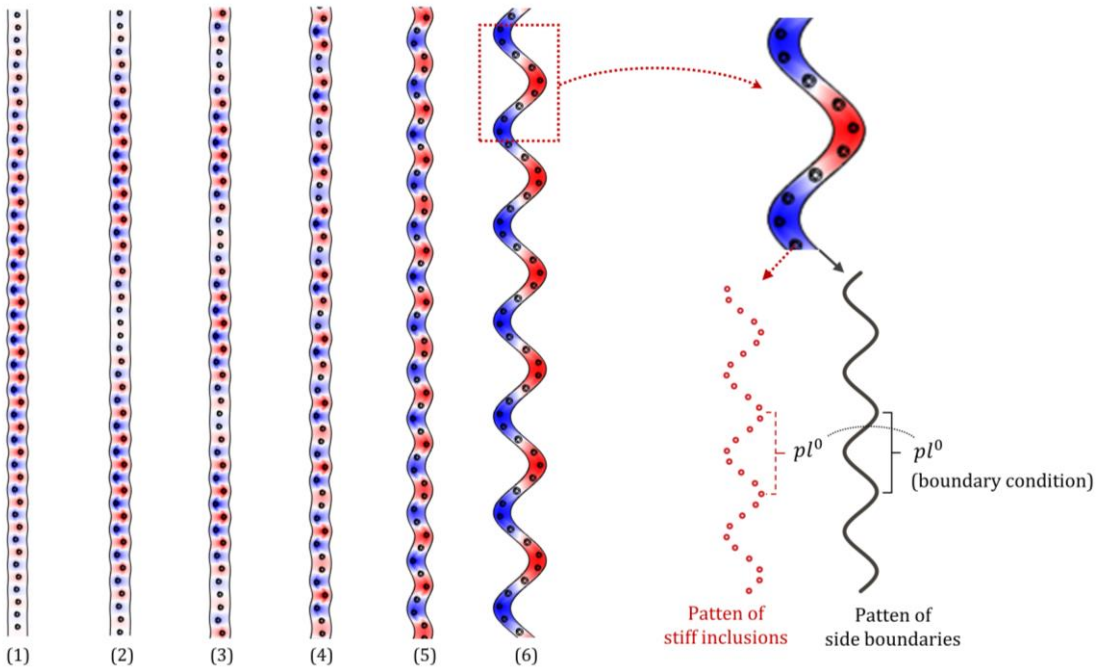

Fig. 15 Eigenmodes of the composites at the critical strains with spacing ratio $\xi = 0.4$ and various periodicity aspect ratios from 1.546 to 1.325.

For the composites characterized by smaller critical wavenumbers (see, for example, case (6) with $k^{cr} \approx 0.134$ corresponding to $p' \approx 7.463$ in Fig. 15), the eigenmodes exhibit wavy shapes with seemingly constant wavelengths. However, the wavelength of the overall wavy mode does not match the periodicity of the inclusion distribution. This mismatch – stemming from the fact that the smallest repeating unit must contain an integer number of inclusions – is illustrated in the schematics for case (6) in the right part of Fig. 15. The wavelength in case (6) is $7.463l^0$; thus, the seemingly full period does not contain an integer number of inclusions; therefore, the actual wavelength may be significantly higher, and its estimate depends on the accuracy of the critical wavenumber determined from the Bloch-Floquet analysis.

Consider the composites developing instabilities with the critical wavenumbers k^{cr} close to 0.5, such as, for example, cases (1)-(3) in Fig. 15. Their eigenmodes exhibit a beat-like phenomenon (Ferrari & Gatti, 1999). For example, case (1), characterized by $k^{cr} \approx 0.491$

($p \approx 2.04$) in Fig. 15, shows a wave packet with variable magnitudes; the wavelength of the envelope is approximated as $50l^0$. This eigenmode shows the features characterized by a superposition of two wavelets with very close wavelengths: $2.04l^0$ (defined by the critical wavenumber k^{cr}) and $2l^0$ (dictated by the closest integer number of inclusions within the updated primitive cells). This situation is reminiscent of the beat phenomenon with the superposition of two waves with slightly different wavenumbers, resulting in a wavy pattern with variable magnitudes (Ferrari & Gatti, 1999). The envelope of the maxima and minima in the superposed wave can be characterized by the estimated wavenumber $k^{env} \approx 0.5 - k^{cr}$. However, we observe that the composite included in one period of the envelope is still not a smallest repeating unit (see, for example, case (2), characterized by $k^{cr} \approx 0.479$ in Fig. 15, the distribution of the inclusions in one period of envelope curve does not exactly match that in the neighboring periods), and the strict smallest repeating unit should be constructed in a much higher scale.

4.1.1.3 Instability mode transitions via initial microstructure geometric parameters

Next, we summarize the results of critical wavenumbers as a surface in the geometrical parameter space of η and ξ in Fig. 16.

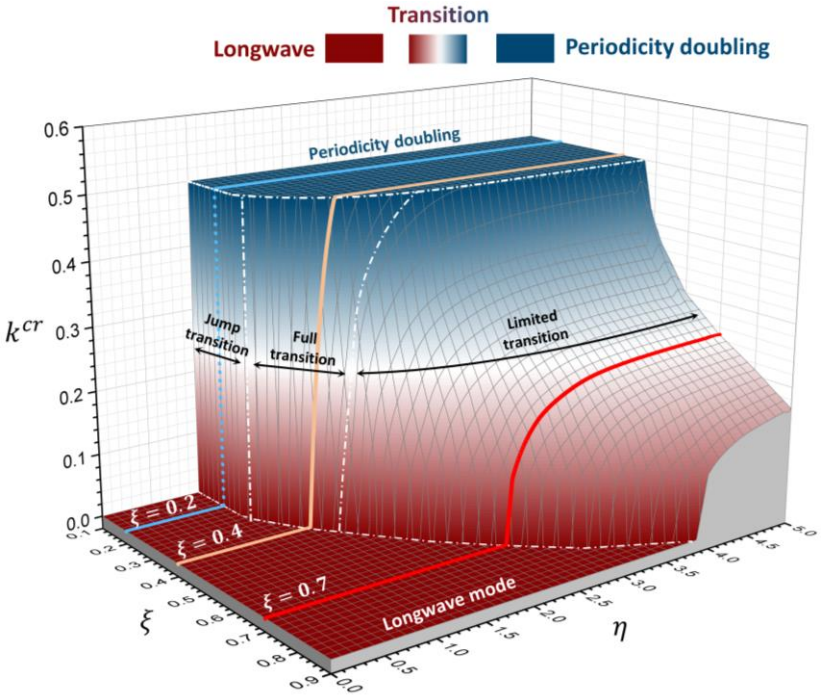

Fig. 16 Surface of critical wavenumber in the space of periodicity and spacing ratio.

In particular, the surface is divided into three sub-domains: (i) the pure red surface on the bottom – labeled as the "longwave" – denotes the geometries for which longwave instabilities develop (with $k^{cr} \to 0$); (ii) the pure blue surface – labeled as the "periodicity doubling" – on the top denotes the microscopic instabilities with constant critical wavenumber $k^{cr} = 0.5$ corresponding to the cases with the initial periodicity being (exactly) doubled upon bifurcation; (iii) the gradient surface – labeled with "transition" – in-between denotes the microscopic instabilities with various k^{cr} from 0 to 0.5, governed by the initial geometric parameters. Moreover, in the transition surface, we can further identify three different transition modes dictated by the periodicity aspect ratio η. First, for the composites with $\xi \lesssim 0.3$, only binary values of the critical wavenumber are possible, namely, either $k^{cr} \to 0$ or $k^{cr} = 0.5$, without any intermediate wavenumber (see, for example, the blue curve corresponding to $\xi = 0.2$ in Fig. 16; the wavenumber jumps from 0 to 0.5 at threshold value $\eta = 0.85$). Thus, we refer to this transition as the jump-transition mode. Second, for the composites with $0.3 \lesssim \xi \lesssim$

0.464, the transition develops gradually, with the wavenumbers changing from 0 to 0.5. This transition case is illustrated by the yellow curve corresponding to $\xi = 0.4$ in Fig. 16; the critical wavenumber increases continuously after the threshold value $\eta^{th} = 1.325$ and reaches the maximum level of 0.5 at $\eta = 1.548$. We denote this transition as the full-transition mode. Third, in the composites with $0.464 \precsim \xi \precsim 1$, the transition is somewhat similar to the previous case. The important difference, however, is that those composites are limited by their corresponding values of critical wavenumbers and do not attain $k^{cr} = 0.5$. For example, see the red curve corresponding to $\xi = 0.7$ in Fig. 16 here, the curve flattens (after the gradual increase range) and eventually reaches the plateau with $k^{cr} \to 0.248$. We refer to this transition as the limited-transition mode. As discussed above, the beat-like eigenmodes are observed for the composites developing instabilities with k^{cr} close but not equal to 0.5. Since in jump-transition mode we can only find $k^{cr} = 0$ or $k^{cr} = 0.5$, the beat-like eigenmodes are only expected to be found in full-transition and limited-transmission mode, such like $k^{cr} \approx 0.491$ corresponding to $\xi = 0.4$ and $\eta = 1.546$ in the full-transition mode and $k^{cr} \approx 0.454$ corresponding to $\xi = 0.47$ and $\eta = 3$ in the limited-transmission mode.

To further shed light on the mechanisms of these three transition modes, we analyze the variation of dispersion curves during each transition, see results for the jump-transition mode (including $\xi = 0.1$ and $\xi = 0.3$) in Fig. 17, the limited-transition mode (including $\xi = 0.7$ and $\xi = 0.9$) in Fig. 18 and full-transition mode (including $\xi = 0.4$ and $\xi = 0.45$) in Fig. 19. In each figure, the dotted and continuous curves correspond to the dispersion relation at the onset of macroscopic and microscopic instabilities, respectively. The trivial zero-point at $k_2 \neq 0$ indicates the critical wavenumber k_2^{cr}. First, see Fig. 17, we observe that the zero-point

never shifts along k_2 axis with an increase in η, and the transition develops via a drop of the normalized eigenfrequency f_n at $k_2 = 0.5$ gradually down to 0. This reveals why there is no intermediate wavenumber found in jump-transition mode. Second, see Fig. 18, we observe that the zero-point smoothly shifts from 0 along k_2 axis with an increase in η and is then limited to a finite value smaller than 0.5. Therefore, the limited-transition can give parts of intermediate wavenumbers under 0.5. Finally, see Fig. 19, the zero-point also shifts smoothly from 0 but eventually reaches 0.5. Therefore, we can find all intermediate wavenumbers from 0 to 0.5 in the full-transition mode. Moreover, the analysis of dispersion curves at critical points can not only help to understand the transition buckling modes but also provide opportunities for discussing the acoustic properties of this composite via instability.

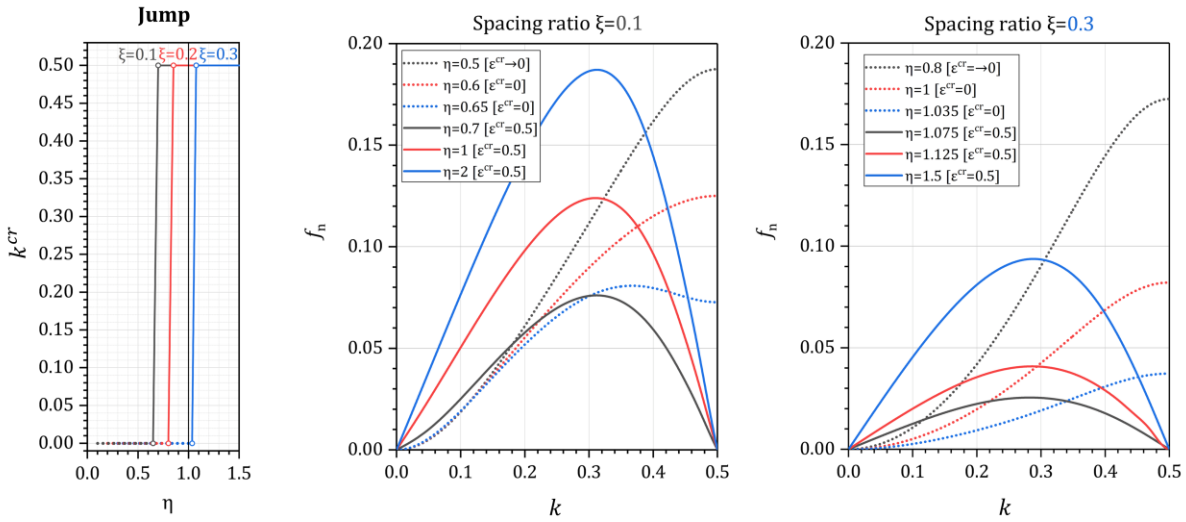

Fig. 17 Critical dispersion curves corresponding to the jump-transition mode.

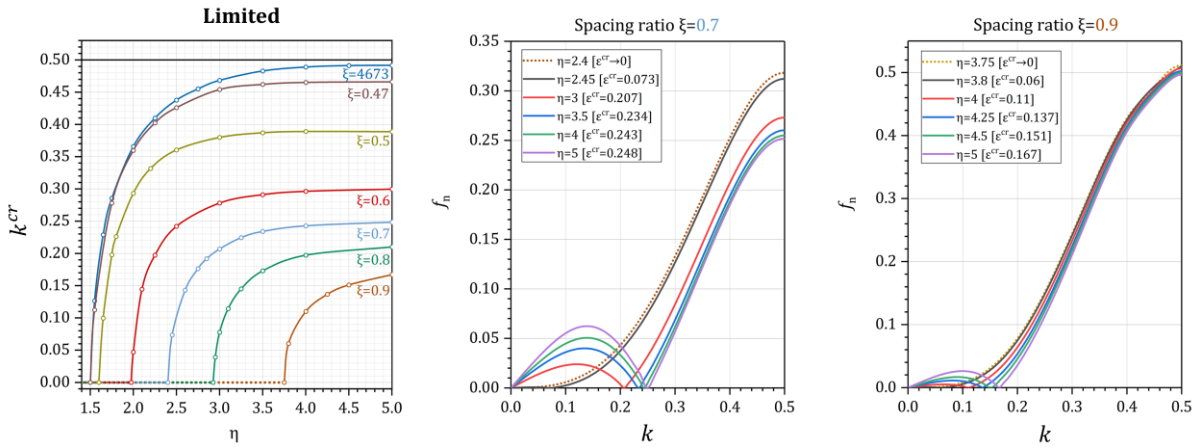

Fig. 18 Critical dispersion curves corresponding to the limited-transition mode

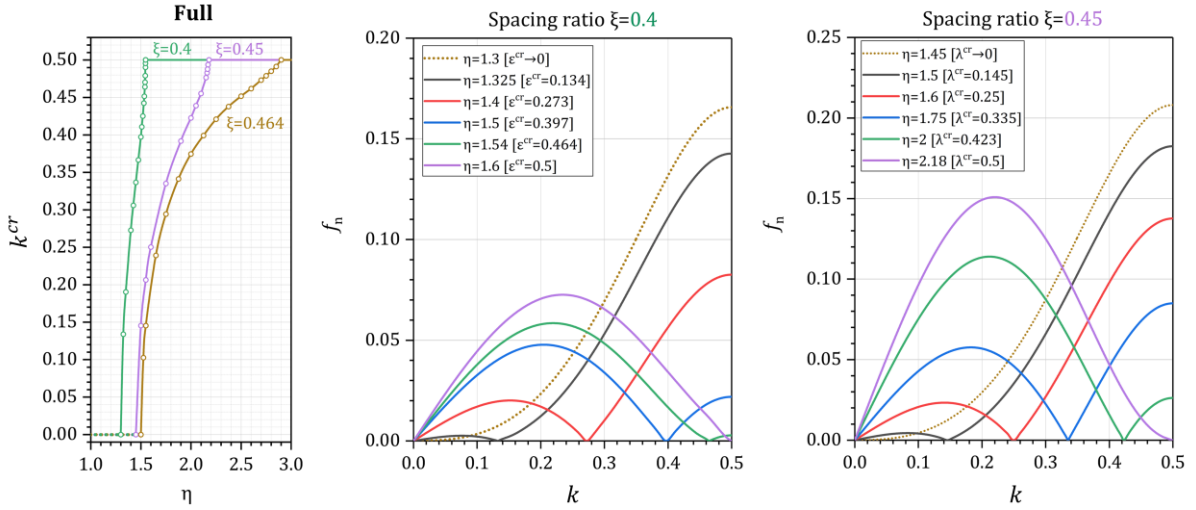

Fig. 19 Critical dispersion curves corresponding to the full-transition mode.

4.1.2 Energy landscapes

Fig. 20a shows a comparison of the critical strains identified from the energy landscapes (black curves) and that from the Bloch-Floquet analysis (colored curves), where the dependence of the critical strain on the periodicity aspect ratio η is plotted for composites with various fixed values of the spacing ratios $\xi = 0.3$, $\xi = 0.5$ and $\xi = 0.7$. We observe that, the onset of the longwave instability identified by the energy landscape analysis coincides with the one predicted by the Bloch-Floquet analysis (see, for example, the overlapped continuous and dotted curves in Fig. 20a corresponding to $\xi = 0.5$ within $0.5 < \eta < 1.65$). The predictions,

however, diverge from each other at the region where microscopic instability occurs first. The threshold values η^{th} corresponds to the transition from longwave to microscopic instability.

Fig. 20b illustrates the transition of the energy landscapes corresponding to the composite configurations (1) – (6) in Fig. 20a. The illustrated energy landscapes (1), (4), and (7) correspond to the lowest values of η, in particular, $\eta = 0.32$, $\eta = 0.55$ and $\eta = 0.75$, respectively; the energy landscapes (2), (5) and (8) correspond to $\eta = 0.4$, $\eta = 0.65$ and $\eta = 1.0$, respectively, at which the curves have their local minima. The energy landscapes (3), (6), and (9) illustrate the composite behavior in the region of increasing ε^{cr}; in particular, $\eta = 1$, $\eta = 1.5$ and $\eta = 1.5$, respectively. In the unstable region, the energy function becomes nonconvex, exhibiting a negative energy change rate (with a change in γ), $\partial\widetilde{W}/\partial\gamma < 0$. We note that the composites with a higher rate of energy decrease (at the same level of deformation) are characterized by lower critical strains. This is illustrated in Fig. 20b by the comparison of the composite configurations (4), (5), and (6) having the same spacing ratio $\xi = 0.5$ with all configurations subjected to the same compressive strain level, $\varepsilon = 0.4$. We note that the magnitude of the global energy decrease may also serve as an indicator of the composite stability similar to the local rate of energy change. For example, let us define the global decrease in energy as $[\widetilde{W}(\gamma = 0) - \widetilde{W}(\gamma = 0.3)]/\widetilde{W}(\gamma = 0)$ at the compressive strain level $\varepsilon = 0.4$. For all considered cases, a higher rate of energy decrease corresponds to a higher ratio of global decrease of energy under a small enough increase in γ. In composite configuration (5), we find a 0.135 decrease of energy with γ increased from 0 to 0.3, while those identified from configurations (4) and (5) are 0.108 and 0.0915, respectively. Composite configuration (5) exhibits the highest rate of energy decrease in the non-convex part of the energy landscape.

At the same time, composite configuration (5) has the critical strain $\varepsilon^{cr} = 0.265$, which is in the vicinity of the local minimum of the curve corresponding to $\xi = 0.5$ in Fig. 20a. The critical strains of the composite configuration (4) and (6) are $\varepsilon^{cr} = 0.272$ and $\varepsilon^{cr} = 0.296$, respectively. Similarly, we also compare other composite configurations with the same spacing ratio in Fig. 20b. For example, for the considered configurations (1), (2), (3) (having the same spacing ratio $\xi = 0.3$) the highest global decrease of energy is found for configuration (2), which is characterized by $\eta = 0.7$. The corresponding periodicity ratio of configuration (2) is found to be in the vicinity of the local minimum (at $\eta \approx 0.7$) of the critical strain curve (see the curve for $\xi = 0.3$ in Fig. 20a). Moreover, if we recall the two particulate system behaviors discussed in Sec. 4.1.1.1, configurations (3), (6), (9) also correspond to the soft particulate systems with laminate-like behaviors, configurations (1), (4), (7) correspond to the soft particulate system with additional horizontal interactions, and configurations (2), (5), (7) correspond to the vicinity of the transition point between these two particulate system behaviors.

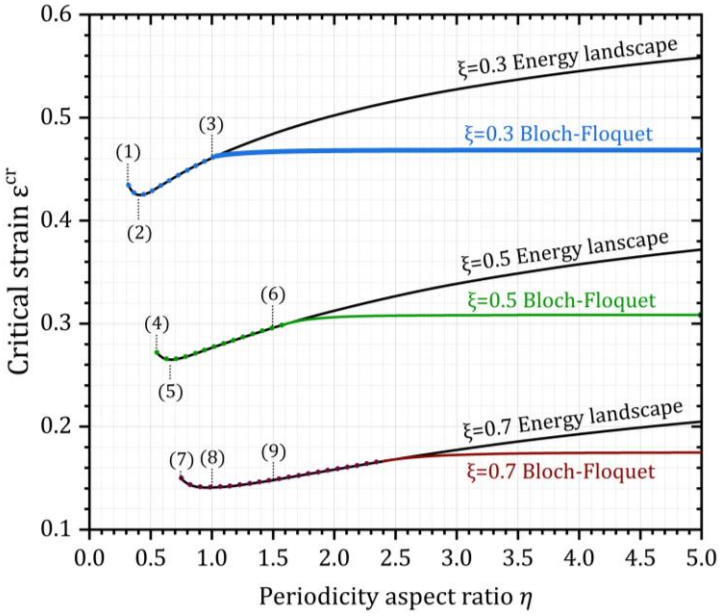

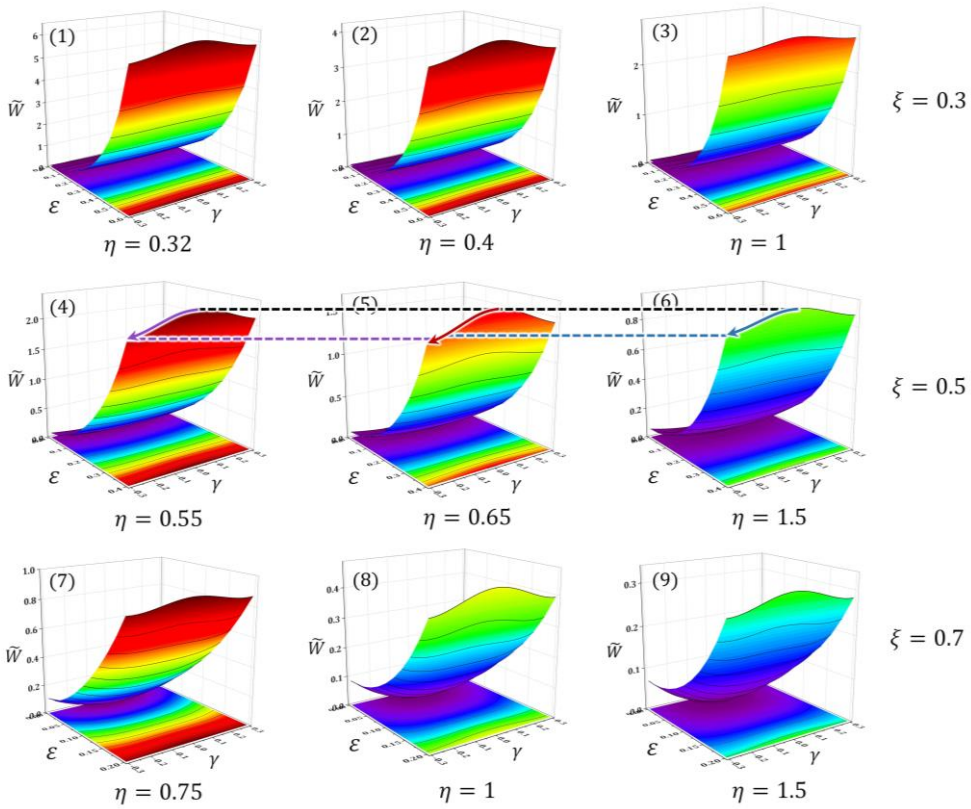

Fig. 20 (a) Comparison of critical strains derived from quasi-convexification and Bloch-Floquet analyses for the composites with $\xi = 0.3$, $\xi = 0.5$, $\xi = 0.7$ and $\xi < \eta \leq 5$;

(b) The energy landscapes of the composites with different geometric parameters ($\xi = 0.3$ with $\xi = 0.32$, $\xi = 0.4$, $\xi = 1$; $\xi = 0.5$ with $\xi = 0.55$, $\xi = 0.65$, $\xi = 1.5$; $\xi = 0.7$ with $\xi = 0.75$, $\xi = 1$, $\xi = 1.5$).

4.1.3 Post-buckling analysis

4.1.3.1 Result of post-buckling development

This section presents the post-buckling numerical calculation results and analysis. We start with an example of the particulate composite with the spacing ratio $\xi = 0.6$ and periodicity aspect ratio $\eta = 2.1$. Fig. 21a shows the corresponding initial RVE at $\varepsilon = 0$. For a more compact illustration, only 40-unit cells of the RVE are displayed here and thereafter. We observe that the composite material maintains a straight column of inclusions until a critical strain level of $\varepsilon^{cr} = 0.233$ is reached. At this point the inclusion column experiences a sudden collapse and transforms into a wavy chain of inclusions. This can be observed in the deformed

RVE shown in Fig. 21a, corresponding to $\varepsilon = 0.253$.

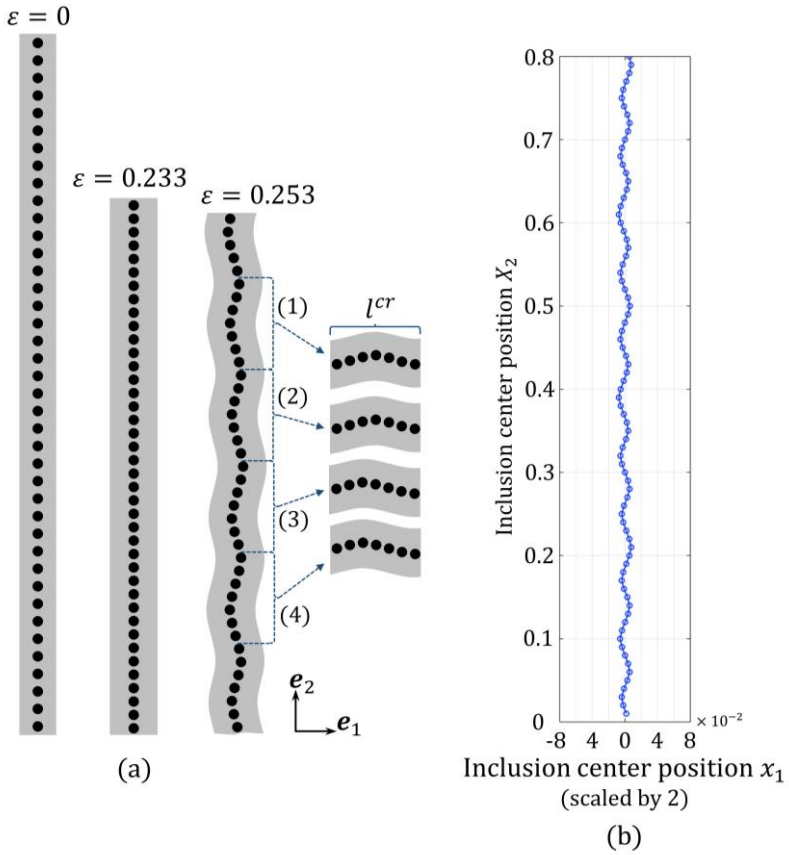

Fig. 21 (a) The deformation sequence under compressive strain level $\varepsilon = 0$, 0.233, and 0.253; initial geometric parameters are $\xi = 0.6$ and $\eta = 2.1$; (b) The position of inclusion centers in the deformed RVE.

The corresponding critical strain identified through the post-buckling DFT analysis is $\varepsilon^{cr} = 0.233$ (for the composite with $\xi = 0.6$ and $\eta = 2.1$); this value is in good agreement with the prediction of the Bloch-Floquet analysis, namely, $\varepsilon^{cr} = 0.2338$ (Chen et al., 2022). In experiments, Li et al. (2019a) also observed the formation of the "wavy chain" pattern of inclusions. This pattern transformation, induced by elastic instabilities, is a result of the breaking of the composite's initial periodicity, characterized by the initial wavelength $L^0 = b$, and the emergence of a new periodicity, characterized by the critical wavelength $L^{cr} = [k^{cr}]^{-1}b$, where k^{cr} is the *normalized* critical wavenumber and $l^{cr} = [k^{cr}]^{-1}$ is the corresponding *normalized* critical wavelength. For simplicity, in this study, we illustrate the

results in terms of the normalized critical values, such as k^{cr} and l^{cr}, and refer to them as the critical wavenumber and critical strain, respectively. It is worth noting that the critical wavelength L^{cr} also represents the height of the smallest repeating unit of the post-buckling configuration, referred to as the "enlarged primitive cell" (Chen et al., 2022; Bertoldi et al., 2008). Let us examine the instability-induced pattern in the composite in the post-buckling regime, in particular, at a strain level exceeding the critical value, namely, $\varepsilon = 0.253$. First, repeating blocks of seven inclusions may be observed; that would correspond to the critical wavelength of $l^{cr} \approx 7$. However, a further inspection of the distribution of inclusions shows that the position (phase) of the corresponding inclusion within different blocks is slightly shifted. For example, the fourth inclusion (from the left) in blocks (3) and (4) shift slightly downward in comparison to that in blocks (1) and (2). This deviation stems from the fact that the critical wavelength of the instability mode does not correspond to an integer number of initial primitive cells. In particular, according to our Bloch-Floquet analysis, the critical wavelength of this numerical case is predicted to be $l^{cr} \approx 6.89$. Therefore, in the post-buckling regime, the composite is unable to form a strictly periodic structure matching by critical wavelength, and is then forced to adapt a configuration with an integer wavelength $l^{cr} = 7$. This forced adaption, however, results in a somewhat frustrated distribution of inclusions and thus leads to the mismatch of inclusion centers in different inclusion blocks.

However, with the DFT analysis discussed in 3.3.2, we can not only correctly capture the onset of instability in post-buckling, but also correctly identify the critical wavenumber eliminating the interference of mismatch of inclusion centers. For example, we illustrate the results of the DFT analysis in Fig. 22, showing the dependence of the Fourier coefficient f on

component wavenumber k = 0.0125, 0.025, ... 0.4875 and 0.5, for fixed compressive strain levels (from 0.23 to 0.24). We observe that, below the critical strain level $\varepsilon^{cr} = 0.2338$, the composite maintains a straight column of inclusions, and correspondingly, we observe that all component wavenumbers are characterized by nearly zero Fourier coefficients. For example, in the green curve with circular markers corresponding to $\varepsilon = 0.233$ in Fig. 22, we observe a straight chain of inclusions in the composite; the corresponding DFT result is a horizontal line at zero values. However, after reaching the critical strain level ($\varepsilon^{cr} = 0.2338$), the inclusion column suddenly collapses and transforms into a wavy chain. Correspondingly, a peak of the Fourier coefficient emerges at $k = 0.145$. This is illustrated by the yellow curve with square markers corresponding to $\varepsilon = 0.235$ in Fig. 22. We observe a peak in the curve at $k = 0.145$ as the corresponding post-buckling pattern develops a wavy chain. Next, with an increase in the compressive strain level, the post-buckling deformation develops further, and the amplitude of the wavy-chain pattern increases. Correspondingly, we observe that the peak Fourier coefficient (at $k = 0.145$) becomes more prominent. This is also reflected in the increase in the amplitude of the wavy-chain pattern (see, for example, the DFT results corresponding to the compressive strain increased from $\varepsilon = 0.2339$ to $\varepsilon = 0.24$). The peak point in DFT results corresponds to a component harmonic curve that dominates the post-buckling wavy chain pattern, and the corresponding wavenumber of this peak point ($k^{cr} = 0.145$) is then identified as the critical wavenumber. This identification method may be applied for post-buckling analysis of particulate composites to identify the critical wavenumber, including the scenario with the frustrating distribution of inclusions (without identifying the enlarged primitive cell). We note that the precision of the DFT analysis depends on the number of

component wavenumbers scanned, which is also identical to the number of unit cells built in the RVE. Increasing the number of unit cells in the RVE can improve the accuracy of the wavenumber identification process. Our numerical results indicate that 80 unit cells are sufficient for obtaining the critical wavenumber accurately. The corresponding comparison of the DFT results obtained with different numbers of unit cells (from 20 to 200) in the RVE is given in Appendix A.

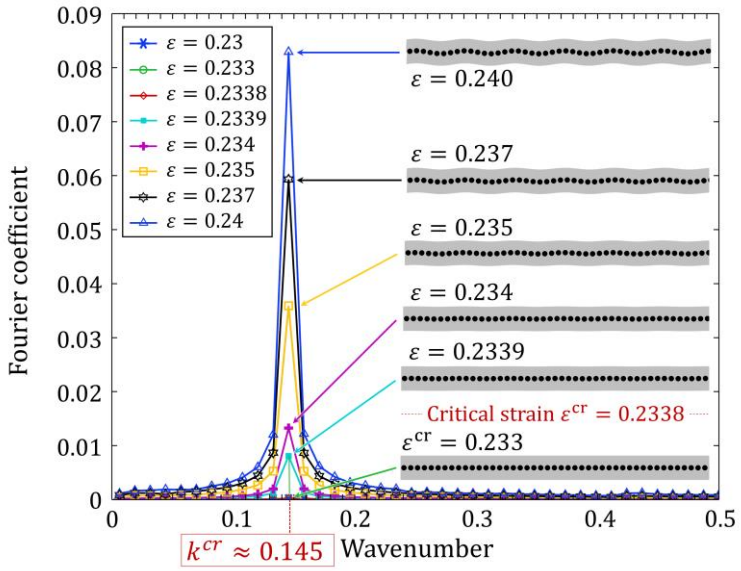

Fig. 22 The DFT analysis results of the post-buckling development for the composite with spacing ratio $\xi = 0.6$ and periodicity aspect ratio $\eta = 2.1$ at compressive strain $\varepsilon = 0.233$, $\varepsilon = 0.2339$, $\varepsilon = 0.234$, $\varepsilon = 0.235$, $\varepsilon = 0.237$, and $\varepsilon = 0.24$ with $N = 80$ number of unit cells built in the RVE.

4.1.3.2 Transition of post-buckling patterns with periodicity aspect ratios

We start by examining the post-buckling development with various initial geometrical parameters of the periodic microstructure. Specifically, the periodicity aspect and spacing ratios are altered by modifying the width of the unit cell and the diameter of the inclusion, respectively, while the height of the unit cell keeps constant. First, we examine the composites with a high spacing ratio $\xi = 0.8$ (the inclusions are placed relatively close in the direction of

compression) and various periodicity aspect ratios. In the upper part of Fig. 23, the red curve shows the dependence of the critical wavenumber k^{cr} on the periodicity aspect ratio η predicted by Bloch-Floquet analysis (from $\eta = 2.5$ to $\eta = 8.0$) for the fixed spacing ratio $\xi = 0.8$. The corresponding DFT analysis results of the post-buckling pattern are overlayed on the curve plot for the composites with periodicity aspect ratio $\eta =$ 2.7, 3.0, 3.25, 3.5, 4.0, 4.75, 6.0, and 7.5, where the vertical axis is the wavenumber, and the horizontal value is the corresponding Fourier coefficient. The lower part of Fig. 23 includes the corresponding post-buckling patterns, showing inclusion center positions at higher strain levels (after the onset of instability). The criterion for selecting these strain levels is based on the relative displacement of the inclusion centers; specifically, the post-buckling structures attain the same value of the so-called average amount of shear. Appendix A describes the details of how this criterion is defined and applied.

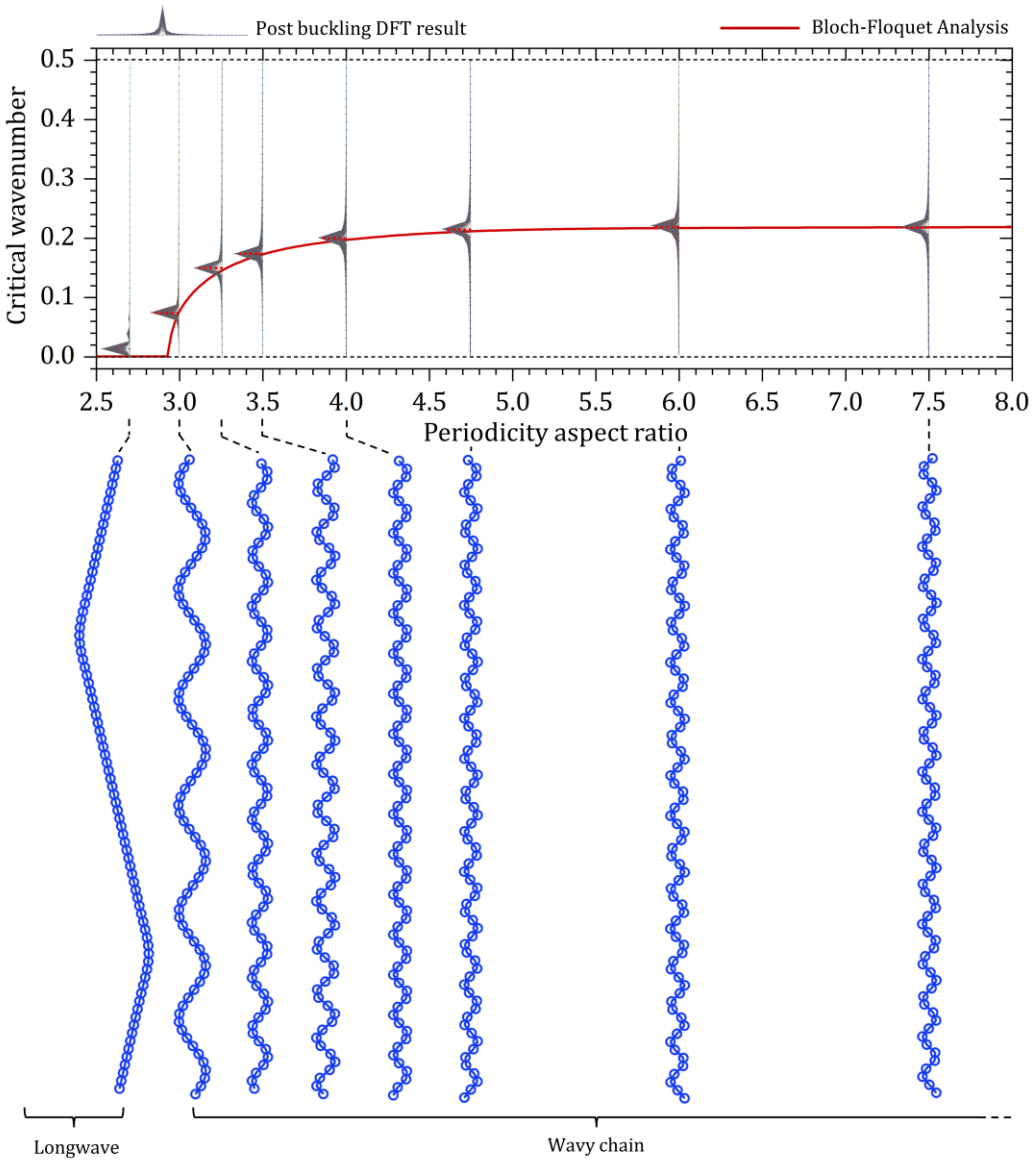

Fig. 23 Post-buckling patterns and the corresponding DFT results with fixed spacing ratio $\xi = 0.8$ and various periodicity aspect ratios (compared with the critical wavenumber predicted from the Bloch-Floquet analysis).

In Fig. 23, we included the Bloch-Floquet prediction of k^{cr} (red curve); the Bloch-Floquet curve starts with the longwave instability ($k^{cr} \to 0$) and transits to a microscopic instability ($k^{cr} > 0$) as the periodicity aspect ratio increases (corresponding to the inclusion columns placed farther away from each other) beyond a threshold value $\eta^{th} \approx 2.95$. For the corresponding post-buckling patterns, we observe a single period of the zigzag chain pattern for every longwave instability mode (see, for example, the pattern in the lower part of Fig. 23

corresponding to $\eta = 2.7$), with the DFT analysis identifying a single peak of Fourier coefficient at $k^{cr} = 0.0125$ (corresponding to the critical wavelength $l^{cr} = 80$, the height of the entire RVE). This is a result of the buckling wavelength being significantly larger than the characteristic size of the microstructure. Specifically, when a finite-sized RVE is used, only a single period of pattern with a critical wavelength corresponding to the height of the RVE will be observed in the cases of longwave instabilities; the peak of the DFT result will be found at the smallest wavenumber scanned, namely, the fundamental wavenumber $k = 1/N$. Similarly, if a larger number of unit cells in the RVE is used (for example, 200 cells), the critical wavelength will increase to $l^{cr} = 200$ and the corresponding critical wavenumber shifts down to $k = 1/200$.

For the microscopic instability modes ($k^{cr} > 0$), the corresponding critical wavelength is smaller than the height of RVE; hence, the wavy chain pattern emerges in the post-buckling regime. For example, for the patterns corresponding to $\eta = 3.0$, and $\eta = 3.25$ in the lower part of Fig. 23, the inclusion centers are observed in overall wavy distribution. The corresponding DFT results show a single peak emerging after the onset of instability, and the corresponding wavenumber values are close to those predicted via the Bloch-Floquet analysis. For instance, in the DFT result corresponding to $\eta = 3.0$ (in the upper part of Fig. 23), we observe a single peak of the Fourier coefficient at the wavenumber $k = 0.075$, and the corresponding Bloch-Floquet analysis prediction is $k^{cr} = 0.077$.

Next, we examine the post-buckling development in the composite with a relatively low spacing ratio $\xi = 0.3$ (the inclusions are placed relatively far away in the direction of compression) for various periodicity aspect ratios. In the upper part of Fig. 24, the Bloch-

Floquet curve shows the dependence of the critical wavenumber k^{cr} on the periodicity aspect ratio η for a fixed inclusion spacing ratio $\xi = 0.3$. The corresponding DFT results of the post-buckling pattern are also overlayed on the curve for the composite with periodicity aspect ratios $\eta =$ 0.8, 0.9, 1.0, 1.04, 1.06, 1.1, 1.2, and 1.3. The lower part of Fig. 24 shows the corresponding post-buckling patterns. For this composite configuration, the Bloch-Floquet predicts the critical wavenumber with only binary values, namely, either $k^{cr} \to 0$ or $k^{cr} = 0.5$. The wavenumber starts with $k^{cr} \to 0$ in the initial ranges of the periodicity aspect ratio, and it jumps from $k^{cr} \to 0$ to $k^{cr} \to 0.5$ after a threshold value $\eta^{th} \approx 1.05$, without any intermediate wavenumber during the transition. In the post-buckling analysis, the zigzag chain pattern for the longwave instability mode develops (see, for example, the pattern in the lower part of Fig. 24 corresponding to $\eta = 1.0$), with single peak of Fourier coefficient at $k^{cr} = 0.0125$ in the DFT analysis. For the microscopic instability mode with $k^{cr} = 0.5$, the initial periodicity doubles (*exactly*) upon buckling, and we observe a repeating two-inclusion period in the post-buckling pattern, namely, the periodicity-doubling pattern (see, for example, the patterns in the lower part of Fig. 24 corresponding to $\eta = 1.2$). The DFT analysis also shows a single peak of the Fourier coefficient at the wavenumber $k = 0.5$, corresponding to the critical wavelength $l^{cr} = 2$. In our numerical results, only the "zigzag chain" and the periodicity doubling patterns were found for composites with $\xi = 0.3$. This binary result holds true even in cases that are close to the threshold value of $\eta^{th} \approx 1.05$. For example, as shown in the lower part of Fig. 24, the post-buckling patterns for $\eta = 1.04$ and $\eta = 1.06$ exhibit zigzag chain and periodicity doubling patterns, correspondingly; no wavy chain patterns are observed.

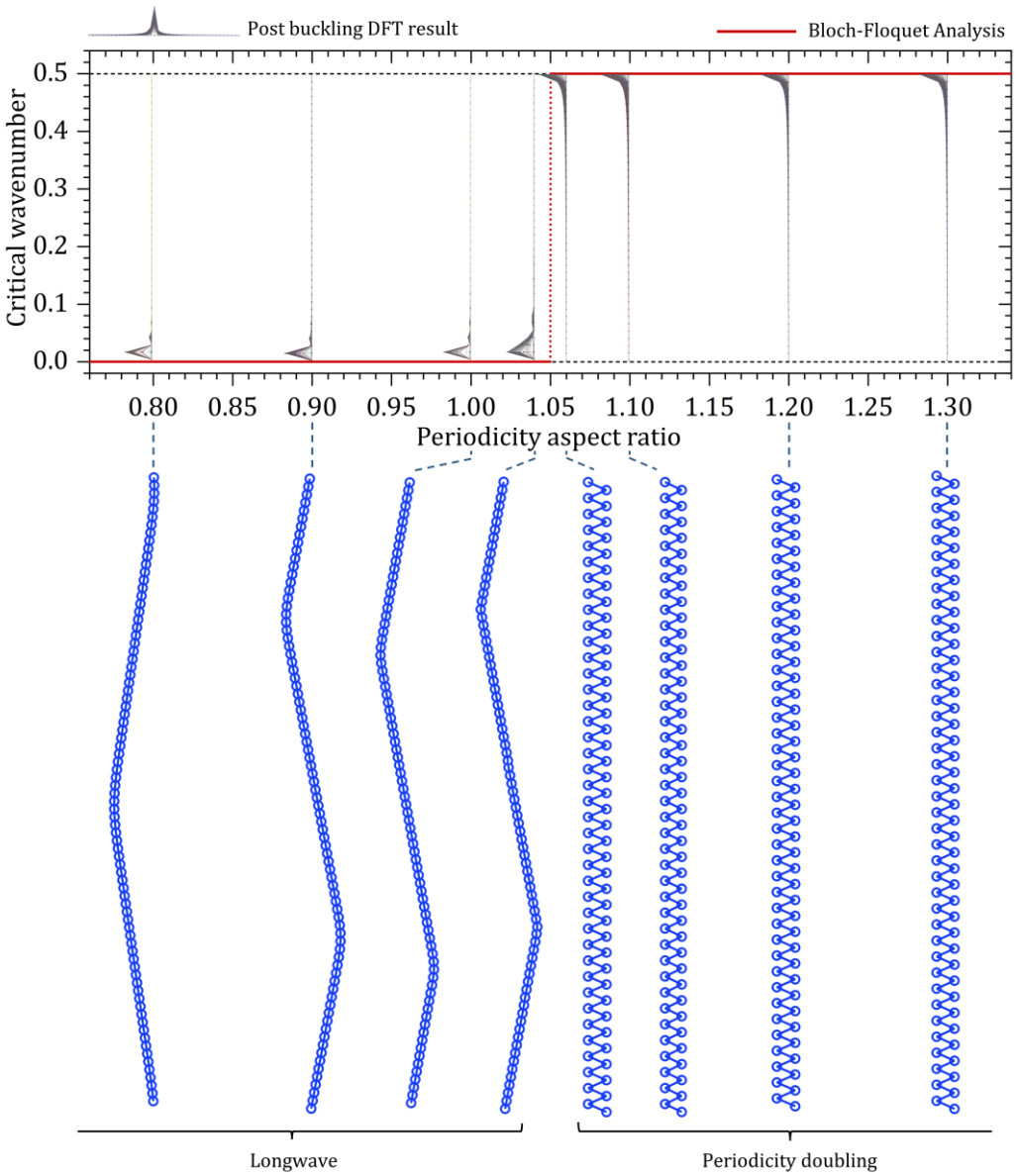

Fig. 24 Post-buckling patterns and the corresponding DFT results with fixed spacing ratio $\xi = 0.3$ and various periodicity aspect ratios (in comparison with the critical wavenumber predicted from Bloch-Floquet analysis).

Finally, we examine the post-buckling development of the composite with a moderate spacing ratio, namely, $\xi = 0.45$ and various periodicity aspect ratios. These composite configurations are characterized by a full evolution of critical wavenumber from the longwave $(k^{cr} \to 0)$ to the periodicity-doubling mode $(k^{cr} = 0.5)$ with an increase in the periodic aspect ratio (corresponding to an increasing distance between inclusion columns). This is

illustrated by the red curve in the upper part of Fig. 25, showing the dependence of (the Bloch-Floquet predicted) critical wavenumber k^{cr} on the periodicity aspect ratio η for fixed inclusion spacing ratio $\xi = 0.45$. The lower part of the figure shows the corresponding post-buckling patterns. In the lower part of Fig. 25, we observe an overall transition of the post-buckling patterns from a zigzag chain (for example, the pattern corresponding to $\eta < 1.46$) to the periodicity doubling pattern (for example, the pattern corresponding to $\eta > 2.18$). During the transition range (from $\eta = 1.46$ to $\eta = 2.18$), the post-buckling development starts with the wavy chain pattern corresponding to a relatively small critical wavenumber (see, for example, the cases corresponding to $k^{cr} = 1.5$ and $k^{cr} = 1.6$ in Fig. 25). However, as the critical wavenumber increases beyond $k^{cr} \approx 0.25$, we observe a significant change in the post-buckling shapes (see the patterns corresponding to $\eta = 1.7$ and $\eta = 1.8$ in Fig. 25). These patterns exhibit a superposition of two modes with different wavelengths. This is also identified in the corresponding DFT analysis results. In particular, we observe that the post-buckling pattern corresponding to $\eta = 1.7$ in Fig. 25 is not a typical wavy chain, but is composed of wavelets of small length scales (see the blue inclusion chains) enveloped in longer waves (see the red envelope curves). Correspondingly, we observe *two peaks* emerging in the DFT result after the onset of instability. The first peak locates at $k = 0.0625$ (representing the wavenumber of the envelope waves in large length scales), and the second peak locates at $k = 0.3125$ (representing the wavenumber of the wavelets in small length scales). Compared with the Bloch-Floquet prediction, $k^{cr} = 0.31$, the second peak in the post-buckling DFT analysis ($k = 0.3125$) represents the initial instability mode, and the first peak ($k = 0.0625$) represents an inclusion set in large length scales combined with the initial one for adaption of

the composite configuration as the initial instability mode does not correspond to an integer number of initial primitive cells.

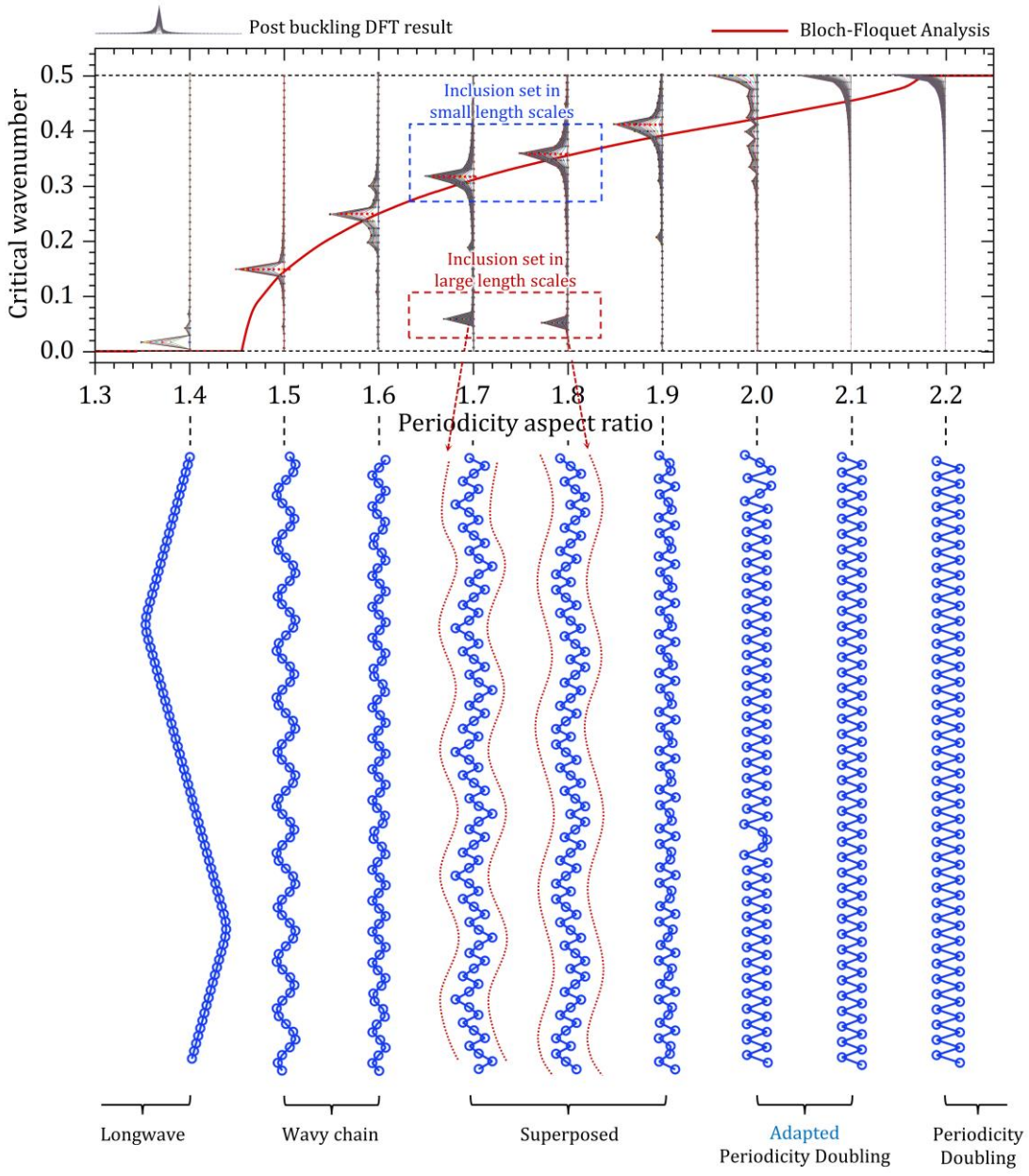

Fig. 25 Post-buckling patterns and the corresponding DFT results with fixed spacing ratio $\xi = 0.45$ and various periodicity aspect ratios (compared with the critical wavenumber predicted from Bloch-Floquet analysis).

A further increase in the periodicity aspect ratio (see the pattern corresponding to $\eta = 1.9$ in Fig. 25) leads to the formation of seemingly disordered and lacking periodicity

microstructures in the post-buckling regime. In the DFT results, a single peak is observed at $k = 0.4125$. However, this wavenumber is found to be larger than the prediction from the Bloch-Floquet analysis ($k^{cr} = 0.343$). This discrepancy results from the limited number of inclusions that need to be accommodated (between 2 and 3, given $l^{cr} \approx 2.91$) in an enlarged primitive cell. The frustrated composite cannot transform into a periodic structure within the instability-dictated length scale, and hence, it is forced to conform with a combination of inclusion sets in different length scales. This adaptation in post-buckling development leads to the critical wavenumber diverging from its Bloch-Floquet prediction. The frustrated patterns, however, become more regulated as the periodicity aspect ratio further increases (see the pattern corresponding to $\eta = 2.0$ and $\eta = 2.1$in Fig. 25). These composites start developing the periodicity doubling post-buckling structure (corresponding to a major peak at $k = 0.5$ in the DFT analysis) even though their critical wavenumber is not exactly 0.5. For example, the DFT analysis for the composite with $\eta = 2.0$ (see Fig. 25), shows the peak at $k = 0.5$, while the Bloch-Floquet prediction is $k^{cr} = 0.423$. Interestingly, for those composites attaining the periodicity-doubling mode, a single localized defect emerges (see Fig. 25 corresponding to $\eta = 2.0$). The DFT analysis also detects certain signals near the peak at $k = 0.5$. For instance, the DFT result corresponding to $\eta = 2.0$ in Fig. 25 detects multiple "minor signals" appears near the major peak at $k = 0.5$. These defects, however, disappear as the critical wavenumber is further increased. For example, the composite with $\eta = 2.1$ (corresponding to $k^{cr} = 0.455$ in the Bloch-Floquet analysis) exhibits a perfect periodicity doubling without developing the defects in the post-buckling regime. Finally, after the periodicity aspect ratio reaches $\eta = 2.18$, the post-buckling pattern does not change with a further increase in the

periodicity aspect ratio η, and the composite develops the exact periodicity-doubling in the post-buckling regime.

Next, we summarize the results of the post-buckling pattern developments as a map in the geometrical parameter space of η and ξ in Fig. 26. The map is divided into five sub-domains: (i) the red surface with diagonal strips – labeled as the "zigzag chain" – denotes the geometries for which longwave instabilities develop (with $k^{cr} \to 0$), where the post-buckling pattern is a single zigzag chain of inclusions; (ii) the blue surface with diagonal strips – labeled as the "periodicity doubling" – denotes the microscopic instabilities with constant critical wavenumber $k^{cr} = 0.5$, and the post-buckling pattern is the initial inclusion column being (exactly) doubled upon bifurcation; (iii) the solid pink surface – labeled with "Wavy chain" – denotes the microscopic instabilities with relatively low k^{cr} from 0 to the vicinity of 0.25, where the post-buckling pattern is a "wavy chain" of inclusions; (iv) the pure purple surface – labeled with "Superposed" – denotes the microscopic instabilities with relatively high k^{cr} from approximately 0.25 to 0.4, where the post-buckling pattern exhibits a superposition of wavelets (in small length scales) in between envelopes in large length scales; (v) the pure blue surface – labeled with "adapted periodicity doubling" – denotes the microscopic instabilities with k^{cr} close but not equal to 0.5; these composites adapt the "periodicity-doubling" post-buckling structure even though their critical wavenumber is not exactly 0.5.

While the post-buckling patterns demonstrate a good agreement with the Bloch-Floquet predictions (Chen et al., 2022) for small critical wavenumbers (typically, $k^{cr} \leq 0.5$), the difference appears when the critical wavenumber increases beyond $k^{cr} = 0.25$ (but not yet reached 0.5). The reason is that the composite configuration cannot transform into a periodic

structure dedicated by the critical instability wavelength; the pattern is then forced to adapt a structure in nearby length scales, or a combination of inclusion sets in different length scales in the post-buckling regime. The formation of those adapted patterns necessitates a large enough finite deformation after the onset of instability; thus, it was not able to be shown in the Bloch-Floquet analysis that considers linearized incremental deformations (superimposed upon the deformed state at the onset of instability). The post-buckling computations, together with the DFT analysis, capture those adapted post-buckling patterns with combined instability modes, enriching the understanding of the buckling behavior of particulate composites.

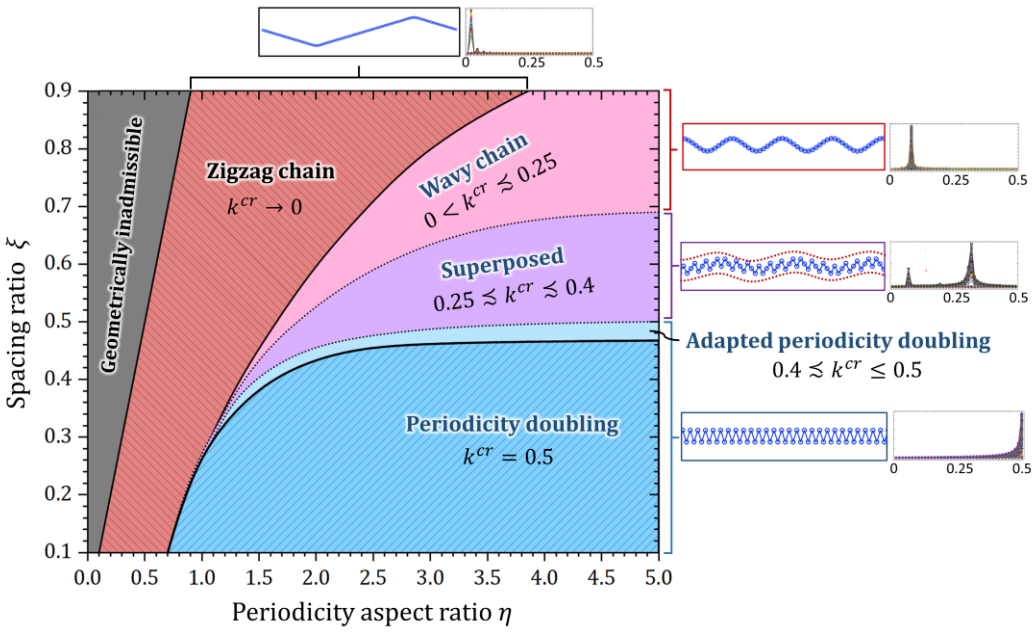

Fig. 26 Post-buckling pattern mapping in the geometrical parameter space.

4.1.3.3 Evolution of post-buckling patterns upon further deformations

Finally, we examine the evolution of the post-buckling development with deformation beyond the critical loading. Here, we are specifically interested in the situation when the initial buckling mode changes with the applied deformation. Recall that the composites that develop

relatively short-wave instability ($l^{cr} \lesssim 4$) are characterized by the adaptation of a combination of inclusion sets in different length scales in the post-buckling regime. Interestingly, in the post-buckling regime, we find the composite with a critical wavenumber lower than 0.25 (which initially forms a wavy-chain pattern) may also transform into a "superposed pattern" as the applied deformation forces the initial wavy buckling pattern to evolve. In Fig. 27, we illustrate this phenomenon via an example case for the composite with spacing ratio $\xi = 0.45$ and periodicity aspect ratio $\eta = 1.5$. The lower part of Fig. 27 shows the post-buckling pattern of the composite (illustrated by the inclusion center positions) right after the critical strain $\varepsilon^{cr} = 0.338$, and further after the buckling at $\varepsilon = 0.3386, \varepsilon = 0.34$ and $\varepsilon = 0.348$. The upper part of Fig. 27 shows the DFT analysis results corresponding to the above four deformation levels.

After the onset of instability at $\varepsilon^{cr} = 0.338$, the initial straight column of inclusions collapses and then transforms into a wavy chain as the compression continues to increase in a relatively small range. This is illustrated by the pattern in Fig. 27-2 showing the configuration at $\varepsilon = 0.3386$; the inclusions are located on a wavy curve with seemingly constraint amplitudes. The corresponding DFT results show a single peak at $k_I^{cr} = 0.15$. However, the corresponding wavelength $l_I^{cr} \approx 6.67$ is a non-integer value (see the DFT results corresponding to Fig. 27-2).

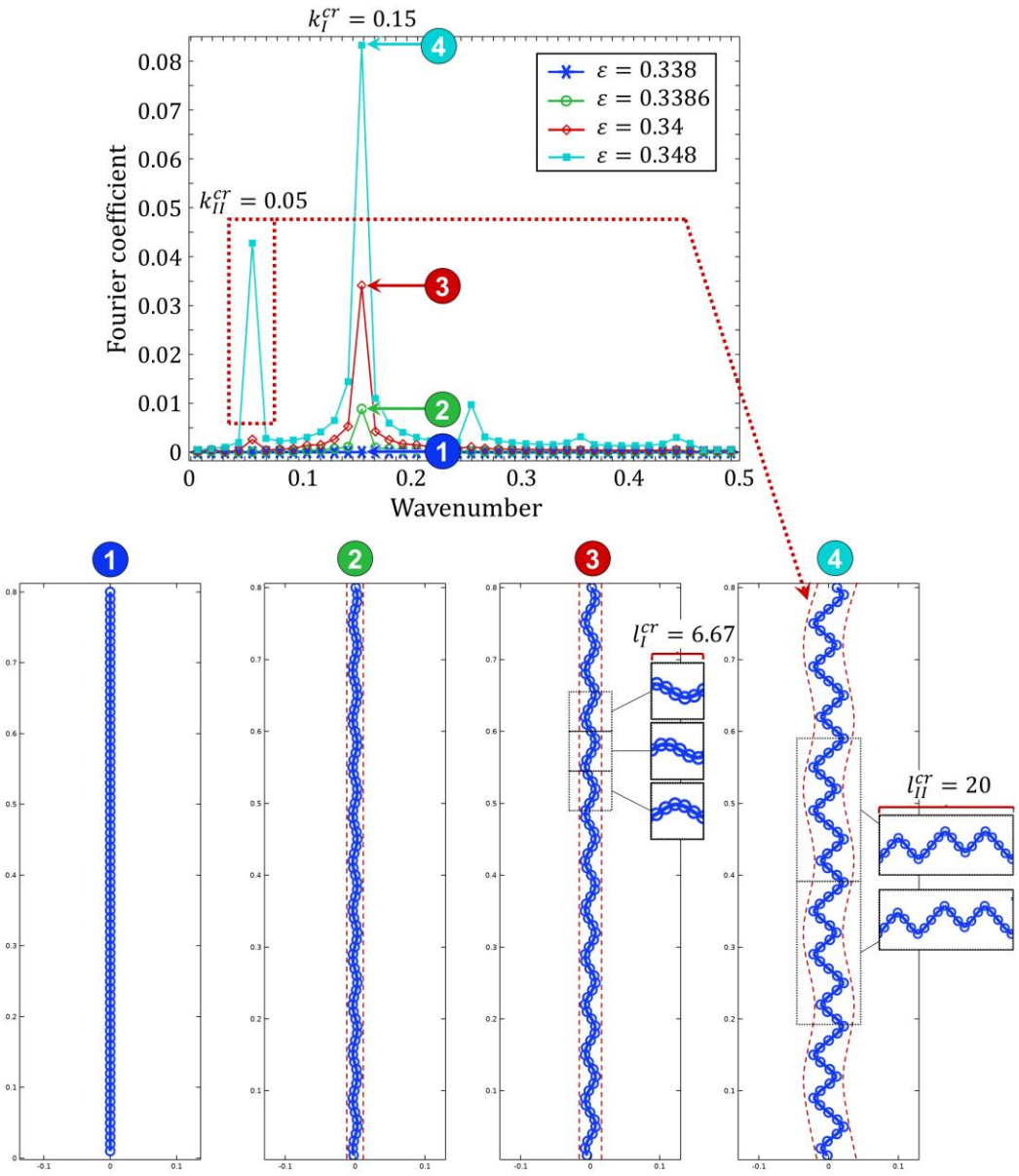

Fig. 27 Post-buckling patterns and the corresponding DFT results for the case with spacing ratio $\xi = 0.45$ and periodicity aspect ratio $\eta = 1.5$ under various compressive strain levels (1) $\varepsilon^{cr} = 0.338$, (2)$\varepsilon = 0.3386$, (3)$\varepsilon = 0.34$ and (4)$\varepsilon = 0.348$.

A further increase in the compressive strain leads to the transformation of the initial wavy chain pattern into a zigzag chain pattern. This emerging zigzag chain pattern appears to be enveloped between wavy curves in large length scales corresponding to the height of approximately 20 unit cells (see, for example, the area enveloped by the red dash curves in Fig. 27-4 corresponding to $\varepsilon = 0.34$). Interestingly, at the same time, we observe that there is a

second peak in the Fourier coefficient emerging at $k_{II}^{cr} = 0.338$, indicating the existence of the envelope in large length scales. This two-peak DFT result was also observed in the post-buckling pattern shown in Fig. 25, corresponding to high wavenumbers ($k^{cr} > 0.25$). However, the case shown in Fig. 27 has a lower wavenumber $k_I^{cr} = 0.15$, and the first and second peak of the DFT results do not emerge simultaneously upon the onset of instability (the secondary peak emerges only after certain additional compression is applied, while the first peak appears right after buckling). This is due to the fact that the initial wavy chain pattern (corresponding to the "first" wavenumber $k_I^{cr} = 0.15$, and the "first" critical wavelength $l_I^{cr} \approx 6.67$) does not have an integer number of inclusions in a wave period. For example, the inclusion blocks shown on the left of Fig. 25-3 exhibit seemingly incomplete wave periods with a non-integer number of inclusions between 5 and 6. Under relatively small increases in deformation after buckling, the inclusion chain can still maintain the overall wavy shape. However, as the post-buckling deformations become even higher, the composite can no longer maintain a non-integer number of inclusions in a wave period. It finally accommodates a combination of inclusion sets in different length scales. For example, the inclusion blocks shown on the right side of Fig. 27-4 have exactly 20 inclusions corresponding to the secondary critical wavelength $l_{II}^{cr} \approx 20$; and in each inclusion block we observe three small wavelets, the average length is $20/3 \approx 6.67$, which corresponds to the first critical wavelength $l_I^{cr} \approx 6.67$. The results discussed above indicate that the post-buckling pattern continues to evolve with further deformation after its initial formation. Remarkably, the evolution may be rather complex beyond a simple amplification of the initial pattern. Specifically, the post-buckling pattern can evolve from a single wavy chain into distinct configurations characterized by a combination of

inclusion sets with different length scales.

4.1.4 Secondary buckling development in post-buckling regime

4.1.4.1 Analysis of post-buckling results for secondary buckling

In this section, we present the results of an example case of the post-buckling analysis. We illustrate the result with an example of the particulate composite with the spacing ratio $\xi = 0.45$ and periodicity aspect ratio $\eta = 6$. The corresponding initial RVE at $\varepsilon = 0$ is shown in Fig. 28. Note that, only 80 unit cells of the RVE are displayed for a more compact illustration here and thereafter. We observe that the composite maintains a straight column of inclusions until it reaches the onset of the first stage buckling at the corresponding critical strain level of $\varepsilon_I^{cr} = 0.233$. At this point, the inclusion column experiences a sudden local collapse, with adjacent inclusions moving to the opposite side of each other. For example, as shown in Fig. 28, corresponding to $\varepsilon = 0.368$, the odd-numbered inclusions from the bottom move horizontally to the right side, while the even-numbered inclusions move to the left. As the compression continues to increase despite the buckling already being triggered, the composite structure quickly forms a seemingly "two straight columns of inclusions" near the middle line of the RVE (see, for example, in Fig. 28, corresponding to $\varepsilon = 0.555$). This post-buckling buckling pattern, however, provides highly ordered and compact arrangement of inclusions with strong interconnections. Therefore, we observe that the buckled composite, however, recovers its stability by forming an effective "particle-reinforced layer" in the center area of the composite, which includes the two columns of inclusions (see, for example, the composite structure corresponding to $\varepsilon_{II}^{cr} = 0.555$ in Fig. 28). Given this analogy, we observed that, this

reinforced layer experiences a wrinkling after a critical strain level of $\varepsilon_{II}^{cr} = 0.555$ is reached. At this point, the two "straight columns" of inclusions transform into two "wavy chain" of inclusions. This pattern transformation can be observed in the deformed RVE shown in Fig. 28, corresponding to $\varepsilon = 0.565$. We call This distinctive buckling phenomenon the "secondary buckling" that occurs in the post-buckling regime of the first(initial) buckling.

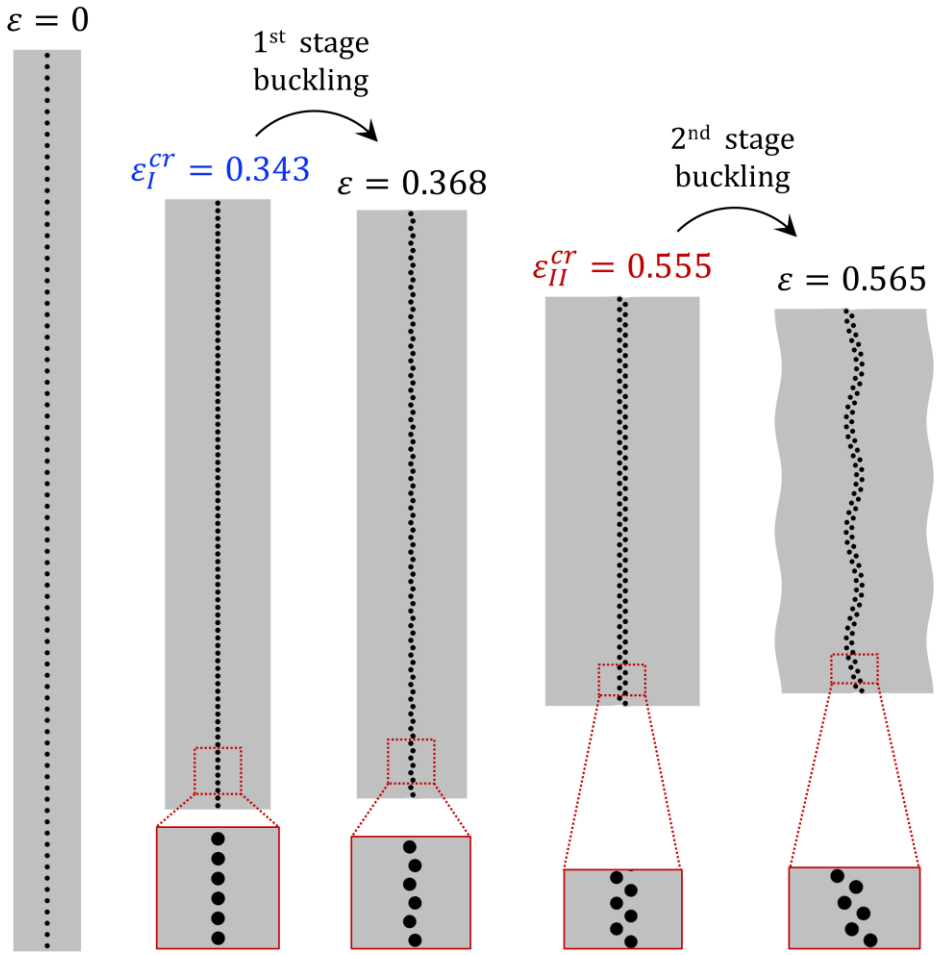

Fig. 28 The deformation sequence under compressive strain level $\varepsilon = 0$, $\varepsilon = 0.343$, $\varepsilon = 0.368$, $\varepsilon = 0.555$, and $\varepsilon = 0.565$; initial geometric parameters are $\xi = 0.45$ and $\eta = 6$. Only 80 unit cells of the RVE are displayed for a more compact illustration.

Next, in Fig. 29, we illustrate the results of the DFT analysis for the composite with $\xi = 0.45$ and $\eta = 6$, showing the dependence of the Fourier coefficient f on component

wavenumbers, for fixed compressive strain levels from 0 to 0.557. Until the critical strain level $\varepsilon^{cr} = 0.343,$ the composite maintains a straight column of inclusions, and correspondingly, all component wavenumbers are characterized by nearly zero Fourier coefficients. However, after reaching the first critical strain level ($\varepsilon_I^{cr} = 0.343$), the inclusion column suddenly collapses into a periodicity doubling pattern. Correspondingly, a peak Fourier coefficient emerges at $k = 0.5$, representing the doubled periodicity and the critical wavenumber of the first buckling $k_I^{cr} = 0.5$. This is illustrated by the green curve with triangular markers corresponding to $\varepsilon = 0.368$ in Fig. 29.

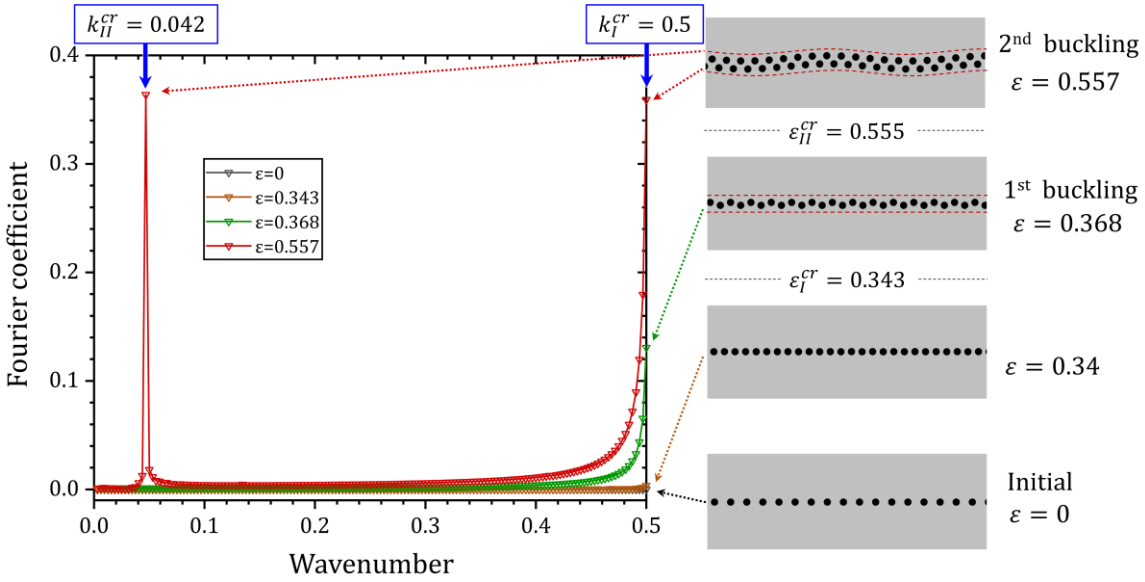

Fig. 29 The DFT analysis results of the post-buckling development for the composite with spacing ratio $\xi = 0.45$ and periodicity aspect ratio $\eta = 6$ at compressive strain $\varepsilon = 0$, $\varepsilon = 0.34$, $\varepsilon = 0.368$, and $\varepsilon = 0.557$ with $N = 320$ number of unit cells built in the RVE (the RVE view is zoomed so not all inclusion are displayed).

Next, with an increase in the compressive strain level, the post-buckling pattern evolves, and the thickness of the "particle-reinforced layer" increases. After the critical strain of the secondary buckling $\varepsilon_{II}^{cr} = 0.55$, we observe a second peak emerging in the Fourier spectrum at $k_{II}^{cr} = 0.042$, representing a wavy buckling mode of the "reinforced layer." Therefore,

$k_{II}^{cr} = 0.042$ is identified as the critical wavenumber of the secondary buckling. Correspondingly, the critical strain of the secondary buckling ε_{II}^{cr} is identified at the lowest strain level, where a peak in the Fourier spectrum is detected to exceed the threshold coefficient 10^{-2} at a wavenumber other than $k_I^{cr} = 0.5$.

4.1.4.2 Dependence of critical strain on geometric parameters

We start by examining the *secondary* buckling development via the dependence of critical strains on the composite's initial geometrical parameters. Fig. 30 shows the dependence of the critical strain on the periodicity aspect ratio η for various fixed values of the inclusion spacing ratios $\xi = 0.3, 0.35, 0.4$ and 0.45, where the dotted and continuous curves correspond to longwave ($k_{II}^{cr} \to 0$) and microscopic ($k_{II}^{cr} > 0$) buckling derived from the Bloch Floquet analysis, respectively; the triangular scatters correspond to the results from the post-buckling analysis. It should be emphasized that *secondary* buckling has only been found in composites with "periodicity doubling" buckling mode in their *first* buckling stage. It has been shown in recent research (Chen et al., 2022, 2023) that those "periodicity doubling" patterns form in composites with small enough spacing ratios ($\xi \lesssim 0.45$) and large enough periodicity aspect ratios (for composites with $\xi = 0.45$, the "periodicity doubling" pattern is found when $\eta \gtrsim 2$). Moreover, the admissible geometries are restricted by $d < b$ and $d < a$, thus, limiting the parameter space as $\eta > \xi$.

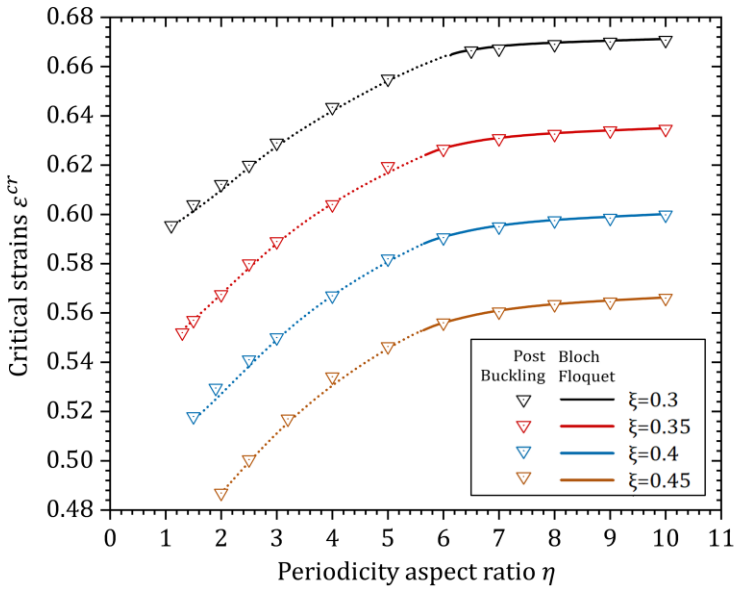

Fig. 30 The dependence of *secondary* buckling critical strain on periodicity aspect ratio with various spacing ratios. The dotted and continuous curves correspond to longwave and microscopic buckling results (from the post-buckling analysis), respectively; the triangular scatters correspond to results from the Bloch-Floquet analysis.

We observe that the secondary buckling critical strain derived from post-buckling analysis agrees well with the predictions of the Bloch-Floquet analysis. The composites with higher spacing ratios experience secondary buckling at lower compressive strains. For example, as shown in Fig. 30, in the composites with the same periodicity aspect ratio $\eta = 7$, with an increase in the spacing ratio from $\xi = 0.3$ to $\xi = 0.45$, the onset of *secondary* buckling shifts from $\varepsilon_{II}^{cr} = 0.6685$ to 0.5611. This stems from the fact that the large-sized inclusions (that are large in the composites with larger spacing ratios) provide a high volume fraction of the stiff inclusions in the effective "particle-reinforced layer," thus increasing the effective stiffness contrast between the soft matrix and the particle-reinforced layer, eventually leading to an earlier onset of the secondary buckling. We also observed that the critical strain ε_{II}^{cr} increases monotonically with an increase in η for all considered spacing ratios. Moreover, we observe that the secondary buckling develops in the longwave modes ($k_{II}^{cr} \to 0$) in the composites with

small enough periodicity aspect ratios. However, the buckling mode switches from longwave to microscopic one in composites with a periodicity aspect ratio large than a threshold value η^{th}, dictated by the initial spacing ratio value ξ (specifically, larger spacing ratios lead to an earlier transition from micro- to longwave secondary buckling). For example, for the composite with $\xi = 0.35$ (the red curve in Fig. 30), the buckling develops in a longwave mode with small enough periodicity aspect ratios such as $\eta = 3$. With an increase in η, the critical strain increases monotonically. After the threshold value $\eta^{th} \approx 5.68$ is reached, a switch from the longwave to microscopic buckling mode occurs, followed by the continuous increase of the critical strain with an increase in the periodicity aspect ratio.

4.1.4.3 Dependence of critical wavenumber on geometric parameters

Let us examine the dependence of the secondary buckling critical wavenumber on the periodicity aspect ratio η. In Fig. 31, we plot the prediction of k_{II}^{cr} from Bloch-Floquet analysis (red dotted and continuous curves, corresponding to longwave and microscopic buckling, respectively) and the post-buckling results (triangular scatters). We observe that the Bloch-Floquet and the post-buckling predictions agree well with each other. Specifically, for microscopic instabilities, they predict critical wavenumbers at a finite value $k_{II}^{cr} > 0$; for longwave instabilities, they predict critical wavenumbers corresponding to their longwave limit $k_{II}^{cr} \to 0$ and $k_{II}^{cr} = 1/320$, respectively.

Next, when the periodicity aspect ratio increases beyond a threshold value η^{th} (corresponding to the initial inclusion columns placed farther away enough from each other), we find a transition from longwave instability to microscopic instability (corresponding to

$k_{II}^{cr} > 0$ in Bloch-Floquet analysis and $k_{II}^{cr} > 1/320$ in post-buckling analysis) beyond a threshold value η^{th}. We also observe that the composites with larger spacing ratios experience an earlier transition from longwave to microscopic instabilities, but is followed by a relatively lower increasing rate of the critical wavenumber, but is followed by a relatively lower increasing rate of the critical wavenumber. For example, comparing the composites with $\xi = 0.3$ and $\xi = 0.4$, the switch from longwave to microscopic mode occurs at $\eta^{th} \approx 6.18$ and $\eta^{th} \approx 5.65$, respectively. After those switches, the wavenumber starts to increase. However, at a higher critical wavenumber, such as $\eta = 10$, the composite with $\xi = 0.3$ reaches a lower critical wavenumber $k_{II}^{cr} = 0.074$ while the composite with $\xi = 0.4$ reaches a higher critical wavenumber $k_{II}^{cr} = 0.069$. However, for composites with a larger spacing ratio, such as $\xi = 0.45$, the corresponding threshold value shifts down to $\eta^{th} \approx 5.65$; the critical wavenumber number reduces to $k_{II}^{cr} = 0.137$ at $\eta = 10$.

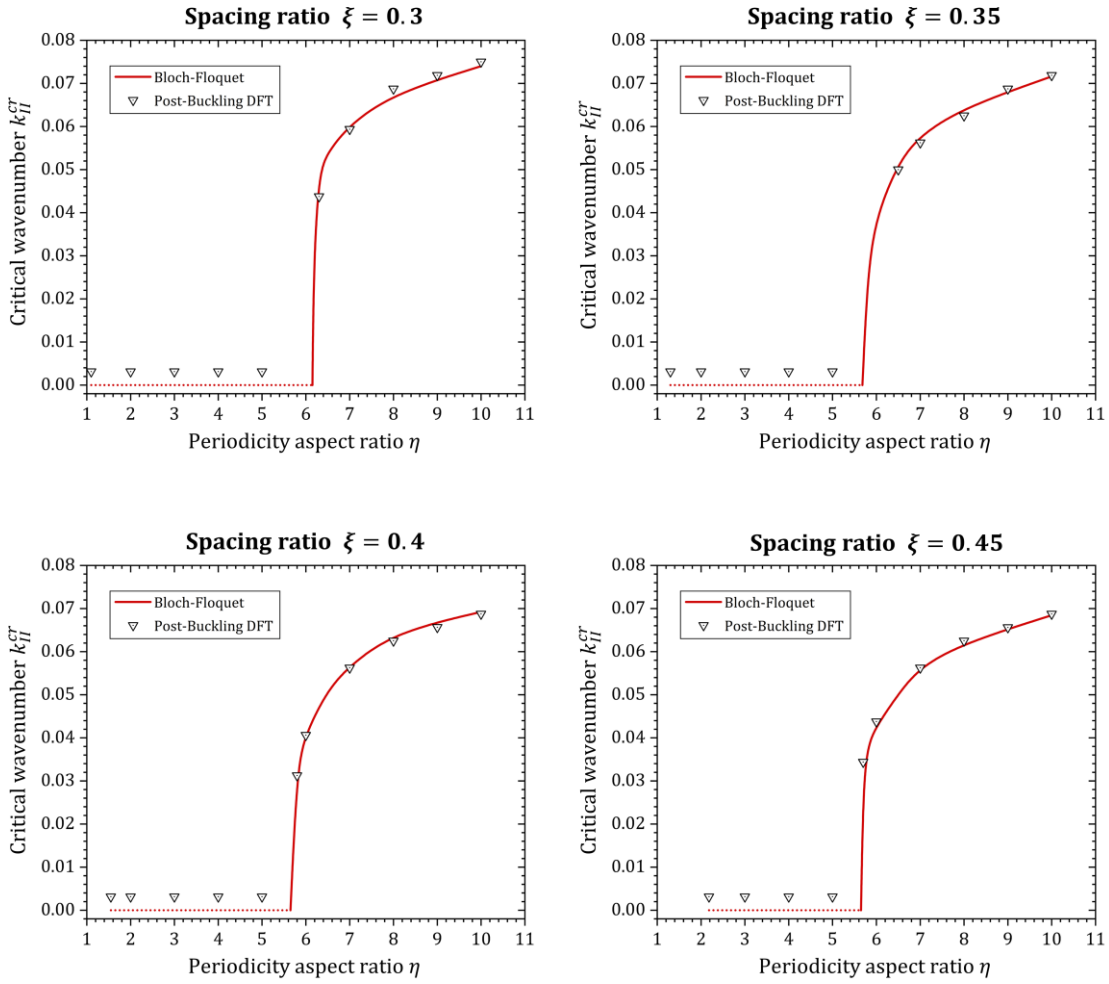

Fig. 31 The dependence of critical wavenumber on the periodicity aspect ratio with various spacing ratios. Triangular scatters and continuous curves correspond to results from post-buckling analysis and Bloch Floquet analysis, respectively.

Finally, we summarize the results of the first and secondary buckling patterns as a map in the geometrical parameter space of the periodicity aspect ratio η and the spacing ratio ξ, as shown in Fig. 32. In the map, the *first stage* buckling patterns are divided into *six* sub-domains. Among them, four grey sub-domains represent composite geometries that will only develop the first stage buckling (Chen et al., 2023): (i) the domain labeled as the "zigzag chain" corresponds to the critical wavenumber of the first stage buckling $k_I^{cr} \to 0$, where buckling pattern is a single zigzag chain of inclusions; (ii) the domain labeled with "Wavy chain"

corresponds to relatively low k_I^{cr} from 0 to the vicinity of 0.25, where the buckling pattern is a "wavy chain" of inclusions; (iv) the domain labeled with "Superposed" corresponds to a relatively high k_I^{cr} from approximately 0.25 to 0.4, where the buckling pattern exhibits a superposition of wavelets (in small length scales) in between envelopes in large length scales. The highlighted two sub-domains represent composite geometries that can develop the *secondary* buckling, based on their formation of a "periodicity doubling" or "adapted periodicity doubling" pattern in the first stage buckling. The bright blue domain – labeled with "longwave" – represents the geometries that will develop longwave secondary buckling, corresponding to $k_{II}^{cr} \to 0$; the dark blue domain – labeled as "microscopic," represents the composite geometries that will develop secondary buckling in the microscopic modes, corresponding to $k_{II}^{cr} > 0$. Our results have shown that *secondary* buckling occurs in composites with small aspect ratios and large periodicity aspect ratios, in which longwave secondary buckling occurs with relatively small periodicity aspect ratios, and microscopic secondary buckling occurs with relatively large spacing ratios.

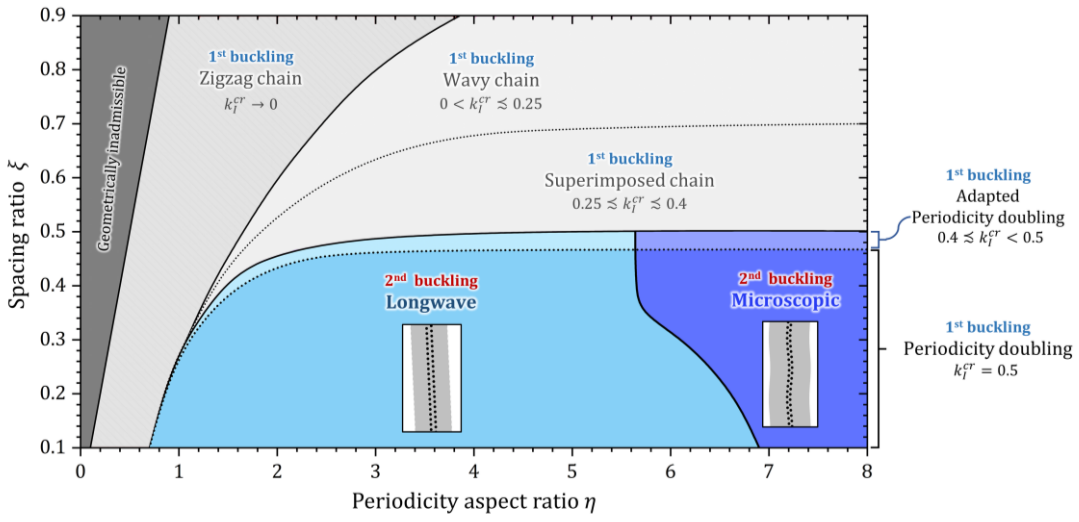

Fig. 32 The first and secondary buckling pattern mapping in the geometrical parameter space. The highlighted areas (bright and dark blue) represent the secondary buckling.

4.2 Composite(2D) with two different-sized inclusions

4.2.1 Bloch-Floquet prediction

4.2.1.1 Dependence of critical strain on geometric parameters

In this section, we examine the influence of the instability characteristics, such as critical strain and wavenumber, on the diameter contrast ratio of the particulate composite with two different-sized inclusions. The blue curves in Fig. 33 show the dependence of the critical strain on the diameter contrast ratio k_d for various fixed values of the inclusion spacing ratios $\xi = 0.4$, $\xi = 0.6$ and $\xi = 0.8$. The black dash line shows the corresponding critical strain of the single-sized inclusion composite.

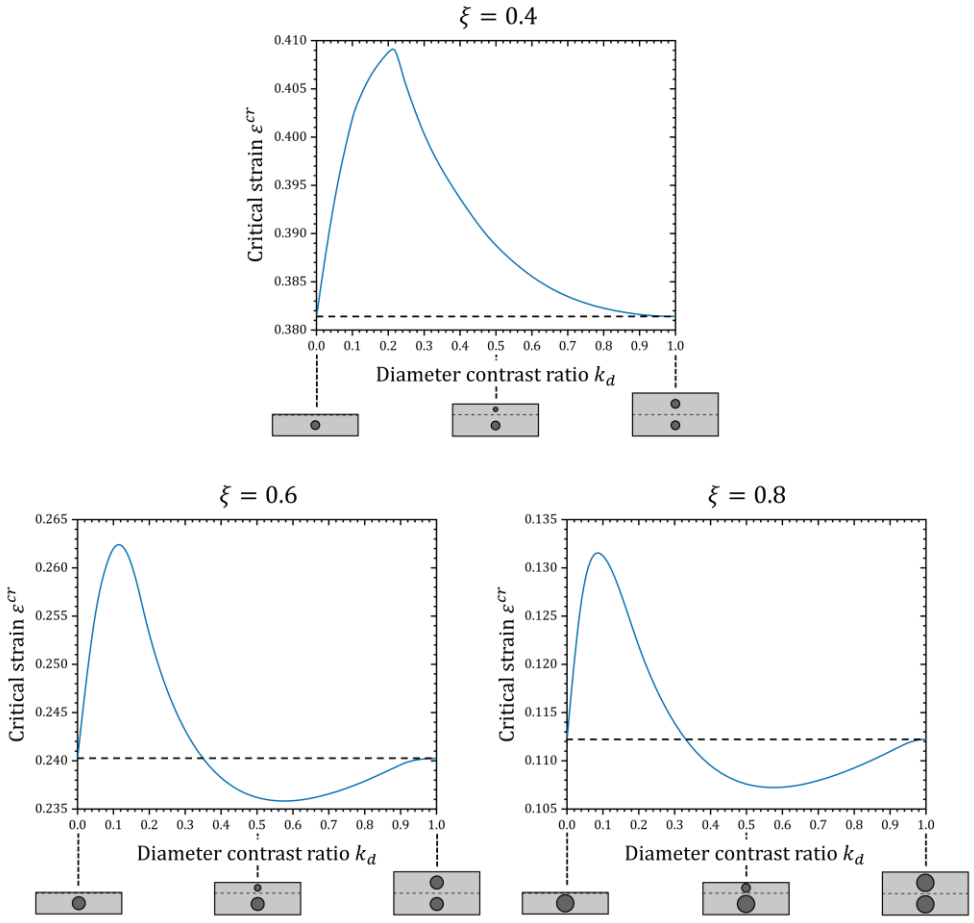

Fig. 33 The dependence of critical strains on inclusion diameter contrast ratio with various spacing ratios in composite with two different-sized inclusions.

In Fig. 33, we observe only microscopic instabilities for all considered diameter contrast ratios in composites with fixed spacing ratios $\xi = 0.4$, $\xi = 0.6$ and $\xi = 0.8$. This stems from the high periodicity aspect ratio $\eta = 8$ used in those cases, where the composites can be considered as nearly a single column of inclusions embedded in the pure soft matrix. Next, we find that, interestingly, with the same spacing ratio, the composites with the diameter contrast ratio $k_d \to 0$ and $k_d = 1$ always have identical critical strains. For example, with spacing ratio $\xi = 0.6$, the composite with $k_d \to 0$ has $\varepsilon^{cr} \to 0.2403$ while the composite with $k_d = 1$ has the identical critical strain $\varepsilon^{cr} = 0.2403$. We realize that, in the composites with $k_d = 1$, the two inclusions have actually the same size; thus, the behavior of the composite is identical to the composite consisting of unit cells with single-sized inclusions. However, for the composites with $k_d \to 0$, the smaller inclusion(between the two) has a diameter of nearly zero, which takes a nearly ignorable effect in the particulate system; thus, the behavior of the composites with two different-sized inclusions is infinitely close to those with single-sized inclusions. We checked the single-inclusion results discussed in Sec. 4.1.1.1 and found that they agree well with the results corresponding to two different-sized inclusions at $k_d \to 0$ and $k_d = 1$. For example, see the black dash line shown in Fig. 33 corresponding to $\xi = 0.6$, the corresponding composite with single-sized inclusions has the critical strain $\varepsilon^{cr} = 0.2402$.

Finally, we notice that, for spacing ratios $\xi = 0.4$, $\xi = 0.6$, and $\xi = 0.8$, the critical strain has obviously non-monotonic dependence on the diameter contrast ratio. For large enough spacing ratios, such as $\xi = 0.6$ and $\xi = 0.8$, the critical strain decreases initially with a decrease in the diameter contrast ratio from $k_d = 1$. Consequently, in those composites, there exists a range of diameter contrast ratios where the composites with two different-sized

inclusions buckle earlier than those with single-sized ones corresponding to the same spacing ratio. With a continuous decrease in the diameter contrast ratio, after k_d reaching a local minimum, the critical strain turns to increase with a further decrease in the diameter contrast ratio. Then it surpasses the critical strain of the composite with single-sized inclusion (the black dash line shown in Fig. 33). Therefore, for large enough spacing ratios, there exists another range of diameter contrast ratio where the composites with two different-sized inclusions buckle later than those with single-sized ones. Finally, after reaching a local maximum at a low enough diameter contrast ratio, the critical strain turns back to decreasing with a decrease of the diameter contrast ratio towards zero and eventually reaches the critical strain of the composite with single-sized inclusions.

For small enough spacing ratios, such as $\xi = 0.4$, we observe that the critical strain increases initially with a decrease in the diameter contrast ratio from $k_d = 1$. Therefore, the composites with two different-sized inclusions always buckle later than those with single-sized ones corresponding to the same spacing ratio. Finally, after reaching a local maximum at a low enough k_d, the critical strain switch to decreasing and eventually reach back to the critical strain of the composite with single-sized inclusions.

4.2.1.2 Dependence of critical wavenumber on geometric parameters

Next, we examine the dependence of the critical wavenumber on the diameter contrast ratio of the particulate composite with two different-sized inclusions. Fig. 34, Fig. 35, and Fig. 36 plot the dependence of the critical wavenumber on the diameter contrast ratio k_d for various fixed values of spacing ratios $\xi = 0.4$, $\xi = 0.6$ and $\xi = 0.8$, respectively. First, we

discuss the results with relatively low spacing ratios, such as $\xi = 0.4$. In Fig. 34, we observed that, for a low enough diameter contrast ratio, the instability develops in a microscopic mode with the critical wavenumber $k^{cr} = 0.25$. The corresponding buckling pattern is a zigzag chain of inclusions with exactly four inclusions (two large and two small inclusions) in one wave period (see, for example, the buckling pattern illustrated in Fig. 34(1) corresponding to $k_d = 0.2$). The critical wavenumber, however, starts to increase after a threshold value of the diameter contrast ratio at $k_d^{th} \approx 0.3$ and finally reaches a plateau of $k^{cr} = 0.5$ after $k_d \approx 0.45$. The buckling mode corresponding to $k^{cr} = 0.5$ is called the "periodicity doubling" mode that has been discussed in Sec. 4.1.1.2. However, due to different sizes of the inclusions, the formed "periodicity doubling" pattern is not geometrically balanced with respect to the unit-cell's central axis, namely, not having the same volume fraction of stiff inclusions on the right and left side of the composite (see the buckling pattern illustrated in Fig. 34(3) corresponding to $k_d = 0.6$). Nevertheless, the buckling pattern finally maintains an overall straight "two columns of inclusions" despite the imbalance. This is due to the fact that the materials in between inclusions are strengthened under compression; thus, via the highly nonlinear stress field, the structure finally accommodates balanced stiffness on the two sides. Finally, when we go back to look at the intermediate critical wavenumber in-between $k^{cr} = 0.25$ and $k^{cr} = 0.5$, such as $k^{cr} = 0.365$ (see the buckling pattern illustrated in Fig. 34(2) corresponding to $k_d = 0.4$), we observe the formation of "seemingly chaotic" arrangement of inclusions in the buckling mode. This stems from the fact that the critical wavelength corresponds to a non-integer number of inclusions (including the large and the small ones), and the composite fails to accommodate an ordered structure in the critical length scales (refer to

Sec. 4.1.1.2 for detailed discussions).

We also notice that the composite corresponding to $k_d = 1$ has seemingly the same buckling pattern as that corresponding to $k_d \to 0$, while the value of the critical wavenumber is halved (for example, $k^{cr} = 0.5$ with $k_d = 1$, while $k^{cr} = 0.25$ with $k_d \to 0$). We realize that, with $k_d \to 0$, in a wave period of the "zigzag chain" pattern, two of the four inclusions are now infinitely small and can be ignored in both visual inspection and physical effects. Therefore, the corresponding buckling pattern is observed the same as a "periodicity doubling" mode. This agrees with our discussion in Sec. 4.2.1.1, where we consider the composites with the diameter contrast ratio $k_d \to 0$ and $k_d = 1$ having the same buckling behavior as the composite with single-sized inclusions. Nevertheless, the infinitely small inclusions with $k_d \to 0$ are still counted for the calculation and normalization of the critical wavenumber, resulting in the critical wavenumber with $k_d \to 0$ exactly a half of that with $k_d = 1$.

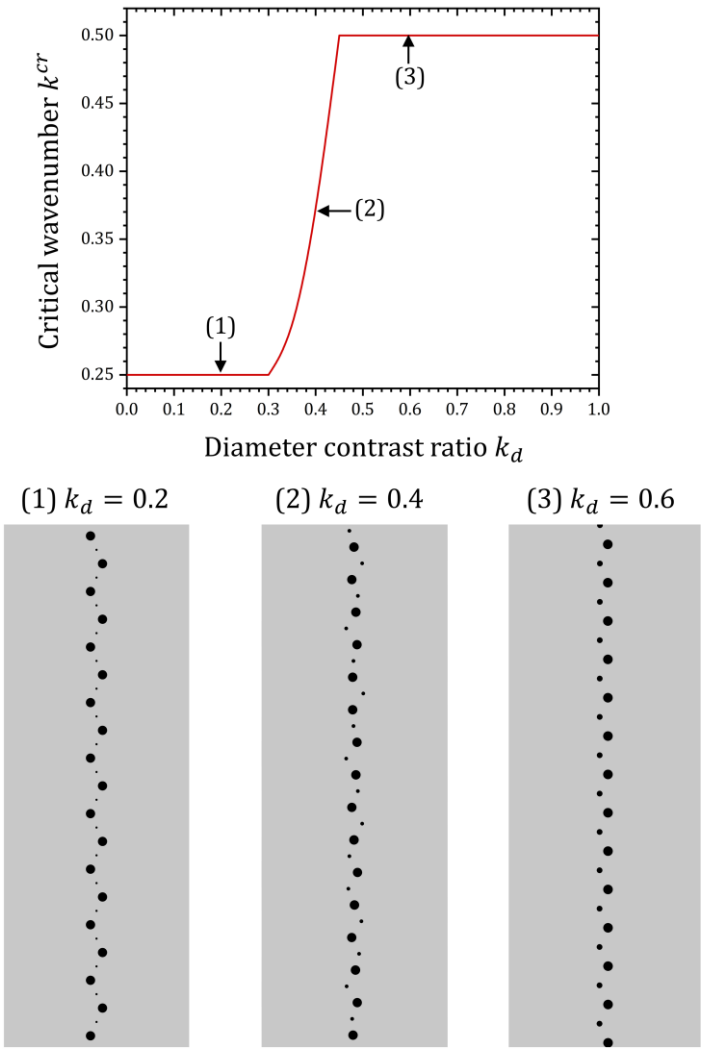

Fig. 34 The dependence of critical wavenumber on inclusion diameter contrast ratio with spacing ratio $\xi = 0.4$ in composite with two different-sized inclusions.

Next, we discuss the results with a moderate spacing ratio, such as $\xi = 0.6$. In Fig. 35, we observe that the critical wavenumber stays in a platform value at $k^{cr} = 0.25$ for a moderate diameter contrast ratio $0.2 \lesssim k_d \lesssim 0.9$, corresponding to the "zigzag chain" pattern with four inclusions in a wave period (see, for example, the buckling pattern illustrated in Fig. 35(2) corresponding to $k_d = 0.4$). However, when the diameter contrast ratio increases beyond $k_d \approx 0.9$, the critical wavenumber starts increasing from $k^{cr} = 0.25$ and finally reaches $k^{cr} = 0.30$ at $k_d = 1$, identical to the critical wavenumber of the composite with single-sized

inclusions. We observe that, for those critical wavenumbers between $k^{cr} = 0.25$ and $k^{cr} = 0.30$ (such as $k^{cr} = 0.285$), the buckling pattern exhibits a beat-like phenomenon, showing short waves with variable magnitudes (see the buckling pattern shown in Fig. 35(2)), which is similar to some special results of the single-sized inclusion model discussed in Sec. 4.1.1.2. To the contrary, when the diameter contrast ratio decreases bellow $k_d \approx 0.2$, the critical wavenumber starts decreasing from $k^{cr} = 0.25$ and finally reaches $k^{cr} = 0.15$, which is exactly identical to a half of the critical wavenumber of the composite with single-sized inclusions.

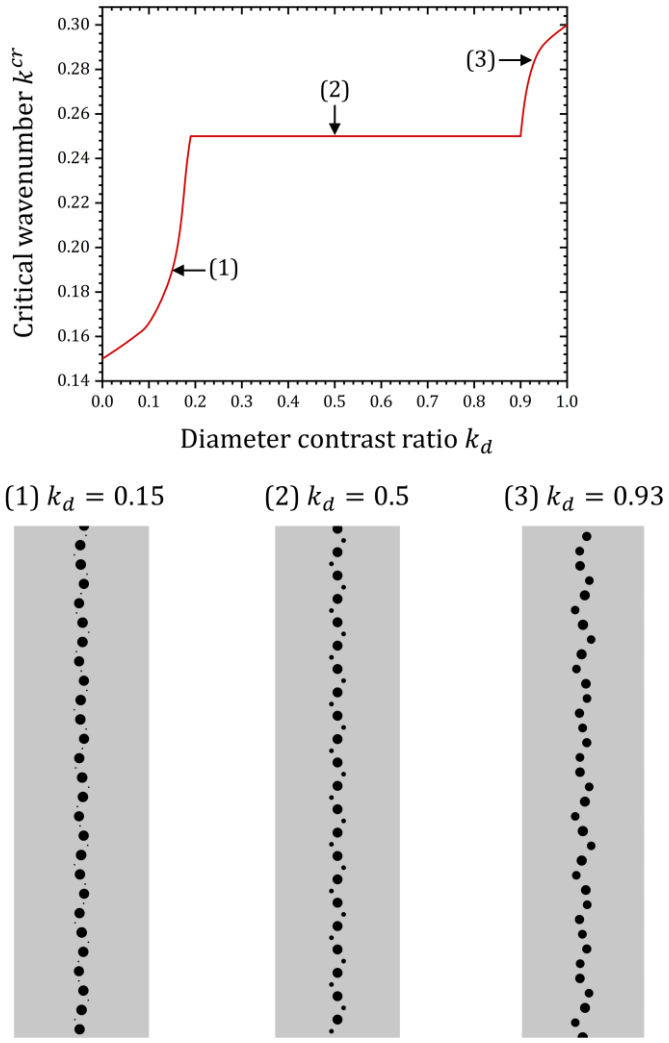

Fig. 35 The dependence of critical wavenumber on inclusion diameter contrast ratio with spacing ratio $\xi = 0.6$ in composite with two different-sized inclusions.

Finally, we discuss the results with a relatively large spacing ratio, such as $\xi = 0.8$. In Fig. 36, we observe the critical wavenumber staying at a platform value $k^{cr} = 0.25$ for a moderate diameter contrast ratio $0.2 \lesssim k_d \lesssim 0.92$, where the buckling mode exhibits the "zigzag chain" pattern with four inclusions in a wave period (see, for example, the buckling pattern illustrated in Fig. 36(2) corresponding to $k_d = 0.6$). However, the critical wavenumber starts decreasing from $k^{cr} = 0.25$ when the diameter contrast ratio either increases beyond $k_d \approx 0.92$ or decreases bellow $k_d \approx 0.2$. Eventually, the critical wavenumber reaches $k^{cr} = 0.219$ (identical to the result with single-sized inclusions) at $k_d = 1$ or approach $k^{cr} \to 0.1095$ (half of the result with single-sized inclusions) at $k_d \to 0$. Interestingly, the buckling pattern exhibits a beat-like phenomenon with $k_d \gtrsim 0.92$ (see, for example, the buckling pattern illustrated in Fig. 36(3) corresponding to $k_d = 0.95$) and a "seemingly chaotic" arrangement of inclusions with $k_d \lesssim 0.2$ (see, for example, the buckling pattern illustrated in Fig. 36(1) corresponding to $k_d = 0.1$).

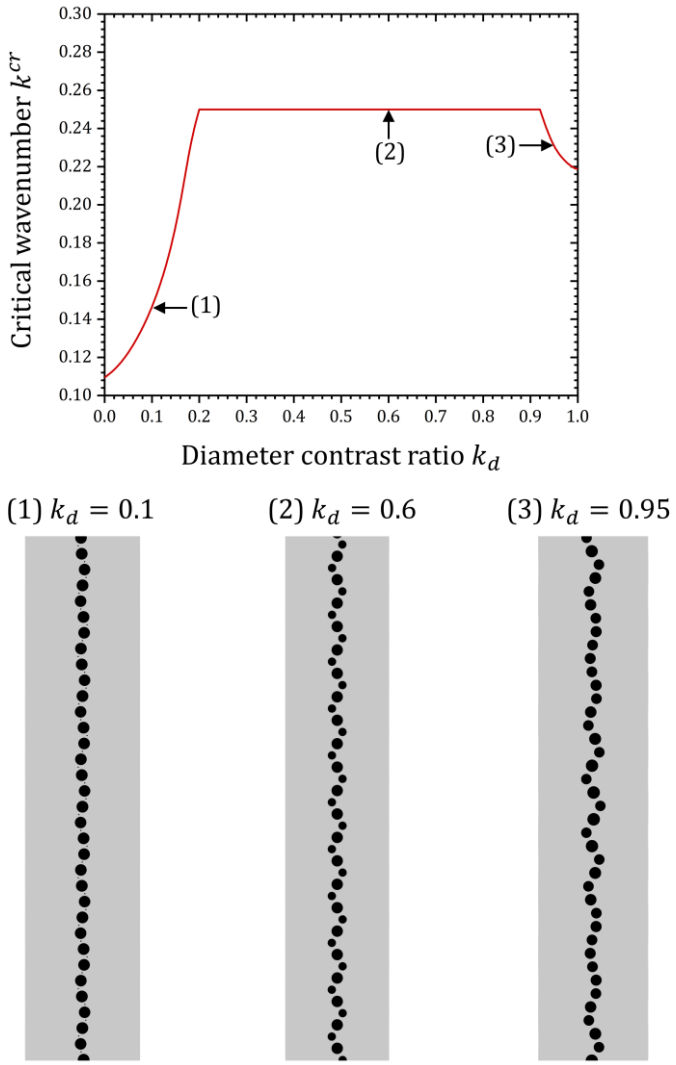

Fig. 36 The dependence of critical wavenumber on inclusion diameter contrast ratio with spacing ratio $\xi = 0.8$ in composite with two different-sized inclusions.

4.3 Composite(3D) with single-sized inclusions

4.3.1 Bloch-Floquet prediction

4.3.1.1 Dependence of strain on geometric parameters

In this section, we examine the dependence of the critical strain on the initial geometrical parameters of the 3D particulate composites. Fig. 37 shows the dependence of the critical strain on the periodicity aspect ratio η for various fixed values of the inclusion spacing ratios ξ from 0.2 to 0.9. Note that, similar to that in the 2D composites, the admissible geometries are

restricted by inclusions not exceeding the cell's boundaries by $d < b$ and $d < a$. Therefore, the parameter space is limited to $\eta > \xi$. Also similar to our illustration of 2D results in Sec. 4.1, the dotted and continuous curves correspond to longwave (or macroscopic) and microscopic instabilities, respectively.

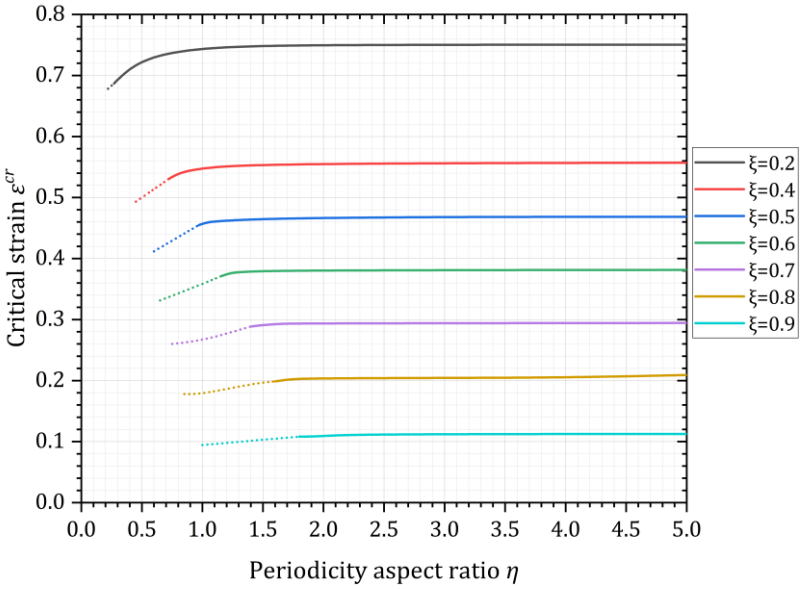

Fig. 37 The dependence of critical strain on periodicity aspect ratio with various spacing ratios for 3D particulate composites. Dotted and continuous curves correspond to macroscopic and microscopic instabilities, respectively.

For 3D results, we observe earlier buckling in the composites with higher spacing ratios, which agrees with the similar trends in 2D results. For both 2D and 3D inclusions, a higher spacing ratio will result in the inclusions being placed more closely in the compressive direction, bringing stronger inter-inclusion interactions and leading to earlier instability development. Interestingly, in 3D particulate composites, the dependence of the critical strain on the periodicity aspect ratio is observed as monotonic for all our numerical cases. Recall that we observed non-monotonic dependence for 2D composites with large enough spacing ratios, considered as the manifestation of two different dominating buckling behaviors in two soft

particulate systems (see the discussion in Sec. 4.1.1.1 for details). However, the 3D particles actually possess smaller volume fractions than 2D particles at the same spacing ratio, since the 2D inclusions occupy a column space in their 3D extrusion while the 3D particle is a sphere enclosed in the column (see the illustration shown in Fig. 38). Therefore, the behavior of 3D composites is corresponding to 2D composites with lower spacing ratio, thus, exhibits monotonic dependence of the critical strain on the initial geometrical parameters. This understanding is also reflected by our results showing that the 3D composites always buckle latter than the 2D composites with the same initial geometrical parameters (see the comparison between 2D and 3D results in Fig. 11 and Fig. 37, respectively).

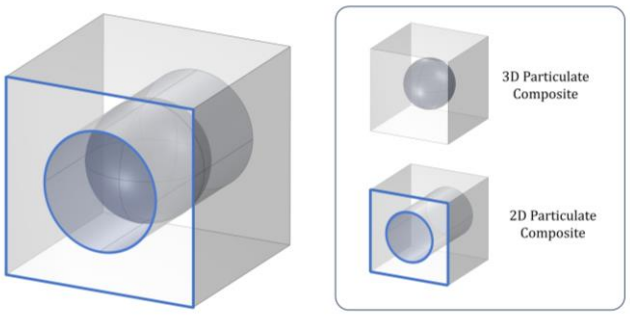

Fig. 38 Schematic microstructure of the 3D particulate composite and the 3D extrusion of the 2D particulate composite.

4.3.1.2 Dependence of critical wavenumber on geometric parameters

Next, we examine the dependence of the critical wavenumber on the periodicity aspect ratio η for various fixed values of the inclusion spacing ratios ξ from 0.2 to 0.9. The results are plotted in Fig. 39. We observe that the 3D composites experience macroscopic or longwave instability ($k^{cr} \to 0$) for small enough periodicity aspect ratios. After reaching a threshold value η^{th} (dictated by the initial spacing ratio value ξ), the buckling mode switches from macroscopic to microscopic ones. Similar to the 2D results, the transition from macro- to

micro-instability modes exhibits a binary switch from $k^{cr} \to 0$ to $k^{cr} = 0.5$ for small enough spacing ratios such as $\xi = 0.2$ and $\xi = 0.3$, namely, the "jump-transition". In 3D composites with modest periodicity aspect ratios, the corresponding critical wavenumber continuously increases from $k^{cr} \to 0$ to $k^{cr} = 0.5$. For the composites with high enough spacing ratios, such as $\xi = 0.9$, the critical wavenumber continuously increases from $k^{cr} \to 0$ but never reaches $k^{cr} = 0.5$. However, by comparing the 2D and 3D results with the same spacing and periodicity aspect ratios, we find the 3D composites behave similarly to 2D composites with lower spacing ratios. For example, 3D composites with $\xi = 0.8$ exhibits a "full-transition" mode from macro- to microscopic insanities, while this transition mode typically occurs in 2D composites with $\xi \precsim 0.465$; the critical wavenumber corresponding to 3D composites with $\xi = 0.9$ finally converges to $k^{cr} \to 0.321$ with large enough η, which is similar to that in the 2D composite with $\xi = 0.6$, where the critical wavenumber finally converges to $k^{cr} \to 0.3$.

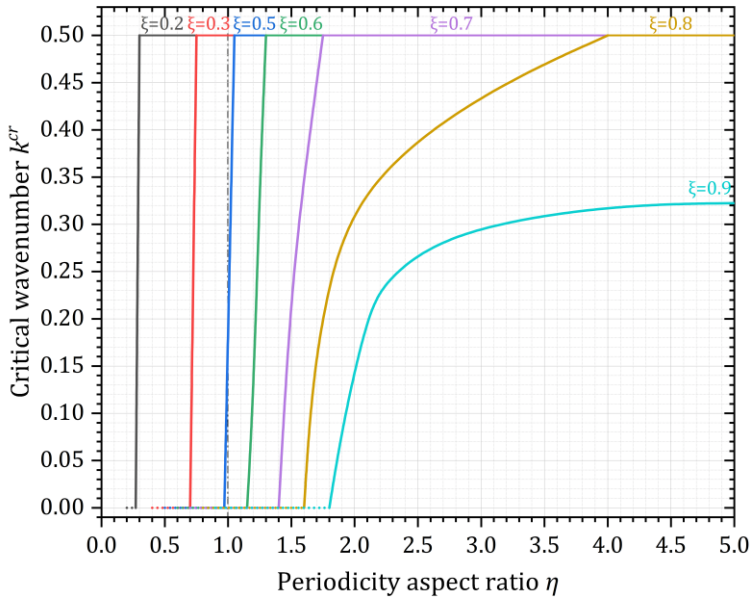

Fig. 39 The dependence of critical wavenumber on periodicity aspect ratio with various spacing ratios for 3D particulate composites. Dotted and continuous curves correspond to macroscopic and microscopic instabilities, respectively.

5. Conclusion

In this dissertation research, I have examined the instabilities in soft particulate composites and the corresponding pattern transformations via various numerical approaches and in different forms and dimensions of composite microstructures.

Overall, I have conducted numerical studies including the i) Bloch-Floquet analysis; ii) the Post-Buckling analysis; iii) the Energy quasi-convexification analysis, and iv) a Hybrid method that implements Bloch-Floquet analysis in the Post-Buckling regime. I have also developed a post-processing method based on the discrete Fourier transformation (DFT) for characterizing post-buckling development. I have also considered different forms of particulate composites, including a) 2D rectangular unit cells with single-sized inclusions, b) 2D rectangular unit cells with two different-sized inclusions, and c) 3D cuboid unit cells with single-sized sphere inclusions. More importantly, I have been focusing on the whole process study of the instability development in soft particulate composites, from prior- to post-buckling regimes, which helped to uncover a distinctive buckling phenomenon where a secondary instability occurs in the post-buckling regime. The results and findings in the dissertation can be concluded as follows:

1) For 2D particulate composites with single-sized inclusions. It has been shown that the instabilities are accompanied by the collapse of the initial straight columns of inclusions beyond the critical strain level and are followed by the formation of various buckling patterns. The buckling patterns predicted by Bloch-Floquet analysis are characterized by the corresponding instability eigenmodes. In particular, those eigenmodes exhibit (i) strictly doubled periodicity, (ii) seemingly non-periodic state, or (iii) longwave pattern, determined

by the initial geometric parameters. The seemingly non-periodic eigenmode occurs with a finite critical wavenumber lower than 0.5, indicating a non-integer number of periods. However, the post-buckling analysis, which considers the nonlinearity in the post-buckling development, predicted buckling patterns with additional and more accurate details. Specifically, the formation of various post-buckling patterns has been observed: i) the "wavy-chain" of inclusions, ii) the "zigzag-chain" of inclusions, ii) the "periodicity doubling" patterns, and iv) the "superposed" patterns (a combination of inclusion sets in different length scales), determined by the composite's initial geometry. Nevertheless, the critical strains predicted by the Bloch-Floquet and the post-buckling analysis exhibit good agreement. Moreover, the dependence of critical strains on the composite's initial geometric parameters reflects a transition of buckling behavior as the composite's manifestation of two soft particulate systems. The transition between these two different soft particulate systems has also been illustrated via the corresponding transition of energy landscapes. In particular, by further examination of the development of buckling patterns in their post-buckling regime, a distinctive phenomenon – the development of a *secondary* buckling in soft particulate composites – has been numerically discovered, providing a new array of instability patterns and opening a new area of interest in buckling analysis.

2) For 2D particulate composites with two different-sized inclusions. I have shown the influence of the diameter contrast ratio (between the two different-sized inclusion) on the instability characteristics of the composite. Specifically, with small enough inclusion spacing ratios, the composites with two different-sized inclusions buckle latter than those with single-sized inclusions, with whatever diameter contrast ratios; while having large

enough inclusion spacing ratios, the composites with two different-sized inclusions may buckle latter or earlier than those with single-sized ones, determined on the diameter contrast ratios. Finally, the buckling patterns of the composites with two different-sized inclusions have been found to transit between a) the “zigzag chain” pattern with four inclusions in a wave period, b) the “periodicity doubling pattern” and c) the buckling pattern corresponding to the composite with single-sized inclusions.

3) For 3D particulate composites, the results have shown that their buckling behavior is similar to the corresponding 2D composites with a lower spacing ratio, which is attributed to the fact that the 3D particles always possess a smaller volume fraction than the extrusion of 2D particles at the same spacing ratio.

Based on the obtained results, it can also be realized that the accuracy of predictions using various numerical approaches depends upon the form of stiff phases present in the composites. Specifically, in composites with continuous stiff phases like stiff fibers and layers, the Bloch-Floquet analysis proves to be both accurate and efficient. However, when dealing with composites containing discretely distributed stiff phases, such as 2D and 3D particles, the post-buckling analysis (combined with the DFT characterization) yields better accuracy and provides more details into the pattern transformations. More interestingly, the Bloch-Floquet and post-buckling analyses demonstrate a good agreement for analyzing the secondary buckling phenomenon in the post-buckling regime. This behavior stems from the formation of the effective "particle-reinforced layer," which exhibits characteristics of both continuous and discrete stiff phases.

It should be noted that, in this study, the composite has been modeled with neo-Hookean

energy, which helped minimize the number of material parameters and focus on the interplay between the composite's micro-geometry and its instabilities. However, the high-level deformations met in our study could cause stiffening behavior (Arruda et al., 1993; Davidson et al., 2013; Gent, 1996; Xiang et al., 2022b) of the polymeric materials, which the neo-Hookean model is unable to capture accurately. Moreover, many soft materials, such as polymers and hydrogels, frequently exhibit strong nonlinear viscoelastic behavior (Naik et al., 2018; Wu et al., 2018; Mao et al., 2017; Xiang et al., 2020b; Hong et al., 2011; Kumar et al., 2016). The interplay between viscoelasticity and instabilities in soft particulate composites undergoing finite deformation has also been reported (Xiang et al., 2023). Therefore, for future work, more complicated material models, such as those considering stiffening or viscoelastic behaviors, will be introduced into the numeral models. Their influence on critical loadings and critical instability modes, as well as their post-buckling development, will be further investigated.

Appendix A The influence of the number of unit cells in the RVE for post-buckling analysis

In this section, we show the influence of the number of unit cells (built in the RVE) on the DFT analysis results of the post-buckling development. We build multiple numerical models with different numbers of unit cells in the RVE (in particular, $N = 20, N = 40, N = 80, N = 120, N = 160,$ and $N = 200$). The corresponding DFT results at the compressive strain level $\varepsilon = 0.237$ are shown in Fig. 40, where the Fourier coefficient of each curve is scaled so that their Fourier peak coefficients are all equal to one. We observe that as the number of unit cells

N increases, the peak point of the curve slightly shifts and finally converges to $k^{cr} = 0.145$. A larger N can increase the precision of identifying the critical wavenumber since more wavenumbers are scanned. The results also show that $N = 80$ provides enough precision for the numerical simulation. For all post-buckling analyses using DFT characterization, we use the number of unit cells in the RVE no less than $N = 80$. For post-buckling analysis of secondary buckling, we use even $N = 320$ unit cells in the RVE, which ensures the precision of both FE simulation and the RVE characterization.

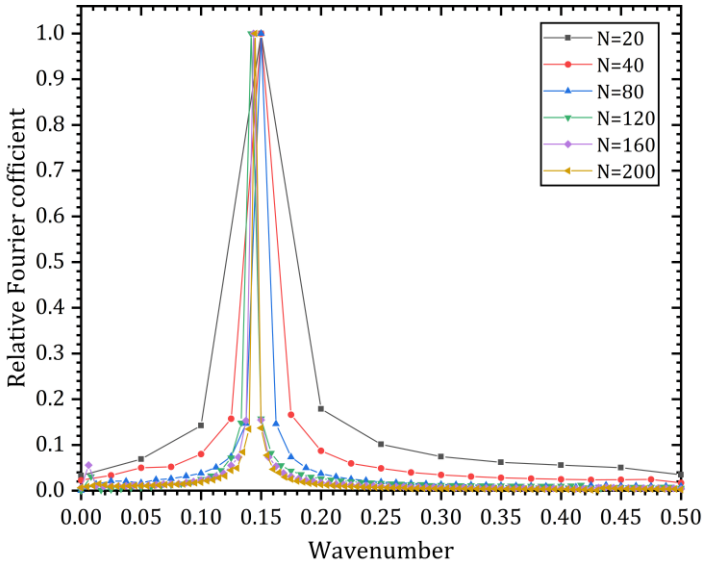

Fig. 40 The DFT results of the post-buckling development for composite with spacing ratio $\xi = 0.6$ and periodicity aspect ratio $\eta = 2.1$ at compressive strain $\varepsilon = 0.237$, for various numbers of unit cells built in the RVE ($N = 20, N = 40, N = 80, N = 120, N = 160,$ and $N = 200$).

Bibliography

[1] Aboudi, J., & Gilat, R. (2023). Bifurcation buckling and the effect of imperfections on the microbuckling of soft materials with periodic microstructure by the finite strain HFGMC micromechanics. International Journal of Solids and Structures, 270, 112227.

[2] Aboudi, J., & Volokh, K. Y. (2020). Modeling deformation and failure of viscoelastic composites at finite strains. Mechanics of Soft Materials, 2, 1-19.

[3] Acome, E., Mitchell, S. K., Morrissey, T. G., Emmett, M. B., Benjamin, C., King, M., ... & Keplinger, C. (2018). Hydraulically amplified self-healing electrostatic actuators with muscle-like performance. Science, 359(6371), 61-65.

[4] Arora, N., Batan, A., Li, J., Slesarenko, V., & Rudykh, S. (2019). On the influence of inhomogeneous interphase layers on instabilities in hyperelastic composites. Materials, 12(5).

[5] Arora, N., Yao, Q., & Rudykh, S. (2022a). Deformation activated negative group velocity state in soft laminates. Extreme Mechanics Letters, 51, 101592.

[6] Arora, N., Li, J., & Rudykh, S. (2022b). Tunable buckling configurations via in-plane periodicity in soft 3D-fiber composites: Simulations and experiments. International Journal of Solids and Structures, 250.

[7] Arruda, E. M., & Boyce, M. C. (1993). A three-dimensional constitutive model for the large stretch behavior of rubber elastic materials. Journal of the Mechanics and Physics of Solids, 41(2), 389-412.

[8] Auguste, A., Yang, J., Jin, L., Chen, D., Suo, Z., & Hayward, R. C. (2018). Formation of high aspect ratio wrinkles and ridges on elastic bilayers with small thickness contrast. Soft Matter, 14(42), 8545-8551.

[9] Babaee, S., Viard, N., Wang, P., Fang, N. X., & Bertoldi, K. (2016). Harnessing deformation to switch on and off the propagation of sound. Advanced Materials, 28(8), 1631-1635.

[10] Bae, H. J., Bae, S., Park, C., Han, S., Kim, J., Kim, L. N., ... & Kwon, S. (2015). Biomimetic microfingerprints for anti-counterfeiting strategies. Advanced Materials, 27(12), 2083-2089.

[11] Bertoldi, K., Boyce, M. C., Deschanel, S., Prange, S. M., & Mullin, T. (2008). Mechanics of deformation-triggered pattern transformations and superelastic behavior in periodic elastomeric structures. Journal of the Mechanics and Physics of Solids, 56(8), 2642–2668.

[12] Bertoldi, K., Reis, P., Willshaw, S., materials, T. M.-A., & 2010, undefined. (2010). Negative Poisson's ratio behavior induced by an elastic instability. Wiley Online Library, 22(3), 361–366.

[13] Brau, F., Damman, P., Diamant, H., & Witten, T. A. (2013). Wrinkle to fold transition: influence of the substrate response. Soft Matter, 9(34), 8177-8186.

[14] Brau, F., Vandeparre, H., Sabbah, A., Poulard, C., Boudaoud, A., & Damman, P. (2011). Multiple-length-scale elastic instability mimics parametric resonance of nonlinear oscillators. Nature Physics, 7(1), 56-60.

[15] Bruno, D., Greco, F., Lonetti, P., Blasi, P. N., & Sgambitterra, G. (2010). An investigation on microscopic and macroscopic stability phenomena of composite solids with periodic microstructure. International Journal of Solids and Structures, 47(20), 2806–2824.

[16] Budday, S., Steinmann, P., & Kuhl, E. (2014). The role of mechanics during brain development. Journal of the Mechanics and Physics of Solids, 72, 75-92.

[17] Cai, S., Breid, D., Crosby, A. J., Suo, Z., & Hutchinson, J. W. (2011). Periodic patterns and energy states of buckled films on compliant substrates. Journal of the Mechanics and Physics of Solids, 59(5), 1094-1114.

[18] Cao, Y., & Hutchinson, J. W. (2012). From wrinkles to creases in elastomers: the instability and imperfection-sensitivity of wrinkling. Proceedings of the Royal Society A: Mathematical, Physical and Engineering Sciences, 468(2137), 94-115.

[19] Chen, D., Arora, N., Xiang, Y., Li, J., Slesarenko, V., & Rudykh, S. (2022). Instability-induced patterns and their post-buckling development in soft particulate composites. Mechanics of Materials, 175, 104482.

[20] Chen, D., Xiang, Y., Arora, N., Yao, Q., Li, J., & Rudykh, S. (2023). Post-buckling development in soft particulate composites. Composite Structures, 117337.

[21] Chen, L. L., Lian, H., Liu, Z., Chen, H. B., Atroshchenko, E., & Bordas, S. P. A. (2019). Structural shape optimization of three dimensional acoustic problems with isogeometric boundary element methods. Computer Methods in Applied Mechanics and Engineering, 355, 926–951.

[22] Chen, X., & Hutchinson, J. W. (2004). Herringbone buckling patterns of compressed thin films on compliant substrates. J. Appl. Mech., 71(5), 597-603.

[23] Chen, Y. C., & Crosby, A. J. (2014). High aspect ratio wrinkles via substrate prestretch. Advanced Materials, 26(32), 5626-5631.

[24] Cheng, H., & Song, J. (2014). A simply analytic study of buckled thin films on compliant substrates. Journal of Applied Mechanics, 81(2), 024501.

[25] Choi, W. M., Song, J., Khang, D. Y., Jiang, H., Huang, Y. Y., & Rogers, J. A. (2007). Biaxially stretchable “wavy” silicon nanomembranes. Nano letters, 7(6), 1655-1663.

[26] Chung, J. Y., Lee, J. H., Beers, K. L., & Stafford, C. M. (2011). Stiffness, strength, and ductility of nanoscale thin films and membranes: a combined wrinkling–cracking methodology. Nano

letters, 11(8), 3361-3365.

[27] Davidson, J. D., & Goulbourne, N. C. (2013). A nonaffine network model for elastomers undergoing finite deformations. Journal of the Mechanics and Physics of Solids, 61(8), 1784-1797.

[28] De Maio, U., Greco, F., Luciano, R., Sgambitterra, G., & Pranno, A. (2023). Microstructural design for elastic wave attenuation in 3D printed nacre-like bioinspired metamaterials lightened with hollow platelets. Mechanics Research Communications, 104045.

[29] Ding, C., Deokar, R. R., Ding, Y., Li, G., Cui, X., Tamma, K. K., & Bordas, S. P. A. (2019). Model order reduction accelerated Monte Carlo stochastic isogeometric method for the analysis of structures with high-dimensional and independent material uncertainties. Computer Methods in Applied Mechanics and Engineering, 349, 266–284.

[30] Du, Y., Su, Y., Lü, C., Chen, W., & Destrade, M. (2020). Electro-mechanically guided growth and patterns. Journal of the Mechanics and Physics of Solids, 143, 104073.

[31] Ebata, Y., Croll, A. B., & Crosby, A. J. (2012). Wrinkling and strain localizations in polymer thin films. Soft Matter, 8(35), 9086-9091.

[32] Efimenko, K., Rackaitis, M., Manias, E., Vaziri, A., Mahadevan, L., & Genzer, J. (2005). Nested self-similar wrinkling patterns in skins. Nature materials, 4(4), 293-297.

[33] Ehret, A. E., & Itskov, M. (2007). A polyconvex hyperelastic model for fiber-reinforced materials in application to soft tissues. Journal of Materials Science, 42, 8853-8863.

[34] Elouneg, A., Sutula, D., Chambert, J., Lejeune, A., Bordas, S. P. A., & Jacquet, E. (2021). An open-source FEniCS-based framework for hyperelastic parameter estimation from noisy full-field data: Application to heterogeneous soft tissues. Computers and Structures, 255.

[35] Galich, P. I., Slesarenko, V., Li, J., & Rudykh, S. (2018). Elastic instabilities and shear waves in hyperelastic composites with various periodic fiber arrangements. International Journal of Engineering Science, 130, 51–61.

[36] Gao, N., Li, J., Bao, R. H., & Chen, W. Q. (2019). Harnessing uniaxial tension to tune Poisson's ratio and wave propagation in soft porous phononic crystals: an experimental study. Soft Matter, 15(14), 2921–2927.

[37] Garcia, K. E., Kroenke, C. D., & Bayly, P. V. (2018). Mechanics of cortical folding: stress, growth and stability. Philosophical Transactions of the Royal Society B: Biological Sciences,

373(1759), 20170321.

[38] Gent, A. N. (1996). A new constitutive relation for rubber. Rubber chemistry and technology, 69(1), 59-61.

[39] Geymonat, G., Müller, S., & Triantafyllidis, N. (1993). Homogenization of nonlinearly elastic materials, microscopic bifurcation and macroscopic loss of rank-one convexity. Archive for Rational Mechanics and Analysis, 122(3), 231–290.

[40] Goshkoderia, A., & Rudykh, S. (2017). Stability of magnetoactive composites with periodic microstructures undergoing finite strains in the presence of a magnetic field. Composites Part B: Engineering, 128, 19-29.

[41] Goshkoderia, A., Chen, V., Li, J., Juhl, A., Buskohl, P., & Rudykh, S. (2020). Instability-Induced Pattern Formations in Soft Magnetoactive Composites. Physical Review Letters, 124(15), 1–7.

[42] Greco, F., & Luciano, R. (2011). A theoretical and numerical stability analysis for composite micro-structures by using homogenization theory. Composites Part B: Engineering, 42(3), 382-401.

[43] Greco, F., Leonetti, L., De Maio, U., Rudykh, S., & Pranno, A. (2021). Macro- and micro-instabilities in incompressible bioinspired composite materials with nacre-like microstructure. Composite Structures, 269.

[44] Greco, F., Lonetti, P., Luciano, R., Blasi, P. N., & Pranno, A. (2018). Nonlinear effects in fracture induced failure of compressively loaded fiber reinforced composites. Composite Structures, 189, 688-699.

[45] Hauseux, P., Hale, J. S., & Bordas, S. P. A. (2017). Accelerating Monte Carlo estimation with derivatives of high-level finite element models. Computer Methods in Applied Mechanics and Engineering, 318, 917–936.

[46] Hauseux, P., Hale, J. S., Cotin, S., & Bordas, S. P. A. (2018). Quantifying the uncertainty in a hyperelastic soft tissue model with stochastic parameters. Applied Mathematical Modelling, 62, 86–102.

[47] Hong, W. (2011). Modeling viscoelastic dielectrics. Journal of the Mechanics and Physics of Solids, 59(3), 637-650.

[48] Huang, Z. Y., Hong, W., & Suo, Z. (2005). Nonlinear analyses of wrinkles in a film bonded to a

compliant substrate. Journal of the Mechanics and Physics of Solids, 53(9), 2101-2118.

[49] Jiang, H., Khang, D. Y., Song, J., Sun, Y., Huang, Y., & Rogers, J. A. (2007). Finite deformation mechanics in buckled thin films on compliant supports. Proceedings of the National Academy of Sciences, 104(40), 15607-15612.

[50] Jin, L., Takei, A., & Hutchinson, J. W. (2015). Mechanics of wrinkle/ridge transitions in thin film/substrate systems. Journal of the Mechanics and Physics of Solids, 81, 22-40.

[51] Kellaris, N., Gopaluni Venkata, V., Smith, G. M., Mitchell, S. K., & Keplinger, C. (2018). Peano-HASEL actuators: Muscle-mimetic, electrohydraulic transducers that linearly contract on activation. Science Robotics, 3(14), eaar3276.

[52] Kim, P., Abkarian, M., & Stone, H. A. (2011). Hierarchical folding of elastic membranes under biaxial compressive stress. Nature materials, 10(12), 952-957.

[53] Kim, Y., Yuk, H., Zhao, R., Chester, S. A., & Zhao, X. (2018). Printing ferromagnetic domains for untethered fast-transforming soft materials. Nature, 558(7709), 274-279.

[54] Kumar, A., & Lopez-Pamies, O. (2016). On the two-potential constitutive modeling of rubber viscoelastic materials. Comptes Rendus Mecanique, 344(2), 102-112.

[55] Laroussi, M., Sab, K., & Alaoui, A. (2002). Foam mechanics: nonlinear response of an elastic 3D-periodic microstructure. International Journal of Solids and Structures, 39(13-14), 3599-3623.

[56] Li, B., Cao, Y. P., Feng, X. Q., & Gao, H. (2011). Surface wrinkling of mucosa induced by volumetric growth: theory, simulation and experiment. Journal of the Mechanics and Physics of Solids, 59(4), 758-774.

[57] Li, J., Slesarenko, V., Galich, P. I., & Rudykh, S. (2018a). Instabilities and pattern formations in 3D-printed deformable fiber composites. Composites Part B: Engineering, 148, 114–122.

[58] Li, J., Slesarenko, V., & Rudykh, S. (2018b). Auxetic multiphase soft composite material design through instabilities with application for acoustic metamaterials. Soft Matter, 14(30), 6171–6180.

[59] Li, J., Pallicity, T. D., Slesarenko, V., Goshkoderia, A., & Rudykh, S. (2019a). Domain formations and pattern transitions via instabilities in soft heterogeneous materials. Advanced Materials, 31(14), 1807309.

[60] Li, J., & Rudykh, S. (2019b). Tunable microstructure transformations and auxetic behavior in

3D-printed multiphase composites: The role of inclusion distribution. Composites Part B: Engineering, 172, 352–362.

[61] Li, J., Wang, Y., Chen, W., Wang, Y. S., & Bao, R. (2019c). Harnessing inclusions to tune post-buckling deformation and bandgaps of soft porous periodic structures. Journal of Sound and Vibration, 459, 114848.

[62] Li, J., Slesarenko, V., & Rudykh, S. (2019d). Microscopic instabilities and elastic wave propagation in finitely deformed laminates with compressible hyperelastic phases.

[63] Li, J., Slesarenko, V., & Rudykh, S. (2022). Emergence of instability-driven domains in soft stratified materials. npj Computational Materials, 8(1), 100.

[64] Li, Y., Kaynia, N., Rudykh, S., & Boyce, M. C. (2013). Wrinkling of interfacial layers in stratified composites. Advanced Engineering Materials, 15(10), 921–926.

[65] Lin, P. C., & Yang, S. (2007). Spontaneous formation of one-dimensional ripples in transit to highly ordered two-dimensional herringbone structures through sequential and unequal biaxial mechanical stretching. Applied physics letters, 90(24).

[66] Lin, S., Cohen, T., Zhang, T., Yuk, H., Abeyaratne, R., & Zhao, X. (2016). Fringe instability in constrained soft elastic layers. Soft matter, 12(43), 8899-8906.

[67] Liu, J., Gu, T., Shan, S., Kang, S. H., Weaver, J. C., & Bertoldi, K. (2016). Harnessing buckling to design architected materials that exhibit effective negative swelling. Advanced Materials, 28(31), 6619-6624.

[68] Liu, Z., McBride, A., Sharma, B. L., Steinmann, P., & Saxena, P. (2021). Coupled electro-elastic deformation and instabilities of a toroidal membrane. Journal of the Mechanics and Physics of Solids, 151, 104221.

[69] Mao, Y., Lin, S., Zhao, X., & Anand, L. (2017). A large deformation viscoelastic model for double-network hydrogels. Journal of the Mechanics and Physics of Solids, 100, 103-130.

[70] Mazier, A., Bilger, A., Forte, A. E., Peterlik, I., Hale, J. S., & Bordas, S. P. A. (2022). Inverse deformation analysis: an experimental and numerical assessment using the FEniCS Project. Engineering with Computers.

[71] Mei, H., Landis, C. M., & Huang, R. (2011). Concomitant wrinkling and buckle-delamination of elastic thin films on compliant substrates. Mechanics of Materials, 43(11), 627-642.

[72] Melnikov, A., Ogden, R. W., Dorfmann, L., & Merodio, J. (2021). Bifurcation analysis of

elastic residually-stressed circular cylindrical tubes. International Journal of Solids and Structures, 226–227, 111062.

[73] Merodio, J., & Ogden, R. W. (2002). Material instabilities in fiber-reinforced nonlinearly elastic solids under plane deformation. Archives of Mechanics, 54(5–6), 525–552.

[74] Merodio, J., & Ogden, R. W. (2003). Instabilities and loss of ellipticity in fiber-reinforced compressible non-linearly elastic solids under plane deformation. International Journal of Solids and Structures, 40(18), 4707–4727.

[75] Merodio, J., & Ogden, R. W. (2005a). Remarks on instabilities and ellipticity for a fiber-reinforced compressible nonlinearly elastic solid under plane deformation. Quarterly of applied mathematics, 63(2), 325-333.

[76] Merodio, J., & Ogden, R. W. (2005b). Tensile instabilities and ellipticity in fiber-reinforced compressible non-linearly elastic solids. International Journal of Engineering Science, 43(8-9), 697-706.

[77] Merodio, J., & Pence, T. J. (2001a). Kink surfaces in a directionally reinforced neo-Hookean material under plane deformation: I. Mechanical equilibrium. Journal of Elasticity, 62, 119-144.

[78] Merodio, J., & Pence, T. J. (2001b). Kink surfaces in a directionally reinforced neo-Hookean material under plane deformation: II. Kink band stability and maximally dissipative band broadening. Journal of Elasticity, 62, 145-170.

[79] Michel, J. C., Lopez-Pamies, O., Ponte Castaeda, P., & Triantafyllidis, N. (2010). Microscopic and macroscopic instabilities in finitely strained fiber-reinforced elastomers. Journal of the Mechanics and Physics of Solids, 58(11), 1776–1803.

[80] Müller, S., Triantafyllidis, N., & Geymonat, G. (1993). Homogenization of nonlinearly elastic materials, microscopic bifurcation and macroscopic loss of rank-one convexity.

[81] Mullin, T., Deschanel, S., Bertoldi, K., & Boyce, M. C. (2007). Pattern transformation triggered by deformation. Physical Review Letters, 99(8).

[82] Naik, D. L., & Kiran, R. (2018). On anisotropy, strain rate and size effects in vat photopolymerization based specimens. Additive Manufacturing, 23, 181-196.

[83] Ogden, R. W. (1997). Non-linear elastic deformations, Dover Publication, Mineola, New York.

[84] Pocivavsek, L., Dellsy, R., Kern, A., Johnson, S., Lin, B., Lee, K. Y. C., & Cerda, E. (2008). Stress and fold localization in thin elastic membranes. Science, 320(5878), 912-916.

[85] Pranno, A., Greco, F., Leonetti, L., Lonetti, P., Luciano, R., & De Maio, U. (2022). Band gap tuning through microscopic instabilities of compressively loaded lightened nacre-like composite metamaterials. Composite Structures, 282, 115032.

[86] Qiu, G. Y., & Pence, T. J. (1997). Loss of ellipticity in plane deformation of a simple directionally reinforced incompressible nonlinearly elastic solid. Journal of Elasticity, 49, 31-63.

[87] Rappel, H., Beex, L. A. A., Noels, L., & Bordas, S. P. A. (2019). Identifying elastoplastic parameters with Bayes' theorem considering output error, input error and model uncertainty. Probabilistic Engineering Mechanics, 55, 28–41.

[88] Reddy, N. H., & Saxena, P. (2017). Limit points in the free inflation of a magnetoelastic toroidal membrane. International Journal of Non-Linear Mechanics, 95, 248-263.

[89] Reddy, N. H., & Saxena, P. (2018). Instabilities in the axisymmetric magnetoelastic deformation of a cylindrical membrane. International Journal of Solids and Structures, 136, 203-219.

[90] Rudykh, S., & Boyce, M. C. (2014). Transforming wave propagation in layered media via instability-induced interfacial wrinkling. Physical Review Letters, 112(3).

[91] Rudykh, S., & Debotton, G. (2012). Instabilities of hyperelastic fiber composites: Micromechanical versus numerical analyses. Journal of Elasticity, 106(2), 123–147.

[92] Rudykh, S., Bhattacharya, K., & Debotton, G. (2012). Snap-through actuation of thick-wall electroactive balloons. International Journal of Non-Linear Mechanics, 47(2), 206-209.

[93] Saxena, P. (2021). Modelling instabilities in electroelastic and magnetoelastic membranes: a very brief review. arXiv preprint arXiv:2104.06707.

[94] Saxena, P., Reddy, N. H., & Pradhan, S. P. (2019). Magnetoelastic deformation of a circular membrane: wrinkling and limit point instabilities. International Journal of Non-Linear Mechanics, 116, 250-261.

[95] Shan, S., Kang, S. H., Raney, J. R., Wang, P., Fang, L., Candido, F., ... & Bertoldi, K. (2015). Multistable architected materials for trapping elastic strain energy. Advanced Materials, 27(29), 4296-4301.

[96] Shan, S., Kang, S. H., Wang, P., Qu, C., Shian, S., Chen, E. R., & Bertoldi, K. (2014). Harnessing Multiple Folding Mechanisms in Soft Periodic Structures for Tunable Control of

Elastic Waves. Advanced Functional Materials, 24(31), 4935–4942.

[97] Shull, K. R., Flanigan, C. M., & Crosby, A. J. (2000). Fingering instabilities of confined elastic layers in tension. Physical review letters, 84(14), 3057.

[98] Slesarenko, V., & Rudykh, S. (2016). Harnessing viscoelasticity and instabilities for tuning wavy patterns in soft layered composites. Soft Matter, 12(16), 3677–3682.

[99] Slesarenko, V., & Rudykh, S. (2017). Microscopic and macroscopic instabilities in hyperelastic fiber composites. Journal of the Mechanics and Physics of Solids, 99, 471-482.

[100] Slesarenko, V., Galich, P. I., Li, J., Fang, N. X., & Rudykh, S. (2018). Foreshadowing elastic instabilities by negative group velocity in soft composites. Applied Physics Letters, 113(3).

[101] Song, J., Jiang, H., Liu, Z. J., Khang, D. Y., Huang, Y., Rogers, J. A., ... & Koh, C. (2008). Buckling of a stiff thin film on a compliant substrate in large deformation. International Journal of Solids and Structures, 45(10), 3107-3121.

[102] Su, Y., Wu, B., Chen, W., & Destrade, M. (2020). Pattern evolution in bending dielectric-elastomeric bilayers. Journal of the Mechanics and Physics of Solids, 136, 103670.

[103] Sun, J. Y., Xia, S., Moon, M. W., Oh, K. H., & Kim, K. S. (2012). Folding wrinkles of a thin stiff layer on a soft substrate. Proceedings of the Royal Society A: Mathematical, Physical and Engineering Sciences, 468(2140), 932-953.

[104] Tang, Y., Lin, G., Han, L., Qiu, S., Yang, S., & Yin, J. (2015). Design of hierarchically cut hinges for highly stretchable and reconfigurable metamaterials with enhanced strength. Advanced materials, 27(44), 7181-7190.

[105] Tipton, C. R., Han, E., & Mullin, T. (2012). Magneto-elastic buckling of a soft cellular solid. Soft Matter, 8(26), 6880-6883.

[106] Triantafyllidis, N., & Schraad, M. W. (1998). Onset of failure in aluminum honeycombs under general in-plane loading. Journal of the Mechanics and Physics of Solids, 46(6), 1089-1124.

[107] Triantafyllidis, N., Nestorović, M. D., & Schraad, M. W. (2006). Failure Surfaces for Finitely Strained Two-Phase Periodic Solids Under General In-Plane Loading. Journal of Applied Mechanics, 73(3), 505–515.

[108] Vella, D., Bico, J., Boudaoud, A., Roman, B., & Reis, P. M. (2009). The macroscopic delamination of thin films from elastic substrates. Proceedings of the National Academy of Sciences, 106(27), 10901-10906.

[109] Volokh, K. Y. (2017). Loss of ellipticity in elasticity with energy limiters. European Journal of Mechanics-A/Solids, 63, 36-42.

[110] Wang, P., Casadei, F., Shan, S., Weaver, J. C., & Bertoldi, K. (2014). Harnessing Buckling to Design Tunable Locally Resonant Acoustic Metamaterials. Physical Review Letters, 113(1), 014301.

[111] Wu, J., Zhao, Z., Hamel, C. M., Mu, X., Kuang, X., Guo, Z., & Qi, H. J. (2018). Evolution of material properties during free radical photopolymerization. Journal of the Mechanics and Physics of Solids, 112, 25-49.

[112] Xiang, Y., Chen, D., Arora, N., Yao, Q., & Rudykh, S. (2023). Towards understanding the role of viscoelasticity in microstructural buckling in soft particulate composites. Composites Part B: Engineering, 110850.

[113] Xiang, Y., Schilling, C., Arora, N., Boydston, A. J., & Rudykh, S. (2020a). Mechanical characterization and constitutive modeling of visco-hyperelasticity of photocured polymers. Additive Manufacturing, 36, 101511.

[114] Xiang, Y., Zhong, D., Rudykh, S., Zhou, H., Qu, S., & Yang, W. (2020b). A Review of Physically Based and Thermodynamically Based Constitutive Models for Soft Materials. Journal of Applied Mechanics, Transactions ASME, 87(11), 110801.

[115] Yin, J., & Boyce, M. C. (2015). Unique wrinkles as identity tags. Nature, 520(7546), 164-165.

[116] Yin, J., Yagüe, J. L., Eggenspieler, D., Gleason, K. K., & Boyce, M. C. (2012). Deterministic order in surface micro-topologies through sequential wrinkling. Advanced materials, 24(40), 5441-5446.

[117] Yin, S. F., Li, B., Cao, Y. P., & Feng, X. Q. (2018). Surface wrinkling of anisotropic films bonded on a compliant substrate. International Journal of Solids and Structures, 141, 219-231.

[118] Yu, K., Fang, N. X., Huang, G., & Wang, Q. (2018). Magnetoactive acoustic metamaterials. Advanced Materials, 30(21), 1706348.

[119] Yu, P., Bordas, S. P. A., & Kerfriden, P. (2022). Adaptive Isogeometric analysis for transient dynamics: Space–time refinement based on hierarchical a-posteriori error estimations. Computer Methods in Applied Mechanics and Engineering, 394, 114774.